UNIVERSITY OF CALGARY

Near-surface characterization and Vp/Vs analysis of a shale gas basin

by

Liliana M. Zuleta Tobon

A THESIS

SUBMITTED TO THE FACULTY OF GRADUATE STUDIES

IN PARTIAL FULFILMENT OF THE REQUIREMENTS FOR THE

DEGREE OF MASTER OF SCIENCE

DEPARTMENT OF GEOSCIENCE

CALGARY, ALBERTA

APRIL, 2012

UNIVERSITY OF CALGARY

FACULTY OF GRADUATE STUDIES

The undersigned certify that they have read, and recommend to the Faculty of Graduate Studies for acceptance, a thesis entitled “Near-surface characterization and Vp/Vs analysis of a shale gas basin" submitted by Liliana M. Zuleta Tobon in partial fulfilment of the requirements of the degree of Master of science.

Supervisor, Dr. Donald C. Lawton, Department of Geoscience

Dr. Kristopher Innanen, Department of Geoscience

Dr. Michael Wieser, Department of Physics and Astronomy

Date

Abstract

The data from a multicomponent refraction survey acquired in Northeast British Columbia was used in this thesis to carry out P-wave and S-wave near-surface description and to undertake Vp/Vs analysis of shallow and deep formations. The datasets had good quality for picking first break arrivals and to process the reflection data successfully.

Three lines from the refraction survey were used for this study. An important feature was the confirmation of a channel that was detected through a previously acquired electromagnetic survey. The near-surface model obtained from P-wave data showed two layers with P-wave velocities of ~ 1950 m/s for the first layer and ~ 2800 m/s for the second layer. The SH-wave data from one of the lines showed three layers in the west end of the line and two layers to the east end of the line. The other line showed three layers along the entire profile. The S-wave velocity of the first layer was found to be around 375 m/s, that for the second layer was ~ 727 m/s and the S-wave velocity for the third layer was ~ 1400 m/s.

The velocity-depth structure obtained for the near-surface was used for the calculation of static corrections. As expected, S-wave static corrections gave higher values that the P-wave static corrections. The datum static corrections vary from -150 ms to -250 ms for SH-wave data and about -15 ms to 15 ms for P-wave data.

Vp/Vs analysis was performed for the near-surface structure with the values of velocities obtained from the refraction analysis and also through PP-PS registration for deeper structures. Measured values of Vp/Vs showed differences of around 0.1 when compared to those from well log. Values of Vp/Vs ranged from 5 in the near-surface to 2.2 in deeper formations.

Acknowledgements

I would like to thank my supervisor, Dr Donald C. Lawton for his guidance, wise counsels and patience during the time I was working on my research. I would also like to express my gratefulness to the committee members, Dr Kris Inannen and Dr. Michael Wieser for their advices.

Thanks to Nexen for allowing me to show the results of this project, especially to Eric Von Lunen and Jennifer Leslie-Panek who made possible the use of the data and gave me their support to do this project.

My recognition goes to the directors and staffs of the CREWES project, especially Helen Isaac, Kevin Hall and Rolf Maier. My sincere gratitude to Penny Colton from Sensor Geophysical and to Saul Guevara from Crewes. Gedco and Hampson-Russell Software are also acknowledged for providing software used in this work.

Last but not least, I would like to thank my husband, Fernando, for his support and encouragement all the time.

Dedication

To God.

To my family in Colombia that do not know what I am doing.

To my husband, who is the energy to do what I am doing.

Table of Contents

List of Tables

List of Figures and Illustrations

List of Symbols, Abbreviations and Nomenclature

Symbol	Definition
θc	Critical angle
θ_i	Incident angle
k	Bulk modulus
μ	Shear modulus
ρ	Density
σ	Poisson’s ratio
γ	Ratio of incident to reflected wave velocity
3C	Three components
Δx, Δy	Bin size
Δr	Receiver interval
3D	Three dimensional
AVO	Amplitude Versus offset
AVOA	Amplitude versus azimuth
CCP	Common conversion point
CDP	Common depth point
CMP	Common mid point
DMO	Dip move out
EM	Electromagnetism
E_d	Datum elevation
E_g	Geophone elevation
FT	Fold taper
FZ	Fresnel zone
f_{max}	Maximum frequency
FD	Finite difference
h, H	Refractor thickness
k_{max}	Maximum wave number
LVL	Low velocity layer
NEBC	Northeast British Colombia
NMO	Normal move out
P	Compressional wave
PP	Compressional reflected to compressional
PS	Compressional reflected to Shear
SS	Shear to shear reflection
RI, RLI	Receiver interval and receiver line interval
SI, SLI	Source interval and source line interval
S/N	Source to noise ratio
S	Shear wave
SV, SH	Shear-vertical and shear horizontal wave
t	time
T and R	Transversal and Radial geophone components
TWT	Two way time

T^+	Plus-times in the plus-minus time analysis
T^-	Minus-times in the plus-minus time analysis
T_d	Datum correction time
T_w	Weathering correction time
T_e	Elevation correction time
Vp	Compressional wave Velocity
TV	Time variant
V_{rms}	Root-mean-square velocity
Vs	Shear wave Velocity
Vw	Velocity of the weathered layer
V_i	Velocity of i layer (i= 1, 2 or 3)
Vα	Velocity of the incident wave
X_c	Crossover distance
X_{cr}	Critical distance
X_{max}	Maximum offset
X_{min}	Minimum offset

Chapter One: **INTRODUCTION AND THEORY OF METHODS**

1.1 Background

The project area studied in this thesis is located in northeast British Columbia (NEBC). A large 3D/3C seismic survey will be acquired in this area, and therefore to ensure optimum quality of the information to be collected, a refraction survey was acquired to give information about the near-surface, with an emphasis to the shear wave properties. Knowledge about the velocity-depth structure of the near-surface and feasibility of acquiring multicomponent data were the main drivers for this acquisition. Also, it is important to know the structure of the near-surface for the investigation and integration with deeper data. As a result, analysis of Vp/Vs was carried out for both the shallow and deep formations. The refraction analysis targeted the near-surface study and horizon registration on PP and PS reflection sections was used for the deeper structure.

Ensuring the collection of useful data, in terms of quality and viability of imaging from the shear and the converted waves is an important issue for the design of the 3D/3C seismic survey. As a result, analysis of the acquisition footprint was carried out during the design stage in order to anticipate this kind of problem. Different geometries were tried and the results were chosen to optimize acquisition, and minimize the effect of the layout in the data.

For this study, the first issue to consider was the irregularities in the terrain and near-surface in the project area, particularly the influence of glacial till for the large scale multicomponent survey. Understanding these irregularities and possible techniques to treat them is very important. This chapter provides a short description of different scenarios to consider for near-surface studies, including the key method used in this thesis, namely the refraction seismology. The knowledge about the depth-velocity structure allows the calculation of statics corrections needed for reflection surveys; these are described briefly. Following this, there are some considerations about shear and compressional waves and their corresponding velocities and velocity ratio. Finally, some issues about multicomponent survey design are explained.

The structure of this thesis is the following: Chapter 1 is a general theory background related to static corrections, Vp/Vs relationship with the different parameters that affect it and survey design. It also reviews the objectives of this thesis. Chapter 2 is a description of the geology in northeast British Columbia, the location area for this study; the surficial and bedrock geology description is included as it is a fundamental part of this thesis. Chapter 3 shows the near-surface velocity-depth results from the plus-minus time analysis and the static correction times. Chapter 4 covers the compressional to shear velocity analysis for shallow and deep structure and comparison with well log data. This process involved PP to PS registration of the seismic data. Chapter 5 is the description of the footprint analysis from the survey design to be used for the 3D/3C seismic survey. Finally chapter 6 presents the conclusions from this thesis and recommendation of future work.

1.1.1 Near-surface characterization

Lateral changes in the elevation of the ground surface require elevation corrections to be made to reflection seismic data. However, even if the terrain is flat, these corrections are needed due to lateral changes in the near-surface (Cox, 1999) or seismic wave propagation in the weathered layer (Figure 1-1). These corrections are referred to as static corrections (section 1.3) and means that a reference datum is chosen to calculate the corrections (time shifts) so that shotpoints and geophones are located on that datum assuming uniform conditions and no low velocity layer (LVL) material below that datum (Telford et al., 1990).

The weathered layer is the shallow unconsolidated portion on the sub-surface in which low velocity is characteristic and air rather than water fills the pores (Sheriff, 1991). The base of this layer occurs where there is a change to a layer of higher velocity or where the velocity no longer changes rapidly with depth. It is also known as the low velocity layer (LVL) and it can be very irregular, in both lateral and vertical directions, with varying lithology, density and velocity. The depth to the base of this weathered layer is one of the objectives for refraction surveys and one objective of this thesis.

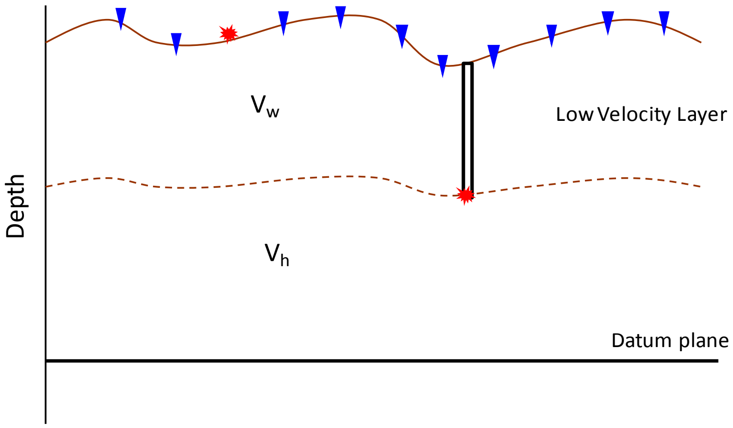

Figure 1-1. Near-surface profile needed for static corrections.

Different surface and near-surface conditions involve specific problems and subsequent requirements for datum static corrections. Examples include sand dune topography, areas where the weathered layer is highly irregular (swamps, larger river deltas), permafrost topography, and mountain topography.

Complications related to sand dunes include: compaction with height producing higher velocity at the base of the dune and away from the edges than close to the surface; the position of the dune changes with time as they are formed by wind-blown sand, which means that the elevation profile also changes with time; sometimes there are gravel plains at the base of the dunes so a refractor is detected with a smoother profile than the surface topography and can be used to estimate traveltimes in the near-surface. The challenge is to find an appropriate velocity function that represents the increasing velocity with depth in order to calculate the datum static corrections (Cox, 1999). Al-Shuhail (2004) compared values of thickness calculated assuming constant velocity and also derived a vertical velocity function. The result showed an error of less than 15% for a 200 m thick dune. In this specific case there was no significant error in applying constant velocity. He found that the error increases with increasing sand thickness and decreasing porosity of the dune sands.

Highly irregular weathered layers are reflected by rapid changes in velocity and/or thickness in the near-surface, producing large variations in datum static corrections between adjacent source (and receiver) locations for group intervals as small as 20 m, even if the elevation changes are small. Hard rock terrain implies large and rapid variations in the depth of the weathering. Refraction surveys are useful to generate a shallow model to correct the reflection times as rocky terrain does not always produce good lateral continuity required to make appropriate residual corrections (Palmer, 2005). Discrete information is required at each source and receiver location for the calculation of static corrections when dealing with this kind of topography. Refraction based methods and high resolution reflection methods are appropriate in this situation. Interpolation between uphole surveys will not give accurate results (Cox, 1999). Another example of refraction applied to irregular bedrock, with dips of up to 30 degrees, is presented by Kilty et al. (1986). They used two refraction lines along the geological strike with high source strength and found, in addition to the expected bedrock irregularities, high variation of velocity in the overburden as well as in the bedrock. Comparing the refraction results with information from borehole, they were accurate to within 10 %.

Permafrost is defined as permanently frozen soil or rock. This frozen state results in increased velocity and can produce false time structure of deeper events in seismic data of up to hundreds of milliseconds. To compute the static corrections, refraction methods can be used but the high velocity of the permafrost normally precludes their use in mapping its base. Other methods that can be used are the ones associated with the dispersion properties of a thick near-surface layer and other geophysical (non-seismic) techniques. MacAulay and Hunter (1982), showed an example of applying refraction methods from high-resolution arrays which are better suited for the refraction interpretation. They detected thick, continuous permafrost at depth but also thin (> 15m), shallow lenses.

Sometimes mountain topography yields complex seismic-geologic near-surface conditions that limit structural imaging and interpretation (Shi, 2005). The presence of large variations of near-surface structures complicates the generation of the near-surface model and the choice of the appropriate method for static corrections. The solution in this case is to make integration of all available data in order to build the model, e.g. use geological outcrops, refraction methods, uphole survey, etc.

1.2 Refraction theory

A wave travelling from a seismic source to a receiver has many different possible paths (Figure 1-2). It can go directly (direct waves) or it can change path when it reaches an interface due to an abrupt change in elastic properties (Telford et al., 1990; Palmer, 1986). In this case, part of the energy is reflected, remaining in the first medium, and the rest is refracted into the second medium. The raypath of that wave arrives at a certain angle to the interface (with respect to the normal of the interface), the incident angle, and refracts with a different angle. When the refracted angle is 90 degrees, the incident angle is called the critical angle and the ray continues traveling along the interface with the velocity of the second medium. The ray and its associated wave fronts also act as secondary sources. The emergent ray at these new sources leaves the interface at the same critical angle. The waves (and raypaths) that travel to and along the interface and return to the original medium are referred to as refraction waves or head waves. Seismic refraction makes use of these head waves when they are received at the geophones before the direct waves (waves traveling directly by the shortest path) to find depth to the refractor and velocities of the medium (as discussed later in this thesis).

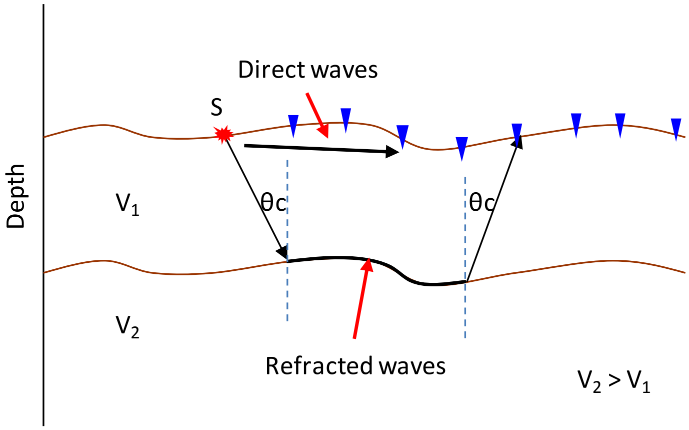

Figure 1-2. Schematic raypath for direct and refracted waves.

Most techniques for the analysis of seismic refraction data are based on Huygens' Principle, Snell's Law and critical refraction. Refraction is defined by the change in direction of a ray or a wavefront when crossing an interface between layers with different velocities. Huygens’ Principle states that every point of a wavefront can be viewed as the source of a new wavelet and that a later wavefront is the tangent envelope to all these new wavelets. When an incident wave hits an interface, this becomes the source of a reflected wave in the same medium and a refracted wave into the second medium. The velocity of the medium determines the velocity of the waves and therefore the distance between wavefronts (Sjogren, 1984). At that interface, the wavefronts follow Snell’s Law

$$\frac{\sin \theta_1}{\sin \theta_2} = \frac{V_1}{V_2} \tag{1.1}$$

Where, V_1 is the velocity of the first medium, V_2 is the velocity of the second medium, θ_1 is the angle between the incident raypath and the normal to the interface, and θ_2 is the angle between the refracted raypath and the normal to the interface. The refracted ray travels along the interface when the refracted wavefront is perpendicular to the interface, in other words $\theta_2 = 90°$. In this case, the corresponding θ_1 is called the critical angle (θ_c) and is defined as

$$\sin \theta_c = \frac{V_1}{V_2} \tag{1.2}$$

This equation is valid when the velocity of the second layer is greater than the velocity of the first layer. The emergent angle from the interface for the wavefront (or ray) in the upper medium is also the critical angle. The waves that travel along the interface and return to the surface are called refracted waves or head waves. Direct waves, which travel directly by the shortest path, arrive first to receivers close to the source, but there is a point beyond which the refracted waves arrive at the receivers before the direct waves (Figure 1-3). This is the *crossover point* and the distance from the source to this point is the crossover distance. The head waves arrive first because the longer distance they have to cover is compensated by the faster velocity of the second medium through which they are passing.

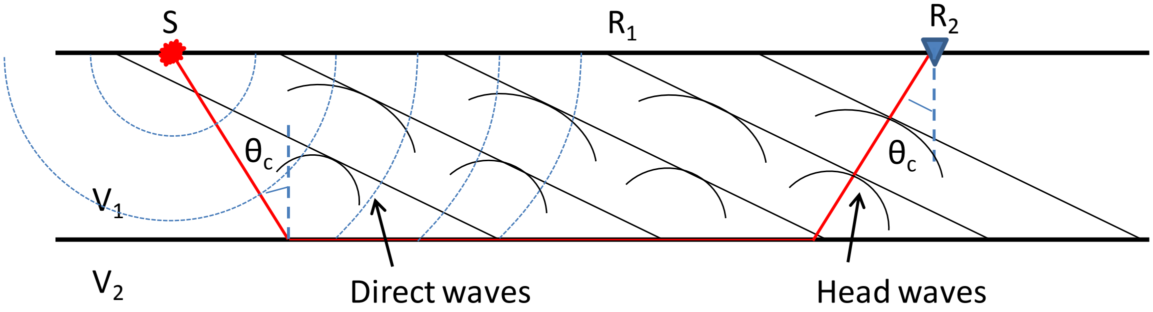

Figure 1-3. Two layers separated by a horizontal interface. Wavefronts and raypaths are depicted (S represents the source; R_1, R_2 represents the receivers).

There are different refraction interpretation techniques suitable for different types of geology. These refraction interpretation methods can be divided in two basic approaches: those in which the data is analyzed at a common surface location and those analyzed at a common sub-surface location (emergent point).

The techniques normally used for near-surface investigation include the intercept-time method, the ABC method (Sjogren, 1984), Hagedoorn or plus-minus method (Hagedoorn, 1959), generalized reciprocal method or GRM (Palmer, 1980, 1986), Gardner method (Gardner, 1939), Blondeau method and the inversion, time-term (or decomposition), general wavefront technique (graphical) and tomographic approaches (Sjogren, 1984, Cox, 1999; Telford, 1990). Almost all the refraction techniques assume that the refracted ray travels in a vertical plane, defined at the surface by the source and receiver locations. This would not be the case for cross dipping refractors.

The interpretation technique used for this thesis was the plus-minus time analysis method, which is explained in section 1.2.1. The concept of *delay time* has first to be explained which is linked to the concept of intercept time, t_i. The latter is the extrapolation of the time-distance curve to zero offset with the apparent velocity of the refractor and it is denoted by the expression

$$t_i = t - \frac{X_i}{V_a} \tag{1.3}$$

Where t is the arrival time, X_i is the source-receiver offset and V_a is the apparent velocity of the refractor estimated from a time-distance graph of the refraction data (Figure 1-4). This velocity depends on the true refractor velocity and the dip of the refractor. If the true velocity is used in expression 1.3, the result is the difference between the actual travel time and the time to travel the horizontal distance from the source to the receiver at the refractor velocity. The *delay time* was defined by Gardner (1939) as the portion of the intercept time associated with one end of the raypath (source or receiver). As a result the intercept time is the sum of the delay time at the source and the delay time at the receiver. This definition assumes that the refractor is flat where the refracted wave enters and leaves the refractor. This assumption holds for dips less than 10 degrees.

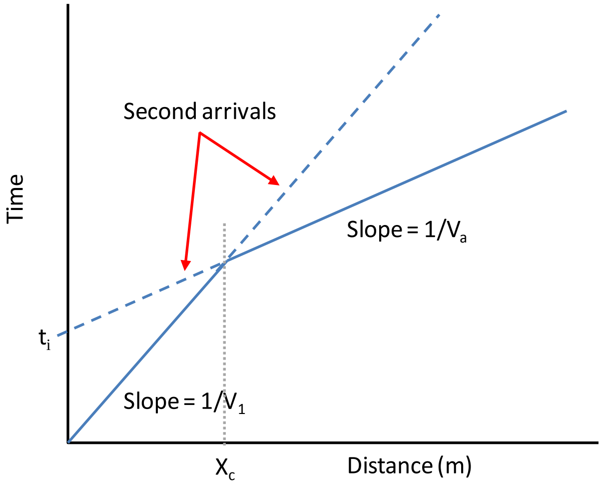

Figure 1-4. Time-distance curve for two layers. t_i is the intercept time, X_c is the crossover distance, V_1 is the velocity of layer 1 and V_a is the velocity of layer 2.

The total travel time, t_x, from source S to receiver R in Figure 1-5 is given by

$$t_x = \frac{SB}{V_1} + \frac{BC}{V_2} + \frac{CR}{V_1} \tag{1.4}$$

Where V_1 and V_2 are the velocities of the near-surface (first layer) and the refractor, respectively. Rearranging equation 1.4 and taking in to account the delay time definition, it can be expressed as:

$$t_x = \left(\frac{SB}{V_1} - \frac{AB}{V_2} + \frac{AB}{V_2}\right) + \frac{BC}{V_2} + \left(\frac{CR}{V_1} - \frac{CD}{V_2} + \frac{CD}{V_2}\right) \tag{1.5}$$

$$t_x = \left(\frac{SB}{V_1} - \frac{AB}{V_2}\right) + \left(\frac{CR}{V_1} - \frac{CD}{V_2}\right) + \frac{SR}{V_2}$$

$$t_x = t_{ds} + t_{dr} + \frac{X}{V_2}$$

t_{ds} and t_{dr} are the delay times at source and receiver locations, respectively. X is the distance from source to receiver (SR ≈ AB + BC + CD), assuming that h_s and h_r are not greatly different.

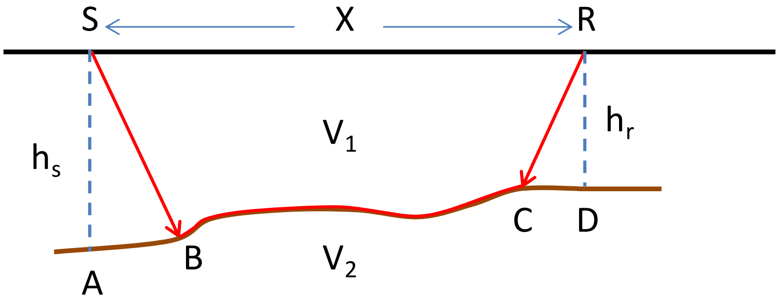

Figure 1-5. Source to receiver path for a two layer model to illustrate the delay time concept.

The delay times can be expressed as

$$t_{ds} = \frac{SB}{V_1} - \frac{AB}{V_2} \quad \text{and} \quad t_{dr} = \frac{CR}{V_1} - \frac{CD}{V_2}$$

Using simple geometry, the delay time at the source can be rearranged as

$$t_{ds} = \frac{h_s}{V_1 \cos\theta_c} - \frac{h_s \tan\theta_c}{V_2}$$

h_s is the depth to the refractor at the source location and θ_c is the critical angle defined by Snell's Law for critical refraction (equation 1.2). This can be used to simplify the delay time expression and solve for h_s:

$$h_s = \frac{V_1 t_{ds}}{\cos\theta_c} \tag{1.6}$$

Similarly for the delay time at the receiver:

$$h_r = \frac{V_1 t_{dr}}{\cos \theta_c} \quad \textbf{(1.7)}$$

1.2.1 Plus-Minus time analysis method

The plus-minus time analysis method (Hagedoorn, 1959; Dufour, 1996) is useful for both depth and velocity determination. The basis of the plus-minus time analysis method lies in the traveltime reciprocity: The traveltime from source to receiver is the same as from receiver to source if they are interchanged. The basic geometry for this method is presented in Figure 1-6.

The plus-times are used to give the traveltime from the surface to the refractor while the refractor velocity is estimated from the minus times; data are analyzed at a common surface location where the rays from two sources are recorded. The plus-time (T^+_D) is defined as the sum of the traveltimes from two sources located on either side of a receiver (T_{AD}, T_{HD}) minus the reciprocal time from shot to shot (T_{AH}, T_{HA}). The minus-time (T^-_D) is calculated by subtracting the times from the two sources located on either side of a receiver, and then subtracting the reciprocal time.

In this method it is assumed homogeneity in the layers, large velocity contrast between the layers and dip of the refractor smaller than 10 degrees. To use this method, enough receiver spread should be recorded in both directions, at least covering the whole distance between the sources. A window of analysis is defined between the two crossover points (from the forward and reverse curves, X_f and X_r, respectively). Inside this window, the plus-time value at each receiver is defined by the following expression (Figure 1-6):

$$T^+_D = T_{AD} + T_{HD} - T_{AH} \quad \textbf{(1.8)}$$

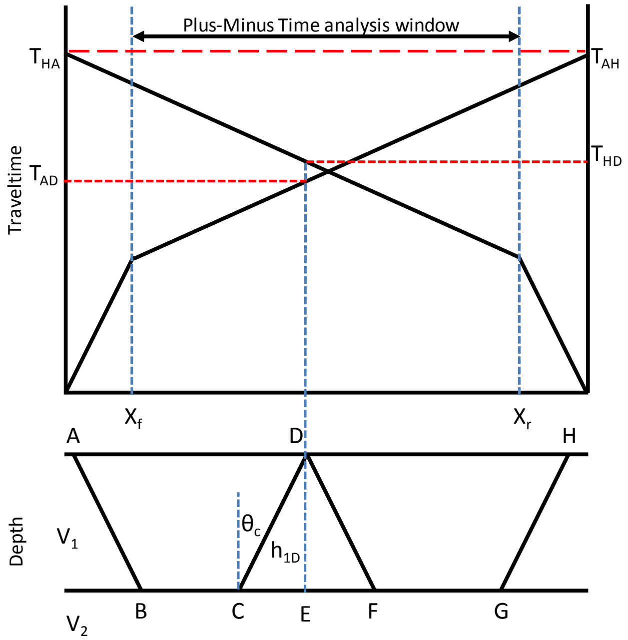

Figure 1-6. Plus time analysis according to the plus-minus method of Hagedoorn (1959).

Using the delay time definition, the refraction arrival times from source (A, H) to receiver (D) can be express as

$$T_{AD} = t_{dA} + t_{dD} + \frac{AD}{V_2}$$

$$T_{AH} = t_{dA} + t_{dH} + \frac{AH}{V_2}$$

and

$$T_{HD} = t_{dH} + t_{dD} + \frac{HD}{V_2}$$

t_{dA}, t_{dH} and t_{dD} are the delay times at locations A, H and D. By replacing these expressions in equation 1.8 the T^+ can be defined as:

$$T_D{}^+ = 2t_{dD} + \frac{AD}{V_2} + \frac{HD}{V_2} - \frac{AH}{V_2}$$

Since $AD + HD = AH$ then

Then $T_D{}^+ = 2t_{dD}$

Thus $$T_D^{+} = 2h_{1D}\frac{\cos\theta_c}{V_1} \qquad \textbf{(1.9)}$$

From equation 1.9, the expression for depth (at a specific receiver) for a two-layer case can be defined as:

$$h_{1D} = \frac{T_D^{+}V_1}{2\cos\theta_c} \qquad \textbf{(1.10)}$$

The velocity of the first layer (V_1) can be found using the inverse slope for the best-fit line of the first layer first break arrivals (source to crossover point). The second layer velocity (V_2) can be derived using the minus-time analysis over a window that includes only the second layer first break arrivals. θc is the critical angle, $\theta c = \sin^{-1}(V_1/V_2)$.

To find the velocity for the refractor, the minus-time definition is used. The minus-time at a receiver D (Figure 1-7) is defined as (Hagedoorn, 1959)

$$T^{-}_{D} = T_{AD} - T_{HD} - T_{AH} \qquad \textbf{(1.11a)}$$

The minus-time at a receiver D' is

$$T^{-}_{D'} = T_{AD'} - T_{HD'} - T_{AH} \qquad \textbf{(1.11b)}$$

Subtracting equation 1.11a from equation 1.11b yields:

$$T^{-}_{D'} - T^{-}_{D} = T_{AD'} - T_{HD'} - T_{AH} - T_{AD} + T_{HD} + T_{AH}$$

$$T^{-}_{D'} - T^{-}_{D} = T_{AD'} - T_{AD} + T_{HD} - T_{HD'}$$

$$T^{-}_{D'} - T^{-}_{D} = \Delta X/ V_2 + \Delta X/ V_2$$

$$T^{-}_{D'} - T^{-}_{D} = 2\Delta X/V_2 \qquad \textbf{(1.12)}$$

Where, $T_{AD'}$ is the time from shot A to receiver D'; T_{AD} is the time from shot A to receiver D; $T_{HD'}$ is the time from shot H to receiver D'; T_{HD} is the time from shot H to receiver D; ΔX is distance between consecutive receivers. The velocity of the second layer (V_2) is equal to twice the inverse slope of a best-fit line through a plot of minus-time vs. distance inside the plus-minus time analysis window.

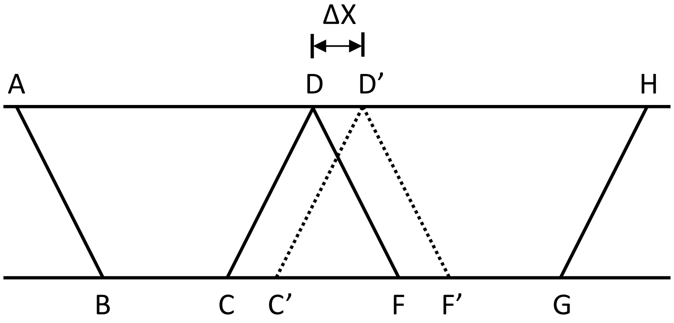

Figure 1-7. Raypaths for a reversed refraction profile to illustrate the Hagedoorn or plus-minus method.

For 3-layer case (Figure 1-8):

$$\begin{aligned} T_{AB'EFC'D} &= 2T_{AB'} + T_{EF} + 2T_{B'E} \\ T_{AB'EFC'D} &= \frac{2h_1}{V_1 * \cos\theta_{13}} + \frac{X_r - 2h_1\tan\theta_{13} - 2h_2\tan\theta_{23}}{V_3} + \frac{2h_2}{V_2\cos\theta_{23}} \\ T_{AB'EFC'D} &= \frac{X_r}{V_3} + 2h_1\left(\frac{1}{V_1\cos\theta_{13}} - \frac{\tan\theta_{13}}{V_3}\right) + 2h_2\left(\frac{1}{V_2\cos\theta_{23}} - \frac{\tan\theta_{23}}{V_3}\right) \end{aligned} \tag{1.13}$$

By Snell's Law: $\sin\theta_{13} = V_1/V_3$ and $\sin\theta_{23} = V_2/V_3$

$$\begin{aligned} T_{AB'EFC'D} &= \frac{X_r}{V_3} + 2h_1\left(\frac{1}{V_1\cos\theta_{13}} - \frac{\sin\theta_{13}\sin\theta_{13}}{\cos\theta_{13}V_1}\right) + 2h_2\left(\frac{1}{V_2\cos\theta_{23}} - \frac{\sin\theta_{23}\sin\theta_{23}}{\cos\theta_{23}V_2}\right) \\ T_{AB'EFC'D} &= \frac{X_r}{V_3} + \frac{2h_1\cos\theta_{13}}{V_1} + \frac{2h_2\cos\theta_{23}}{V_2} \end{aligned} \tag{1.14}$$

From equation 1.14 the plus times can be defined as:

$$T^+ = \frac{2h_1\cos\theta_{13}}{V_1} + \frac{2h_2\cos\theta_{23}}{V_2}$$

After some manipulation, the thickness of the second layer can be obtained.

$$h_2 = \left[T^+ - \frac{2h_1\cos\theta_{13}}{V_1}\right]\frac{V_2}{2\cos\theta_{23}} \tag{1.15}$$

V_3 can be obtained from the ΔT^{-}_{D} vs. ΔX curve for the appropriate window. θ_{23} is the critical angle, calculated following Snell's law as $\theta_{23} = \sin^{-1}(V_2/V_3)$

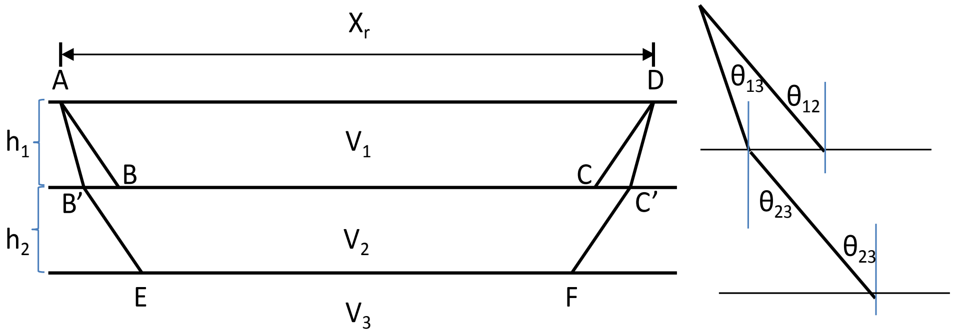

Figure 1-8. Source (A) to receiver (D) path for three layers separated by horizontal interfaces.

Summary of the method

Knowing the first and second layer velocities and the plus-time values at each receiver, the thickness of the first layer below each receiver can be obtained according to the delay time analysis. The delay-time represents the time to travel from the receiver to the refractor minus the time necessary to travel the normal projection of the raypath on the refractor (Figure 1-5). From Snell's law, a relation between the delay times (left and right) and the thickness of the first layer at the receiver can be established. Finally, the link between the delay times and the plus-times allows us to determine the thickness of the first layer below each receiver inside the plus-minus time analysis window (equation (1.10). This will allow the determination of the first layer thickness and velocity all along a seismic survey line, from which surface-consistent static corrections can be extracted (section 1.3). This analysis is for a two layer case in two dimensions.

1.3 Datum Static Corrections

Static corrections are time shifts applied to the seismic data to correct for irregularities in the near-surface, low velocity material, different elevation of the stations, etc. The goal is to correct the reflection times to what would be recorded on a flat surface without the influence of the near-surface velocity structure (Cox, 1999). This last statement implies the assumption of vertical traveltime as the reflection times are adjusted to simulate data registered vertically up or down to the specified datum. The datum static corrections are simple to compute from near-surface parameters: elevation, thickness and velocity. One method to obtain this information is from refraction surveys.

The first step is to remove the weathering layer (or low-velocity layer, LVL) so that the base of this layer becomes the new reference surface. The times are corrected as if they have been observed on this new surface. This correction is often called the weathering correction, T_w. The second step is to adjust the data to simulate it as being recorded at another reference surface called the datum. This correction is often called the elevation correction, T_e (Cox, 1999). The datum correction (T_d) must include both the weathering correction and the elevation correction to remove the time effect of the weathered layer and to adjust the times to a datum elevation using a replacement velocity (Figure 1-9). Usually, the replacement velocity is the refractor velocity and it is used to compensate for low-velocity near-surface materials (Sheriff, 1991).

$$\mathrm{T_d} = -\mathrm{T_w} + \mathrm{T_e} \qquad \textbf{(1.16)}$$

The datum correction (T_d) for the two layer case is defined as

$$T_d = -\frac{H_1}{V_1} + \left(\frac{\left(E_d - E_g\right) + H_1}{V_3} \right) \qquad \textbf{(1.17)}$$

And for the three layer case:

$$T_d = -\frac{H_1}{V_1} - \frac{H_2}{V_2} + \left(\frac{\left(E_d - E_g\right) + H_1 + H_2}{V_3} \right) \qquad \textbf{(1.18)}$$

H_1 and H_2 are the thickness of layers 1 and 2, respectively. V_1, V_2 and V_3 are the velocities of layer 1, 2 and 3, respectively. E_d is the datum elevation and E_g is the surface elevation where the geophones are located (Figure 1-9). In general, a negative static correction reduces the reflection time.

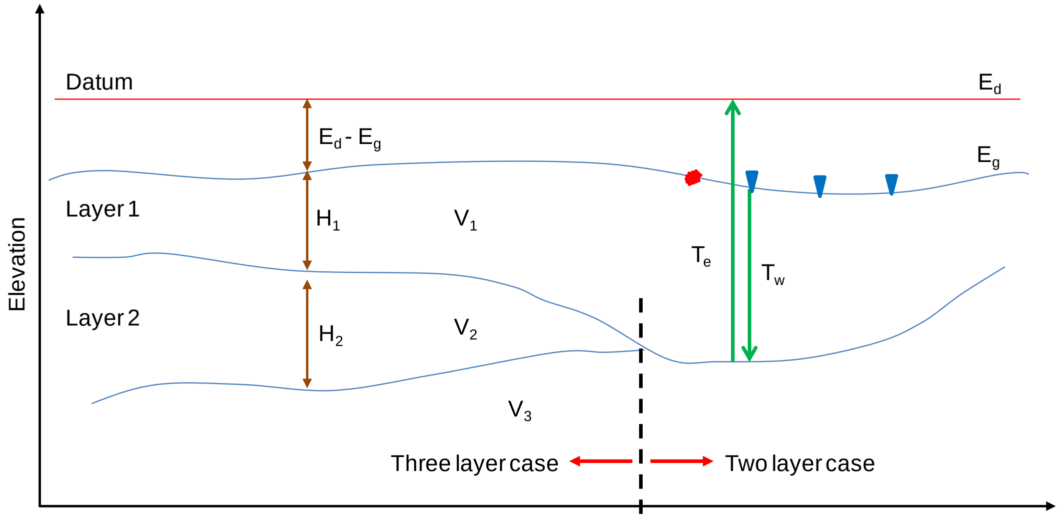

Figure 1-9. Schematic diagram illustrating components of datum static corrections.

The computation of datum static corrections requires the following parameters: Source and receiver elevations and the thicknesses and velocities of the weathered layer or layers are needed for the weathering correction; the elevation of the reference datum and the replacement velocity (usually the velocity of the deeper refractor) from the base of the weathered layer to the reference datum are needed for the elevation correction. The surface elevation is routinely obtained from survey measurements. For deep-hole dynamite surveys, the source elevation is computed from the surface elevation minus the borehole depth which is measured by the driller.

Direct measurements of the thicknesses and velocities of the weathered layers can be made with uphole surveys but these parameters can change slowly or rapidly, both in the horizontal and vertical directions. Despite of this, interpolation between these locations (control points) can be used to obtain an estimate of these parameters at each source and receiver location (Cox, 1999; Guevara, 2011).

When each receiver array is tied to a specific x-y coordinate along the line, a datum static correction value must be computed at each location. The concept of a single value for a specific location is often referred to as surface consistency. Thus, datum static corrections for a line are surface consistent.

1.4 Shear (S) and compressional (P) wave (body waves) velocities

P-waves have higher velocities than S-waves and generally have higher signal to noise ratio, which make them the primary seismic waves used for hydrocarbon exploration. Compressional waves arrive first and have a rectilinear particle motion, for this reason they are more easily generated for a variety of sources. The particle motion is always polarized in the direction of wave propagation (Figure 1-10a). P-wave velocity (Vp) can be derived from Newton's second law of motion and Hooke's law of elasticity (Sheriff and Geldart, 1995). P-wave velocity can be expressed as:

$$V_p = \sqrt{\frac{\kappa + {}^{4}\!/_{3}\,\mu}{\rho}} \tag{1.19}$$

Where *k* is the bulk modulus, μ is the shear modulus and ρ is the density. The bulk modulus can be considered as the incompressibility of the material and the shear modulus as the rigidity or resistance of the material to shear stresses.

S-waves propagate in elastic solid media but not in liquid media so they are not affected by the fluids in the rock. The particle motion is perpendicular to the direction of wave propagation (Dobrin and Savit, 1988). They can be classified as SH and SV depending on the polarization plane or the direction of propagation. SH waves are generated by sources acting perpendicular to the inline direction (Figure 1-10b); the particle motion purely horizontal. SV waves are generated by sources acting in the inline direction (Figure 1-10c); SV-waves propagate in a vertical plane containing the source and receiver (Tatham and McCormack,1991; Cerda, 2001). The S-wave velocity (Vs) is expressed as:

$$V_S = \sqrt{\frac{\mu}{\rho}} \tag{1.20}$$

From this equation can be seen that the greater the shear modulus, or the more resistant to shear the material is the greater will be the S-wave velocity. Fluids have no resistance to shear so S-waves do not propagate in fluids. As a result, S-waves are less affected by the water table or by fluids in the pores (Al Dulaijan, 2008) than are P-waves.

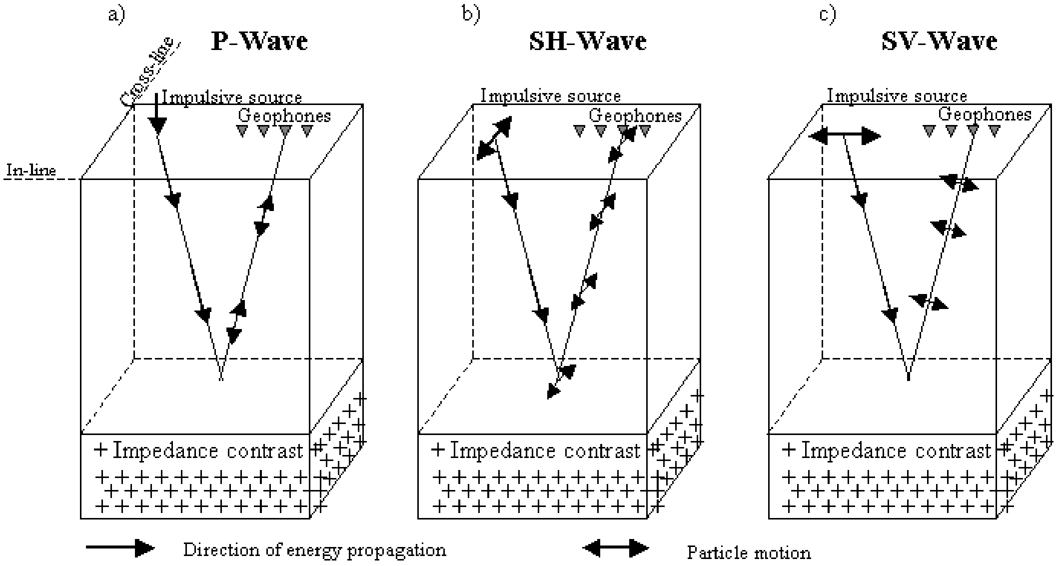

Figure 1-10. Particle motion of P-wave, SH-wave, and SV-wave in two layered media (from Cerda, 2001).

1.4.1 Vp, Vs and Vp/Vs analysis

Velocity information can be obtained from lab measurements, well logs, vertical seismic profile (VSP), and surface seismic data. Variations in rock properties produce changes in P-wave velocity, S-wave velocity and their ratio. Hence, these velocities and their ratio are used to interpret some specific properties of the rock, although this is non unique; more information is required for interpretation. Additional to velocities, prestack and poststack reflection amplitudes, attenuation, anisotropy, well log information and regional geological data are required. Seismic velocities are affected by lithology, porosity, pore fluid type, pore shape, compaction due to burial, temperature, and anisotropy (Tatham and McCormack, 1991). Some of these parameters are explained below.

Lithology: It is difficult to establish unambiguous relationships between sedimentary rock types, Vp, Vs and Vp/Vs. Clean, well-consolidated sandstones, dolomites and limestones can be distinguished for their unique Vp/Vs values; this can be seen on the “Pickett Diagram” (Figure 1-11, Pickett, 1963; Tatham and McCormack, 1991).

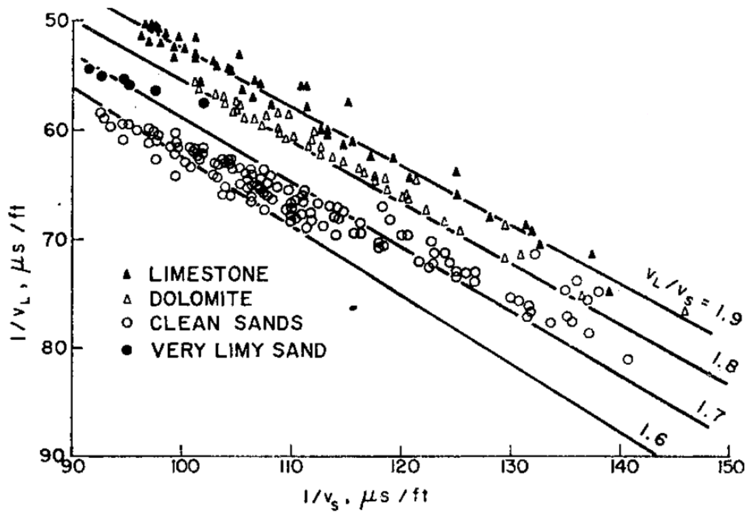

Figure 1-11. Reciprocal compressional velocity (1/V$_L$) vs Reciprocal shear velocity (1/V$_s$). Laboratory measurements on Limestones, dolomites and sands (Pickett, 1963).

From this diagram, limestone has Vp/Vs of 1.9, dolomite near 1.8 and sandstone in the range of 1.65 and 1.75. Miller (1990) found average Vp/Vs values of 1.6 for sandstones and 1.89 for limestones and shales.

Other rock properties can variously control Vp, Vs and Vp/Vs in different lithologies. Vp/Vs is a better indicator of lithology than each velocity by itself, but both parameters produce better results in determining rock types than either parameter alone. Shale is a special case with a broader range in Vp/Vs typically between 2 and 3. Jain (1987) reviewed literature available with studies in dependence of lithology on Vp/Vs, as well as work by Domenico (1974, 1976), Castagna et al. (1985) and Han et al. (1986). In summary, all these studies coincide in the range of values for the Poisson's ratio in different lithologies. They found that a large decrease in Poisson ratio in a sand environment indicates the presence of gas; a small decrease in Poisson's ratio could indicate increase in porosity or increase of shale; in carbonates, a small decrease could indicate dolomitization or an increase in porosity. Vp/Vs is related to Poisson's ratio,σ, by the following expression:

$$\frac{V_p}{V_s} = \sqrt{\frac{1-\sigma}{0.5-\sigma}} \tag{1.21}$$

Many authors have demonstrated the relationship between lithology and Vp/Vs. Castagna (1985) found different relationships between compressional velocity and shear velocity for different lithologies (dry and wet sandstones, water saturated and dry clastic silicate sedimentary rocks, mudstones, etc). Miller (1996) presented results for two different field studies, calculating values of Vp/Vs for different formations and consequently different lithologies. Plots of Vp/Vs versus gamma ray values can give a trend related to clay or shale content; in general, there is a small increase in the ratio for sands with increase in clay or shale content. In the same way, the Vp/Vs and PEF logs increase as the limestone fraction versus dolomite increases. Emery and Stewart (2006) found consistency in their results with Castagna (1985) mud rock line and also they found a value for Vp/Vs of 1.75 to differentiate a clay or calcite-rich bed from a quartz-rich deposit. Stewart (2003) put together some of the conclusions from different authors in Vp/Vs relationships with lithology.

Porosity and pore aspect: In many occasions porosity is the main controller of velocity values especially as it is usually accompanied by a change in other rock properties (e.g., pore shape, density). It is difficult to define an unambiguous effect of porosity on velocities. Generally both P- and S-wave velocities are inversely proportional to porosity for a broad range of lithologies, burial depths, and pore fluids (Figure 1-12). A decrease in velocity is due to the decrease in shear modulus of the rock matrix which is affected by increase in porosity. Pore fluid composition affects both P-wave and S-wave velocities in a different way. Shear velocity of rocks is affected by the fluid only due to the change in density; the shear modulus of all fluids is zero. An increase in density produces a decrease in velocity. This is also true for P-wave velocity but the bulk modulus of the pore fluids has a greater effect which compensates any changes in density due to change of fluids into the pore space. Then the velocity will increase due to an increase in the bulk modulus of the pore fluids even if the density also increases (Tatham and McCormack, 1991).

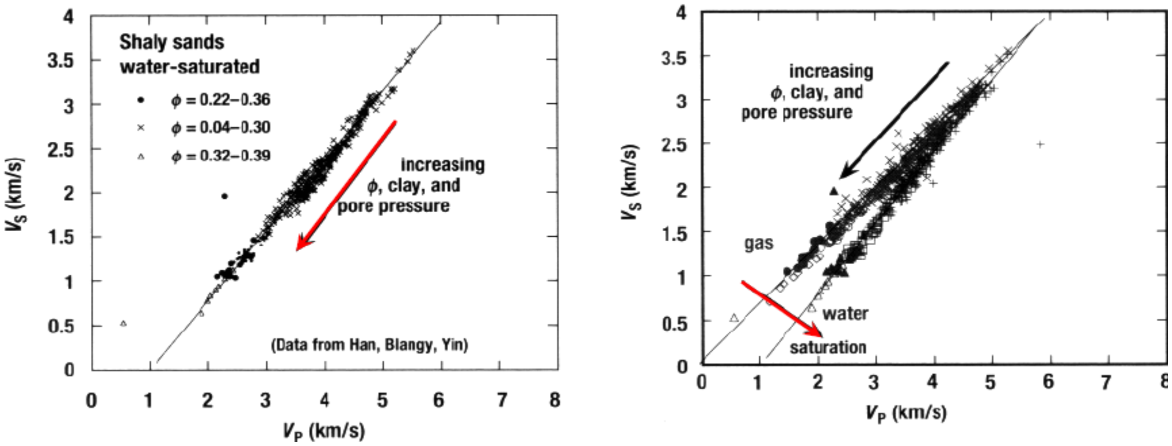

Figure 1-12. Vp vs Vs for water saturated sandstone (left) and water and gas saturated sandstone. From Avseth et al., (2005).

Miller (1990) found a particular case where for some sandstones Vp/Vs decreased with increasing porosity; this is different to what is reported by other authors. For limestone Miller found a decrease in Vp and Vs as porosity increases, but the ratio had little change with porosity. Castagna's (1985) relationships show that Vp/Vs for sandstone increases with increase in porosity and clay content, being more sensitive to porosity. Figure 1-12 shows the particular trend of some data (data from Han (1986), Blargy (1992) and Yin (1992)) in spite of porosity, clay content and effective pressure variation.

Eastwood and Castagna (1987) found that Vp/Vs for quartz-water and quartz-shale-water systems depends on porosity and is relatively independent of pore aspect ratio, for a high aspect ratio (0.05-1.0), but it depends on both for lower aspect ratios. There are two cases where velocity could be affected by pores of low aspect ratio: in overpressured formations and with shaly-sand formations where it is not clear the type of pores present. Higher than expected Vp/Vs is indicative of overpressure zones. They also concluded that porosity has little effect in Vp/Vs for limestones and dolomites.

Kuster and Toksoz (1974) generated equations to relate porosity, aspect ratio and elastic properties to Vp and Vs for an impermeable rock. Laboratory studies agree with the results of these equations. In general, Vp decreases with increase in porosity and aspect ratio. Poisson's ratio decreases for gas-filled sandstone and increases slightly for water filled sandstone with increasing in porosity.

Milller (1992) did a specific study on the relationship between seismic velocities and porosities in carbonates. No particular trend was found in the three formations studied from Alberta. As the relationships between rock properties and velocities are complex in carbonates, it is recommended to undertake individual analyses on the formations of interest.

Pore fluid content: P-wave and S-wave velocities are approximately constant for mixture of gas and liquid up to about 90 % liquid saturation. At higher liquid saturation, Vp increases strongly due to rapid increase in the fluid bulk modulus. Vs does not change with fluid saturation, except when pore fluid density changes for different gas saturations. For oil and water, Vp responds differently; it increases monotonically as the saturation of water increases due to the increase in fluid bulk modulus. Oil and water in the pores will show more variation of Vp/Vs with changes in water saturation. However, a good stratigraphic knowledge of the reservoir is required to determine the cause of changes in Vp/Vs: oil-water variations or lateral porosity/lithology changes (Tatham and McCormack, 1991). Castagna (1985) found a linear relationship between compressional velocity and shear velocity for water saturated and dry clastic silicate rocks. For dry sandstone, Vp/Vs is nearly constant.

Differential pressure and depth of burial: Most of the changes in Vp/Vs occur in the first kilometer of depth. Sandstones are more affected by this factor than limestones as in the case of porosity. In general, Vp/Vs decreases with increasing differential pressure (Tatham and McCormack, 1991).

Near-surface Vp/Vs: Stumpel et al., 1984 presented a study about the use of shear and compressional waves for lithology problems in the near-surface. They confirm some differences of shear waves and compressional waves, including that shear waves are not affected by water saturation, they have lower frequency but shorter wavelength therefore better resolution of thin layers, and they have lower absorption (Q_s^{-1}) hence better penetration through partially saturated and gas-containing sediments than P-waves. They studied data from a 3C refraction survey (SH and P mode) between distances of 20 m to 500 m, where the P-wave detects dry sand with 300 m/s, saturated sand with 1500 m/s and boulder clay with 2200 m/s, and SH-wave shows one layer with 150 m/s (dry and saturated sand) and the boulder clay with 450 m/s. High velocity ratios (4.8) for the saturated sand and boulder clay were found. Another example showed in this paper found high Vp/Vs (3.6 – 4.5) below the ground water level and in the upper part of a boulder clay section from borehole measurements.

Carvalho et al. (2009) presented a paper that evaluates the most interesting and useful geotechnical near-surface parameters through P and S-wave refraction surveys and standard penetrating tests (SPT). Vp/Vs and Poisson’s ratios were calculated and a classification of the subsoil is presented in this paper. Two layer were identified in their area of study with Vp/Vs varying from 1.46 to 3.26 for the first layer and 1.47 to 7 for the second layer. The highest velocity ratio coincides with the profiles where the water table is very shallow. They described the soil condition based on S-wave velocity and layer thickness.

Richardson and Lawton (2003) presented a study about the Vp/Vs behaviour in the near-surface. The study area is located in Red Deer, Alberta and they found high values of Vp/Vs (~5) in the shallowest strata down to 100 m. The highest value was 4.7 at 40 m depth. The information was obtained from vertical seismic profiles and compared to values from seismic data and well logs. This result agrees with the general trend of Vp/Vs which is usually high in the near-surface and decreases with depth.

1.5 PP – PS survey acquisition design

The objectives of 3D seismic surveys include producing enhanced seismic data for structural and stratigraphic interpretation, help in solving fine-scale reservoir architecture or fluid contacts or it could be used as a base data to be compared to a later seismic data to detect movement of fluids. All of these products of seismic data rely on processing, which relies on good acquisition practices (Ashton et al., 1994). One way to evaluate survey design is to consider the properties of the CMP bin: Offset distribution, azimuth distribution and fold. For example, Vermeer (2002) gives more importance to the spatial properties of a given geometry across the bins. Spatial continuity, resolution, shallowest and deepest target to be mapped and the signal to noise are the most important requirements.

Ashton et al. (1994) consider three important elements to obtain good seismic signal: good signal-to-noise ratio (S/N), high resolution power and adequate spatial sampling of the target. These elements and other geophysical rules form the basis of survey design. High S/N can be obtained during acquisition by using a source with high power and directivity and by minimizing noise. Adequate geometry should be selected to avoid spatial aliasing (ambiguity in the signal due to under-sampling) of the signal and to attenuate noise. Stacking is a processing technique to reduce noise and improve signal in the data; this technique sums the reflections at a common midpoint (CMP); to obtain good results, every CMP needs a wide and uniform sample range of source-receiver offsets (distance) to define the travel-time curve, known as normal moveout (NMO) curve and be able to apply precise NMO corrections. Fold is another important factor, which is the number of traces (reflections) in a rectangular space in the subsurface called a bin. There is an optimum value of fold beyond which only small improvements can be made in the data. This value is usually taken as half the fold of 2D seismic data (Ashton et al., 1994). Fold controls the signal-to-noise ratio (S/N); Increase in fold will increase the S/N but it is not a linear function. Fold increases as the (S/N) squared (Cordsen, 2000).

Adequate subsurface coverage is reached by choosing appropriate lateral distance between CMP’s at the target (bin dimension). The minimum source and receiver interval should be twice the CMP spacing at the target for a flat reflector. Target size is related to spatial sampling (due to target dip) and this one is related to bin size (Neidell, 1994). Two to three traces are needed to image a small target (bin size equal or less than target size divided 3); this is a first approximation to bin size (Cordsen, 2000). Vertical and lateral resolution requires a specific bin size, $\Delta X * \Delta Y$. This can also be taken as the radius of the Fresnel zone or larger for a flat reflector. The Fresnel zone is the portion of a reflector from which reflected energy arrives to a receiver within a half-wavelength of the prior reflections (Ashton et al., 1994). For a dipping reflector:

$$\Delta X = \frac{V_{rms}}{4 f_{\max} \sin \upsilon} \qquad \textbf{(1.22)}$$

Where V_{rms} is the root square average of velocities to the target, f_{max} is the maximum non-aliased frequency necessary to resolve the target, and υ is the target dip. Normally, ΔX=ΔY. The bin size controls the sampling of the wavefield and care should be taken to avoid spatial aliasing (ambiguous sampling of the wavefield) especially when sampling dipping events (Cooper, 2004; Cordsen, 2000). The sampling interval should not be larger than half of the smallest wavelength period ($\Delta x = 1 / (2k_{max}) = V_{min} / (2f_{max})$) but this criteria leads to a very small interval which is very expensive and no practical (Vermeer, 2002). This criterion is relaxed in order to satisfy equation 1.22

Other parameters to be considered when planning a 3D survey are: size and shape of the survey, minimum coverage (fold) to image the objective, maximum source-receiver offset, source/receiver line spacing, etc (Cooper, 2004). The survey area should be such that full fold is obtained over the target, sometimes this means an increase in the area to record reflections from dipping layers (the distance between sources and receivers should be larger than if the target is flat) or capturing area around the area of interest, especially in areas with complex geology to help in the interpretation of complicated structures (Cooper, 2004; Cordsen, 2000).

The desired 3D fold is determined from previous seismic data, usually 50 % of the value from a reasonable good 2D seismic survey (Neidell, 1994) or it could be a factor of the 2D fold:

$$3DFold \geq 2Dfold \sqrt{\frac{\Delta X \Delta Y}{2 R_f \, dx}} \qquad \textbf{(1.23)}$$

Where R_f is the radius of the Fresnel zone and dx is the CMP interval in the 2D data (Ashton et al., 1994). Krey (1987) showed an expression for 3D fold as directly proportional to 2D fold and frequency. Lansley (2004) stated that fold is not important as a number without specifying the bin size. A better number to consider is the trace density which is number of traces per unit area. The requirements of even offset distribution and not duplicating source-receiver trajectories still should be met.

A widely accepted expression to estimate 3D fold is:

$$3DFold = \frac{\pi X_{\max}^{2}}{4(SL)(RL)} \tag{1.24}$$

Where SL and RL are the source and receiver line interval, respectively and X_{max} is the maximum offset. This expression gives the nominal fold considering the bin size as half the source by half the receiver interval and assumes that all the traces contribute to the fold (include traces that will possibly be muted in processing).

It is also desirable to acquire wide offset and azimuth distributions in order to estimate a good velocity field and to minimize artefacts generated during data processing (Neidell, 1994). A first approximation to the maximum offset is making it equal to the target depth (Cordsen et al., 2000). For shallow targets, the maximum offset is limited by interference of the first breaks with the actual reflections; in processing, these first breaks are muted and with them, some reflections are also lost. Another factor to be considered is the stretch mute, which is applied due to wavelet distortion (data with greater than ~15 % stretch are eliminated). For deep targets, the critical factor is the loss of reflection amplitude (Cooper, 2004).

Source/receiver line spacing is controlled by the shallowest reflector i.e. the largest minimum offset (X_{min}). This distance should be shorter in order to have a minimum fold at this shallow event (Cordsen, 2000). These line spacings can be estimated from equation 1.24 knowing the desired fold and the usable offset range. Cooper (2004) gives some ranges for SL/RL in order to preserve image quality.

For PS survey design, the difference relative to PP mode is in the reflection mode raypaths; local propagation velocities, reflection strength and attenuation are different. The temporal frequency content is the same between the incident and reflected wave, for both PP and PS modes. In contrast, wavenumber changes when there is change of mode, such as for converted waves. In this case, the wavenumbers of reflections are larger than the incident waves. Furthermore, the amplitude of the reflected wave behaves differently with reflection angle depending on mode change (Meier, 2009).

More information is required for a PS survey design than for a PP survey design. A preliminary 2D multicomponent line is helpful to obtain more information about shear wave velocity, attenuation and other information. It also allows the assessment of efficiency of the PS method to obtain the desired results.

The sampling theorem states that band limited data can be reconstructed if they are sampled at least two or more times per cycle for the highest frequency present. This is called the Nyquist theorem and the largest sampling interval that satisfies it is given by

$$\Delta X = \frac{V_\alpha}{2 f_{\max}(1+\gamma)(\sin\theta_i)_{\max}} \qquad \textbf{(1.25)}$$

V_α is the velocity of the incident wave, γ is the ratio of velocity of the incident waves to the velocity of reflected waves and θ_i is the incident angle (Meier and Lee, 2009). Notice that this equation is the same as the equation 1.22 which is the expression for PP mode as the ratio of velocity (γ) would be equal to 1 as there is no mode conversion. The sampling requirement for PS surveys is typically more severe than for PP surveys because the ratio of converted wave sampling to common wave (PP) sampling is less than 1. This is $\Delta X_{PS}/\Delta X_{PP} = 2/(1+\gamma)$, (Meier and Lee, 2009).

Some other authors have written on the subject of bin size for converted waves. Eaton and Lawton (1992) concluded that using conventional bin size equal to half the receiver spacing (as in PP) will produce irregular fold distribution. They recommended to select a source spacing as an odd number of receiver spacing multiplied by the expected compressional to shear velocity ratio to improve the fold distribution. Lawton (1993) showed that the natural bin size is given by the expression:

$$\Delta X = \frac{\Delta r}{1 + {}^{Vs}\!/\!_{Vp}} \qquad \textbf{(1.26)}$$

Where, Δr is the receiver interval. Using this expression in conjunction with asymptotic binning (this is a technique to bin converted waves) produces a uniform coverage (fold) distribution. Smooth coverage is required to have strong post-stack amplitude analysis and it is very important for pre-stack amplitude versus offset (AVO) analysis. Lawton et al. (1995) discussed the design of 3C/3D for the Blackfoot survey. As the asymptotic method for binning produces variations in fold from bin to bin, a bin fractionation was used in this case, known as Flexi-bin®. This technique uses source and receiver line interval which are not integer multiples of the receiver interval and distributes the conversion points at even 10m by 10m bin sizes. Fold maps were generated at different depths showing the variations of fold with Vp/Vs.

Cordsen and Lawton (1996) showed a method to use the same bin size for PS stacks as for PP wave stacks keeping the quality of the design. It uses the Flexi-bin technique which produces uniformity in the midpoints for both wave mode stacks allowing the use of constant bin sizes.

Another difference between PP reflection mode and the PS mode is that the reflection point is not centered between source and receiver points (Figure 1-13). The domain of analysis changes from common midpoint (CMP) to common conversion point (CCP).

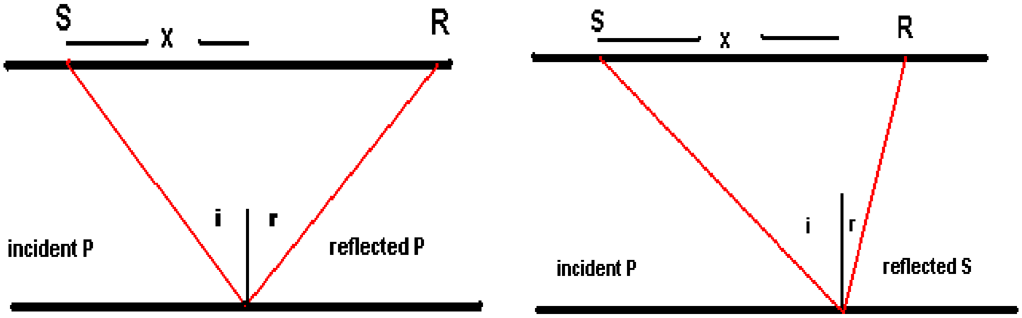

Figure 1-13. Schematic of common midpoint (left) and common conversion point (right). (From course notes).

The conversion point lies closer to the receiver points and depends on Vp/Vs and depth; one of the algorithms to locate the conversion points assumes an asymptotic trajectory not considering the depth (proposed by Fromm et al., 1985), as follows:

$$X \approx S + \frac{r - s}{1 + {}^{Vs}\!/_{Vp}} \tag{1.27}$$

Where Vs and Vp are the average S- and P-wave velocities, s is the source position and r is the receiver position.

The asymptotic conversion point (ACP) has an error in location that decreases with target depth (Lawton, 1993); it is adequate for offset smaller than half the target depth, but as this ratio increases, the conversion point moves towards the receiver and the error in location increases. Another algorithm to locate the conversion points at a specific depth uses ray tracing for a given velocity model (Lawton et al., 1995). This is called depth-specific conversion point (DSCP). Figure 1-14 is a schematic of both conversion point location types. Lawton and Hoffe (2000) showed an example where DSCP binning produced better results than asymptotic conversion point for an ocean bottom cable (OBC) 4C-3D seismic survey design.

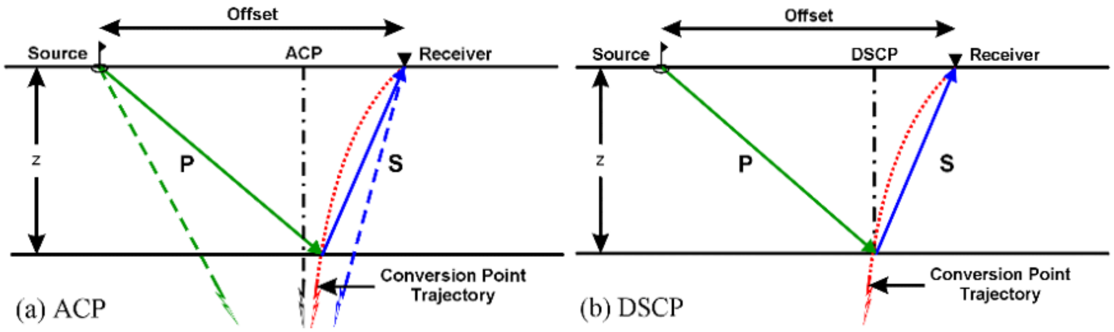

Figure 1-14. Conversion point binning. a) asymptotic conversion point (ACP) and b) depth-specific conversion point (DSCP). From Lawton and Hoffe (2000).

PS acquisition imaging of areas with weak PP reflection response but strong PS response due to large reflection angles and corresponding offsets of PS mode is potentially another of its advantages. Larger offsets should be considered during design. With larger offsets, the requirement of denser sampling is relaxed and the migration aperture increases. Typically, PS acquisition requires a greater aperture than the PP method and this difference tends to increase with larger offsets (Meier, 2009).

1.6 Objectives of this thesis

The dataset used during this study includes a multicomponent refraction survey and a well log from the project area. SH-wave data and P-wave data were used for the refraction analysis, which provided the near-surface velocity-depth structure required to calculate static correction times to be used during the processing of reflection data. This step improves the result of residual static corrections because correlation across common midpoint depends on the quality of the input data; refraction static corrections resolve intermediate and long wavelength static anomalies (Lawton, 1989). P-waves and SH-waves difference in sensitivity allow detailed description of the subsurface as shear waves are insensitive to fluids, slower than P-waves and polarized.

Acquiring shear and converted wave data enabled making PP to PS registration, from which the Vp/Vs values for the structures of interest is obtained. These values were compared with those obtained from the well log available in the area which included data from 40 m to 2054 m. Vp/Vs is a very important tool for lithology identification and shear-wave data help in differentiating between lithologic or fluid changes in the subsurface. Elastic rock properties can be estimated by doing combined interpretation of PP, SS and PS data (Garotta et al., 2002).

The main objective of the study was to elucidate the near-surface P- and S-wave velocity-depth structure. This model will help in the processing of a 3D/3C seismic survey that will be acquired in this area, and to provide constraints on registration of PP and PS volumes. Another objective was to do Vp/Vs analysis for shallow and deep formations. Also, the PS survey design was evaluated to guarantee the quality of the data to be acquired with the 3D/3C seismic survey. The methodology followed was:

- Refraction analysis through the plus-minus time analysis method. Once the velocity-depth structure of the near-surface was obtained, the static corrections were calculated and compared with the results obtained by Sensor Geophysical that carried out the processing of the data.
- Vp/Vs analysis. With the velocities obtained from the refraction analysis, the velocity ratio was calculated for the near-surface and compared with well log

data. Also, PP to PS registration was performed which allowed the estimation of Vp/Vs for deeper structures and again compared with the deeper information from the well log.

Analysis of fold, offset and azimuth distribution for the PP and PS survey was performed, with emphasis in footprint effects.

1.7 Hardware and software used

Rotation of the horizontal components and first break picking were performed using Vista software. The plus-minus time analysis was performed through an automatic code available and also using Excel spreadsheets. The interpretation and event registration to obtain Vp/Vs was performed with Hampson and Russell software. Finally, Omni software was used for the 3D survey design.

Chapter Two: **GEOLOGY**

2.1 Surficial geology

The study area is located in northeastern British Columbia (NEBC). The surface of the area is mainly tills rich in clay and glaciolacustrine sediments. In some places, these deposits completely cover glaciofluvial sands and gravels. A common feature in the region is the presence of thick organic deposits in poorly drained areas. Not that common is the presence of glaciofluvial deposits at surface but sometimes they occur within or near large melt-water channel systems (Levson et. al. 2005).

There are some indications, from radiocarbon dates, that the last glaciation in the region was Late Wisconsian. Other than that, the timing is inadequately defined in the Late Pleistocene. Fossiliferous organic sediments have been found under the till in the area of study suggesting a paleoclimate fairly similar to the present. Those sediments are possible Sangamonian age. The area had no glaciers until after about 24 ka radiocarbon years BP and it is believed that ice free conditions persisted from then until well before 40 ka (Levson et al., 2004).

2.2 Bedrock geology

A shallow stratigraphic column of the general study area is shown in Figure 2-1. The Fort St John Group and Dunvegan Formation are the main bedrock units for this area of study which are Cretaceous shales and sandstones (Hickin, 2005). The Banff Formation (Missisipian), the Debolt unit of the Rundle Group (Missisipian), the Spirit River and Buckinghorse formations from the Fort St John Group (Lower to Mid Cretaceous) and the Dunvegan Formation (upper Cretaceous) are the subsurface units of interest.

The Banff Formation consists of shales and marlstones that turn into spiculite, bedded chert and carbonates towards the surface and east. The shallower portion of this formation is a sequence of interbedded sandstones, siltstones, and shales (Glass, 1997). The thickness of the Banff Formation in this area is around 140 m. The Rundle group comprises the Pekisko, Shunda and Debolt formations. The Pekisko consists of limestone; the Shunda is formed by a sequence of interbedded limestones, dolostones, siltstones, sandstones, shale and breccia. In northeast BC, the Debolt is mainly composed by limestone with less dolomite and shale.

The Fort St. John Group (Cretaceous) is underlain by the sub- Cretaceous unconformity. The lower Fort St. John Group consists of the Spirit River and Peace River formations. The Fort St. John Group is composed mostly of dark shale deposited in a marine environment. Bentonite is present in the shale, and it is interbedded with sandstone, siltstone and conglomerates. It has a thickness from 700 m to 2,000 m. The Buckinghorse Formation, also included in the Fort St. John Group in some areas, occurs north-east of the Canadian Rockies foothills in British Columbia. It is composed of silty marine mudstone with fine grained marine sandstone interbeds (Hickin, 2005).

The Dunvegan Formation is the upper-most unit in the area and consists of marine, deltaic and channel sandstones, conglomerate, and shale.

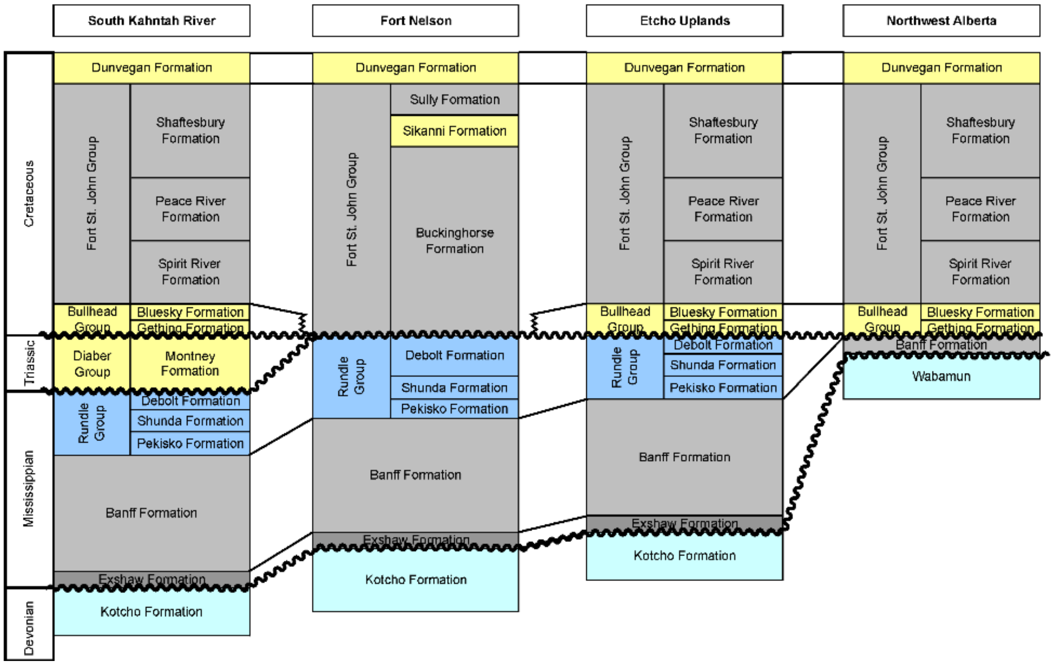

Figure 2-1. Bedrock and shallow stratigraphy of the area is transitional between the nomenclature from the northwestern plains of Alberta and that of the Fort Nelson area (after Stott, 1982 and Thomson, 1977).

Hickin et al. (2008) presented a new understanding of the bedrock in the area with a complex bedrock surface showing much higher relief and several deeply buried depressions believed to represent paleovalleys incised up to 300 m into the shales of the Fort St. John Group (Cretaceous). These valleys are bigger than modern valleys and they are filled with glacial, interglacial, and preglacial deposits. These channels are important as they may be gas or water reservoirs (Levson, 2008). They can be source of water for surface use and also for use in hydraulic fracturing of shales for gas production.

2.3 Deep geology

2.3.1 Geologic setting

The Horn River Basin and Cordova embayment are located in northeastern B.C., and extend northward into the Northwest Territories. They are limited by the carbonate platforms of the Middle Devonian Upper Keg River, Sulphur Point and Slave Point Formation. The Presqu'ile barrier reef was formed during the Middle Devonian period (approximately 375 million years ago), and can be found in Alberta, British Columbia, the Yukon and Northwest Territories (Figure 2-2). The reef consists of limestone and dolostone that were product of calcite mud and skeletons of organisms growing in the reef that were deposited and buried in this area of shallow and well circulated sea-water. The shales of the Horn River Basin and the Cordova Embayment originated from deposits of clays, fine siliceous (silica-rich) muds, and organic matter, in the deeper, poorly oxygenated waters. These shales were divided in The Evie, Otter Park and Muskwa shales and they contain enough organic material to be the source of natural gas, some of which has migrated into the Presqu’ile barrier (Ministry of Energy and Mines, Oil and Gas report, 2011).

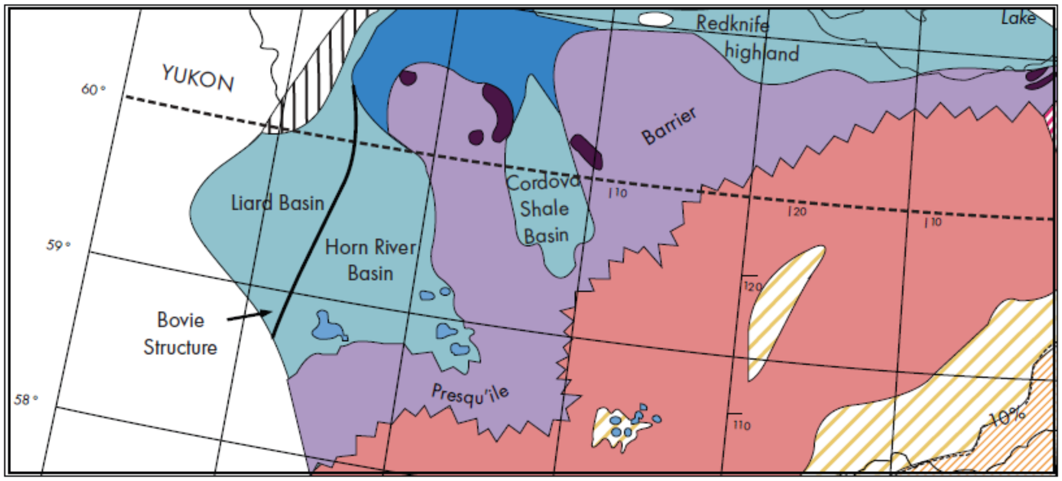

Source: Alberta Geological Survey

Figure 2-2. Location map: Horn River basin and Cordova embayment (from BC Ministry of Energy and Mines, 2011).

2.3.2 Stratigraphy and depositional history

Keg River Formation: The lower Keg River Formation is generally uniform in NEBC with 20 m to 50 m of thickness. In the north, Evie shales make up the upper part of the Keg River Platform. To the south, clastic deposits gradually replaced the carbonates. The Lower Keg River Formation is the beginning of a widespread marine transgression with relatively deep-water deposits. The Upper Keg River Formation, with thickness greater than 200 m, is a carbonate layer that forms the northern boundary of the Elk Point basin. This formation consists of continuous sequences, each with shale at the base, shoaling upwards and finishing with a thick carbonate at top (Petrel Robertson consulting, 2003). Figure 2-3 is showing the stratigraphic units in northeast BC.

Sulphur Point Formation: These carbonates were deposited over the Keg River in a period where there was a moderately slight regional transgression. This strata in this formation is uniform and it is found in most of the study area. The contact between the Sulphur Point and Upper Keg River is marked by an argillaceous facies. To the north, this unit is mainly limestone, especially towards the basin side of the Keg River barrier.

Slave Point Formation: It was deposited in the early stages of a basin-wide transgression. It is a carbonate platform including several repeated shallowing-upward periods that make it a complex structure. Reefal accumulations and carbonate deposits can be found at the edges of the main platform, and of the embayments inside the platform.

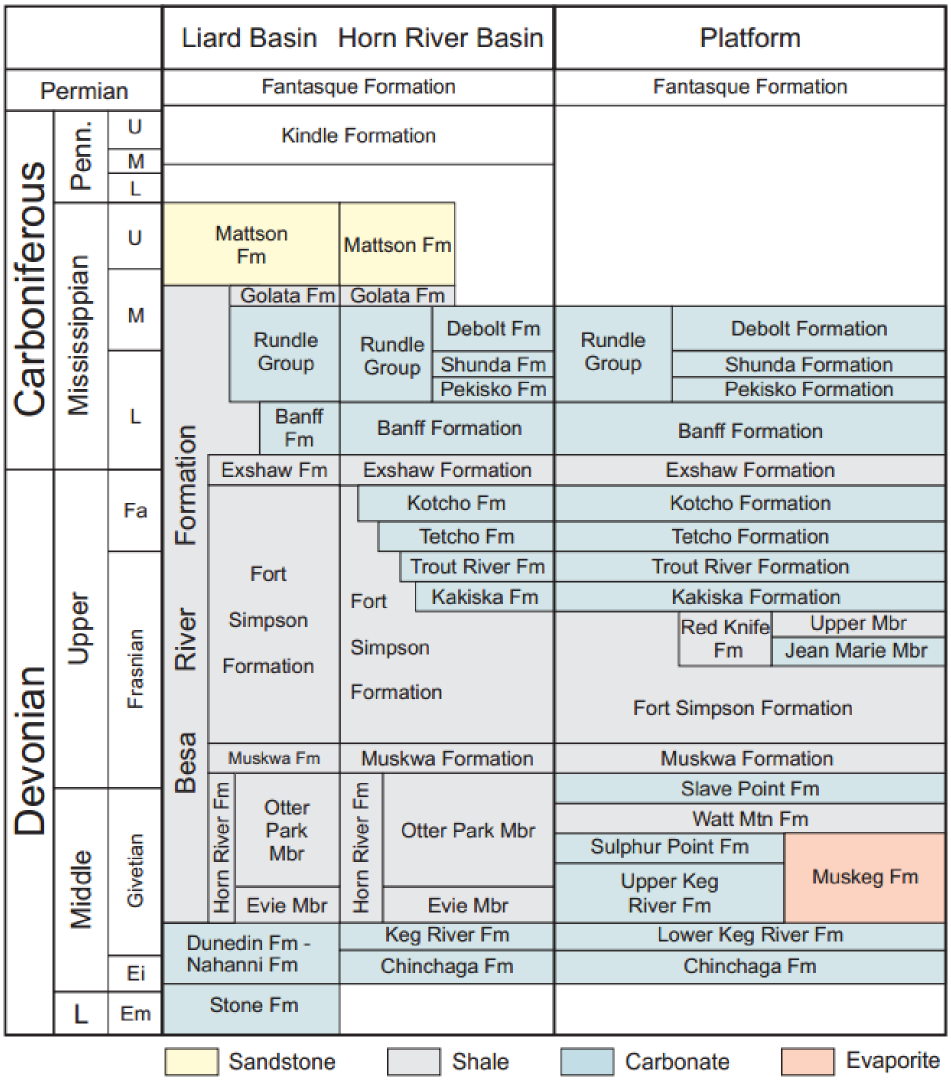

Figure 2-3. Stratigraphic column of the Middle to Upper Paleozoic showing main stratigraphic units along the sedimentary basins in northeast British Columbia (Ferri et al., 2011).

The Evie, Muskwa, and Otter Park formations are Middle Devonian shales forming the Horn River Group (Morrow, 2002). These are target formations for oil and gas exploration (Figure 2-4).

2.3.2.1 Evie Shale

The Evie/Klua shale is correlated with Elk Point (Keg River and Sulphur Point) carbonates. The Evie shales represent a starved basin facies due to water restriction from the Keg River accumulations.

The Evie Shale is dark grey to black, radioactive, rich in organic matter, pyritic, changeably calcareous (calcite-rich), and siliceous. High gamma ray and resistivity values are characteristics of this unit in well logs. Lower values of these log curves are detected in the upper part due to an increase in the silt content. The thickness of the Evie Formation varies from 75 m west of the Presqu'ile barrier reef, in the Horn River Basin, to 40 m to the west, close to the Bovie Lake Structure (western margin of the basin). The Evie Shale overlies limestones and dolostones of the Lower Keg River Formation (McPhail et al., 2008; BC Ministry of Energy and Mines, 2011).

2.3.2.2 Otter Park Shale

The Otter Park includes shales that loaded the Slave Point embayment and limited the Slave Point Platform. The Otter Park Formation is a medium to dark grey calcareous shale with lower radioactivity and resistivity on well logs than the Evie and Muskwa shales. This shale reaches over 270 m in thickness southeast of the Horn River Basin and thins to the north and west, increasing radioactivity in this area due to the presence of radioactive siliceous black shale beds (McPhail et al., 2008; BC Ministry of Energy and Mines, 2011).

2.3.2.3 Muskwa Shale

The Muskwa is part of the Upper Devonian Woodbend Group, and corresponds to the distal starved basin section of the Fort Simpson shales. This shale is grey to black, radioactive, rich in organic matter, pyritic and siliceous. High gamma ray and resistivity values are characteristics of this unit in well logs. The contact with the overlying shales (rich in silt and clay) of the Fort Simpson Formation is gradational. The thickness of this unit varies from 30 m adjacent to the Presqu'ile barrier reef to 60 m in the vicinity of the Bovie Lake Structure on the western side of the basin. In the Cordova embayment, the thickness ranges from 50 m to 70 m. The Muskwa thins in the southeast corner of the Horn River Basin where the Otter Park reaches its maximum thickness. This unit extends over the top of the barrier reef and is present through the rest of northeastern British Columbia (McPhail et al., 2008; BC Ministry of Energy and Mines, 2011).

Between these shales and the Banff Formation two important markers for the study area are seen in the seismic data: The Exshaw Formation and Jean Marie member of the Redknife Formation.

2.3.2.4 Exshaw Formation

The Exshaw Formation is a stratigraphic unit of Mississippian age and it is composed of black shale in the lower part, and siltstone and limestone in the upper part. It has a thickness of ~46 metres. The Exshaw Formation is unconformably overlain by the Banff Formation and unconformably overlies the Kotcho Formation.

2.3.2.5 Jean Marie Member

The Redknife Formation of Devonian age, is divided into the Jean Marie Member (base) and an upper un-named shale unit. The Jean Marie Member is composed of argillaceous, silty and dolomitic fossiliferous limestone. The carbonates are massive east of Fort Nelson and west of the Alberta border. The upper Redknife consists of calcareous shales with silty limestone and siltstone interbeds. To the south and east, the shales grade into limestone and siltstone, and it becomes dolomitic in the Peace River arch. The maximum thickness of the upper shales is 20 m, and the lower carbonates are up to 3 m thick.

Cross-section Showing the Horn River Basin

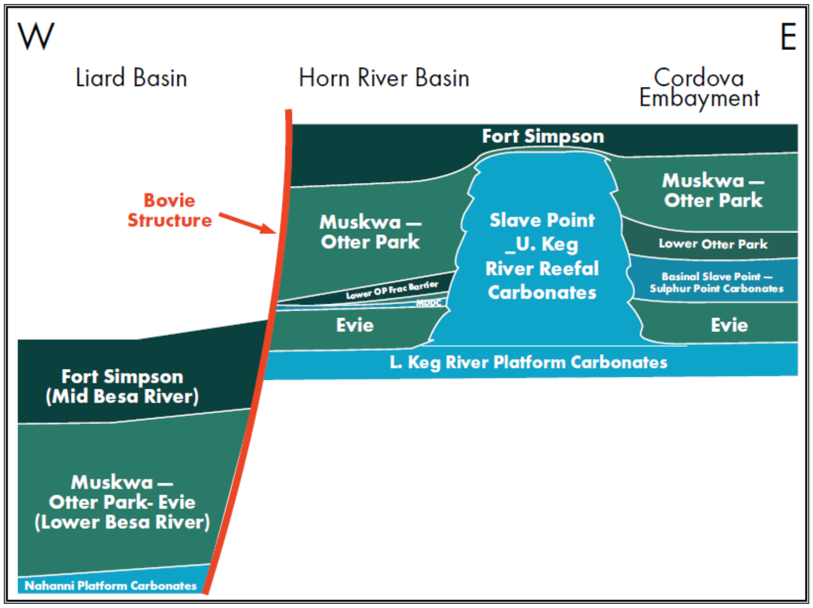

Source: AAPG Explorer

Figure 2-4. Cross-section showing the deep structure and stratigraphy of Northeastern British Columbia (BC Ministry of energy and gas, 2011).

2.3.3 Structural framework

The palaeography and reservoir development in the study area was influenced by the structural setting during Devonian time. Deep–seated faults, active during deposition, were the preferred location for basin margins and bank edges. Reactivation of these faults applied control over features of all sizes as platforms margins, interior platform embayments and localization of isolated reefal buildups (Petrel Robertson consulting, 2003). Faults were mapped on seismic lines, surface lineaments or regional isopach maps which coincided with aeromagnetic anomalies that were interpreted as major discontinuities (Figure 2-5).

The main fault trend detected in the area is the Bovie Lake fault zone. The Bovie fault began near the end of Devonian time and has a large displacement that increases from 700 m at Muskwa level to 1500 m at Exshaw level (Monahan, 1999; Morrow et al., 2001). The Bovie structure was generated by two separate events. The first event was the creation of the reverse fault, the Bovie fault which extends from the Proterozoic through the Upper Devonian Kotcho Formation. This fault forms the boundary between the Liard basin (west) and the Horn River basin (east). The second event was Laramide compression in Early Tertiary time that created a thrust fault with a decollement horizon near the top of the Banff Formation. East of the Bovie Fault is the Slave Point shelf edge (Morrow et al., 2001).

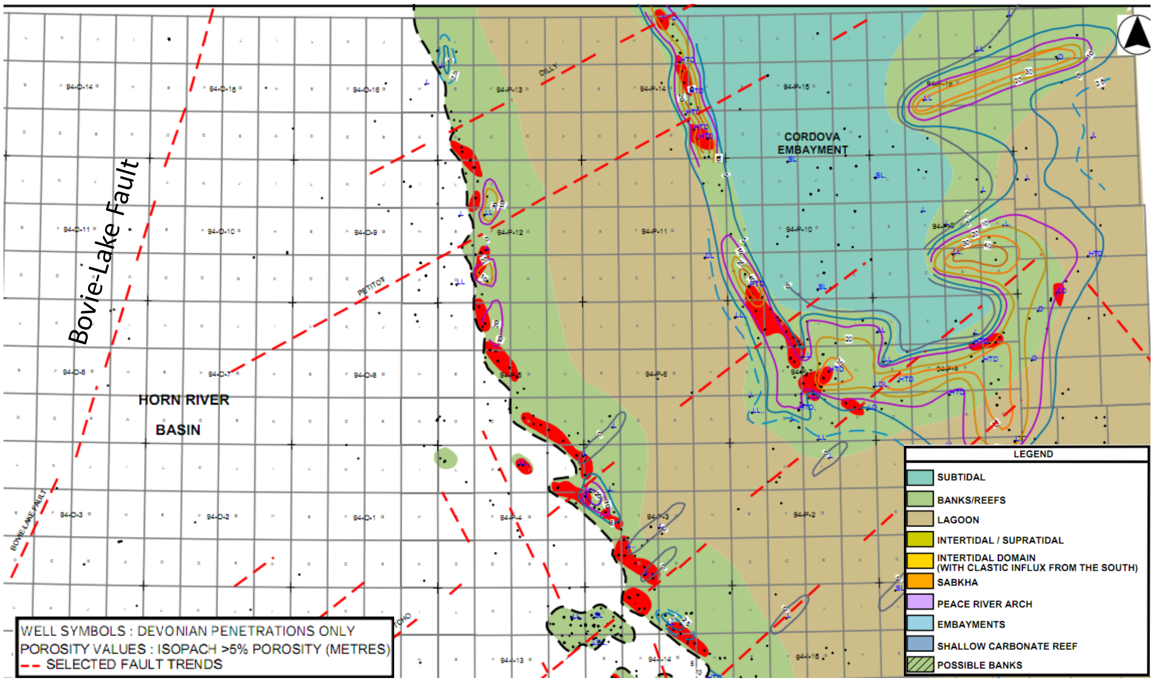

Figure 2-5. Slave Point palaeography and porosity (by Petrel Robertson for the BC Ministry of Energy and Mines).

Seismic lines crossing the Slave point shelf show a sudden change in structural elevation below the Slave Point shelf edge along the unconformity at the base of the Phanerozoic where Keg River to Slave Point strata goes into the Cordova embayment (Figure 2-6). As the shallow formations (Jean Marie, Tetcho and Kotcho) are not influenced by this structure, the time of faulting is constrained to the period between Slave Point and Jean Marie deposition (Morrow et al., 2002). Seismic lines do not detect sudden changes in subsurface elevation in the west margin of the Cordova embayment and the east of Horn River Basin.

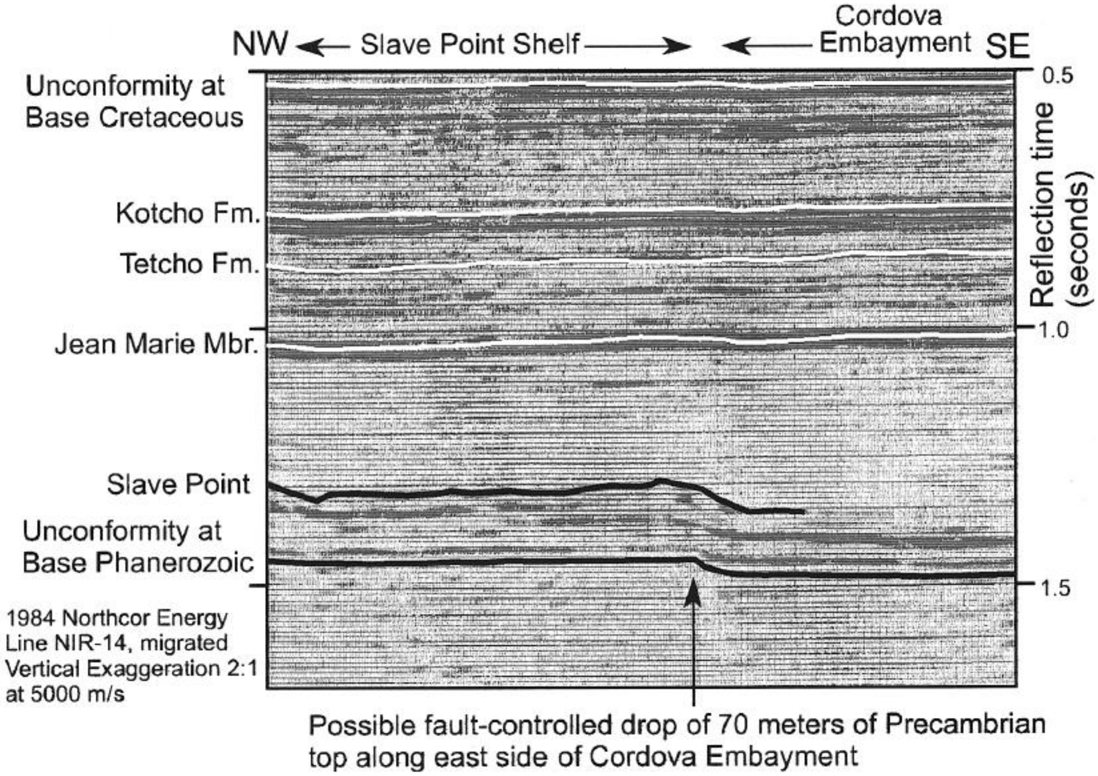

Figure 2-6. Seismic line showing the possible Devonian down-to-basin faulting (from Morrow et al., 2002).

2.4 Summary of this chapter

This chapter reviewed the regional geology in northeast British Columbia, including surficial, bedrock and deep geology. A brief description of stratigraphy, depositional history and structural framework has been included.

Chapter Three: **NEAR-SURFACE CHARACTERIZATION IN NORTHEAST BRITISH COLUMBIA (NEBC)**

3.1 Introduction

P- and S-wave data have been used before for near-surface characterization in order to calculate static corrections (Al Dulaijan, 2008; Martin, 2002; Parry and Lawton, 1993). Static corrections are used in the processing of reflection seismic data to remove the effect of low velocity in the shallow layer and the effects of surface elevation. The problem with statics is more severe in areas with glacial sediments due to their irregular thickness, which is the case in most of western Canada (Lawton, 1990) and also in Northeast British Columbia.

In this chapter, accurate depth and velocities are obtained in order to provide a detailed description of the near-surface structure. A refraction survey was acquired in the study area, from which three segments were analyzed for this thesis (Figure 3-1). The first segment comprised 43 shots with only a P-wave source (Line 101), the second included 90 shots with only an S-wave source (Line 103) and the third 220 shots with both P- and S-wave sources (Line 104). The vertical data (P) was the result of P-wave source recorded on the vertical component and the shear data (S) was the result of the shear vibrator on one of the horizontal components of the geophone. The shear vibrator polarization was transverse to the line azimuth, as a result the data used was from the transverse component. Rotation of the original data was performed to transform it into radial and transverse components. The field orientation of the H_1 component of the geophones was zero degrees (magnetic north). After rotation of the data, the first break arrivals were picked in VISTA software and these values were exported for the plus-minus analysis. Two methodologies were used: manual calculation with Excel spreadsheets and a software package available. Depth and velocities were obtained and from them static corrections were calculated.

Figure 3-1 shows the refraction lines used in this thesis overlain on a resistivity map from an airborne electromagnetic (EM) survey previously acquired. During an electromagnetic survey, an electromagnetic field is generated by a transmitter coil through which there is an electric current flow. The current flow generates a magnetic field around the coil (primary field). When this transmitter is located close to the earth, it induces an electrical field in the earth. The latter will flow through the earth at different strengths depending on the ground conductivity, generating a secondary magnetic field. There is a phase difference between the primary and secondary field that allows the separation of fields in the case of instruments measuring both of them. There are other instruments that measure only the secondary field. Changes in the measured field can be related to properties of the earth (Fetter, 1994). EM data can be used to detect high electrical conductance areas which are related to saline water and fresh groundwater would be expected where the conductance is low (Paine and Collins, 2003).

The primary or source fields used in EM prospecting are normally generated by passing alternating or pulsed current through long wires or coils. The EM mentioned in this study was TDEM (Time domain) where the disturbing field is measured after the primary field is eliminated by source cut off. The secondary field is small in comparison with the primary field.

Maxwell's equations can be used to understand the propagation and attenuation of electromagnetic waves. These equations relate electric and magnetic field vectors as follows:

$$\begin{aligned} &\nabla \times E = -\frac{\partial B}{\partial t} \\ &\mathit{and} \\ &\nabla \times H = J + \frac{\partial D}{\partial t} \end{aligned} \tag{3.1}$$

Where J is the current density (A/m^2), E is the electric field intensity (V/m), B is the magnetic flux density [teslas (T)], H is the magnetic field intensity (A/m) and D is the electric displacement (C/m^2). The first of equations 3.1 is a mathematical expression of Faraday's law that an electric field exists when there is a time-varying magnetic field and this induced emf is proportional to the negative change of magnetic flux. The second of equations 3.1 is an expression of Ampere's law (including Maxwell's displacement current $\partial D/\partial t$) where a magnetic field is generated by current flow and that field is proportional to the total current (conduction plus displacement) in the region (Telford et al., 1991).

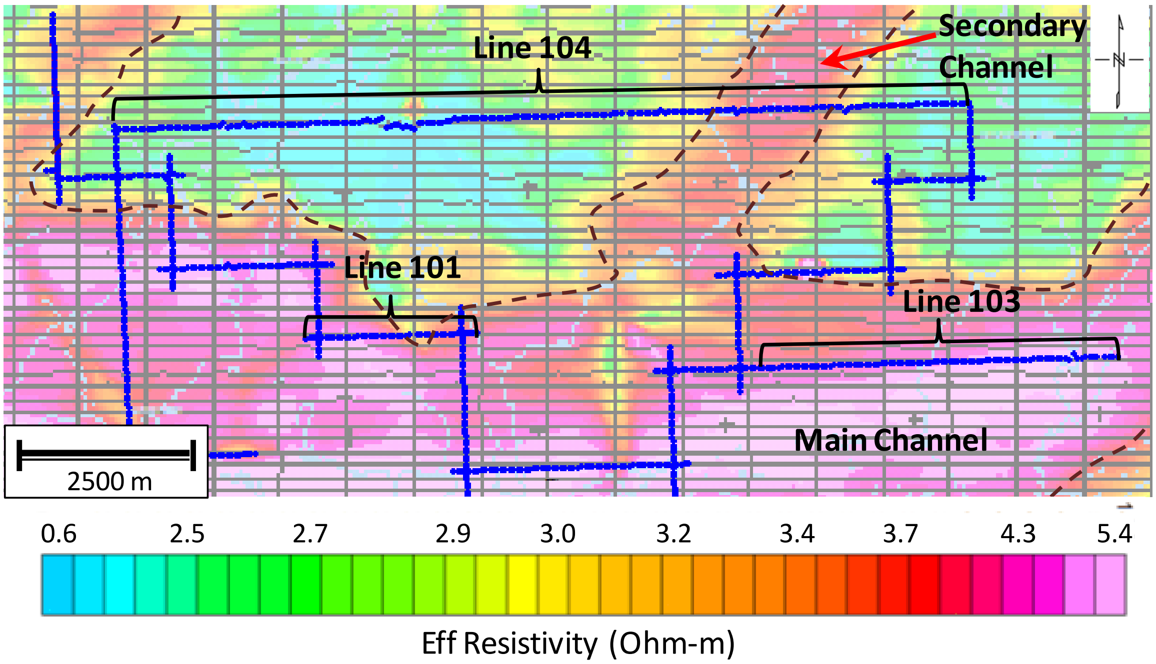

Figure 3-1. Refraction survey layout overlying the electrical resistivity map acquired in the area. Line 101, Line 103 and Line 104 were selected for the analysis.

The EM survey acquired shows interesting anomaly trends which cross the area of study and are delineated with dashed lines in Figure 3-1. This figure shows the result of the electromagnetic field converted to effective resistivity; this is a depth slice at 250 m. The pink colour represents high resistivity values, greater that 3.7 Ohm-m (low induced magnetic field, intensity lower than ~0.13 pV*ms/(A*m^4)) and the green/blue colours represent resistivity values lower than 2.7 Ohm-m (high induced magnetic field, intensity higher than ~0.23 pV*ms/(A*m^4)). The high values of resistivity are interpreted as channels, associated with sand, gravel and fresh water.

3.1 Acquisition parameters

The source-receiver offset range was chosen so that refracted arrivals observed from the target refractor were the first arrivals. The group interval was commensurate with the detail required, and the recording done was reciprocal (Cox, 1999). The minimum offset was only a few meters so that the direct arrivals were recorded on the near geophones and used to estimate the near-surface velocity.

Cox (1999) presented a table relating critical (Xcr) and crossover (Xc) distances with depth for different values of Vp/Vs for a simple two-layer case. These relationships were used to calculate the maximum source-receiver offset for the acquisition of the refraction survey. For this project, the deepest refractor expected was at around 300 m, therefore the crossover distance is estimated to be about 780 m (Xc ≈ 3.1 times the depth) when the refractor velocity is 4.0 times the near-surface velocity. The critical distance is 150 m (Xcr = 0.5 times the depth) that corresponds to the source-to-receiver offset when the reflected and refracted raypaths are identical. A refracted wave can be obtained only at offsets greater than the critical distance of 150 m but it is observed as first arrivals beyond the crossover distance of 780 m. In areas where several layers are to be mapped, it is likely that a larger offset range is required. The Cox (1999) table would be useful for refraction layout design if previous knowledge of velocity was available, but usually this type of survey is acquired to precisely find out these velocities.

The maximum offset used in this project was 1500 m. After analysing the data acquired it was concluded that longer offsets would be needed in order to accurately define the deepest refractor velocity. Longer offsets are needed to have an analysis window (section 1.2.1) wide enough to make the velocity calculations.

The geophone interval needs to be rather short (5-20 m) to obtain sufficient number of arrival times from the various velocity layers. For this project, a 10 m geophone interval was used, and P-wave and S-wave sources were used every 60 m along the line.

3.2 Rotation

Shear waves can be described in terms of polarization versus direction of propagation. A horizontal vibration oriented perpendicular to the in-line direction (particle motion purely horizontal) generates an SH-wave. If the horizontal vibration is oriented parallel to the in-line direction, the source generates an SV-wave, in isotropic media.

Shear wave data processing requires the rotation of the data acquired from the field coordinates to the radial-transverse coordinate system. The radial component (R) contains predominantly SV and P-wave modes, whereas the transverse (T) data are predominantly SH. 3D/3C surveys record data from different azimuths. The data at a specific receiver is a mix of SV, SH, (and P) waves on each horizontal component. The degree of "mixing" depends on the location (azimuth and offset) of the receiver from the source. Rotation based on source-receiver azimuth is necessary to obtain separation of SV and SH waves (Simmons, 1999).

The equations used for this rotation (Figure 3-2) were:

$$R = H_2 \cos\theta + H_1 \sin\theta \qquad (3.2)$$

$$T = H_1 \cos\theta - H_2 \sin\theta \qquad (3.3)$$

Where R is the radial component, T is the transverse component, H_1 is the component on the magnetic north orientation (MN), H_2 is the component on the magnetic east orientation (ME), and θ is the rotation angle.

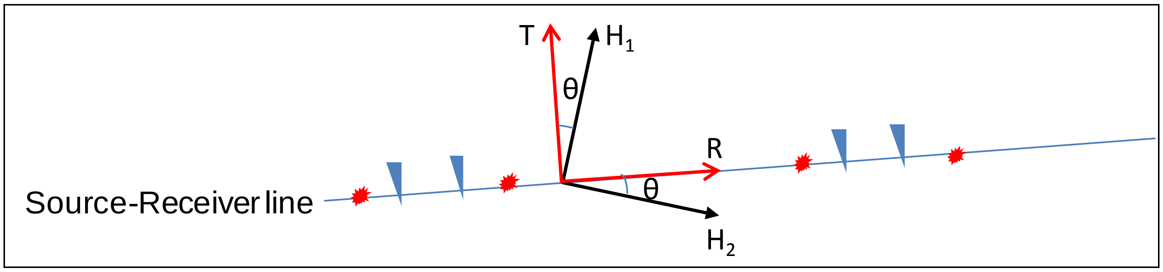

Figure 3-2. Receiver orientation. H_1 and H_2 correspond to the field orientation of the geophone components. R is the radial orientation and T is the transverse orientation (orientation after rotation of the geophone components).

The first step in the process was to determine the orientation of the receivers and the source as this information was initially not clear from the acquisition reports. The H_1 component of the geophone was oriented at zero degrees (magnetic); this information was taken from the observer's report which is generated by the refraction acquisition crew. The azimuth of the lines was 88° (from the refraction survey layout) and the magnetic declination in the area is 20° (from http://www.ngdc.noaa.gov/geomagmodels/Declination.jsp). The rotation angle is the angle between the transverse (T) component and the magnetic North, 22° in this case (Figure 3-2). Equations 3.2 and 3.3 were used to rotate the data from H_1 and H_2 to R and T components.

As the source was vibrating perpendicular to the line direction, maximum energy was obtained in the transverse component, i.e. SH-SH by convention. Examples of shot gathers before and after rotation are shown in Figure 3-3 to Figure 3-4. Note that the transverse component has more energy than the radial component, as expected. This is due to optimum coupling between the crossline vibrations and the transverse geophone component.

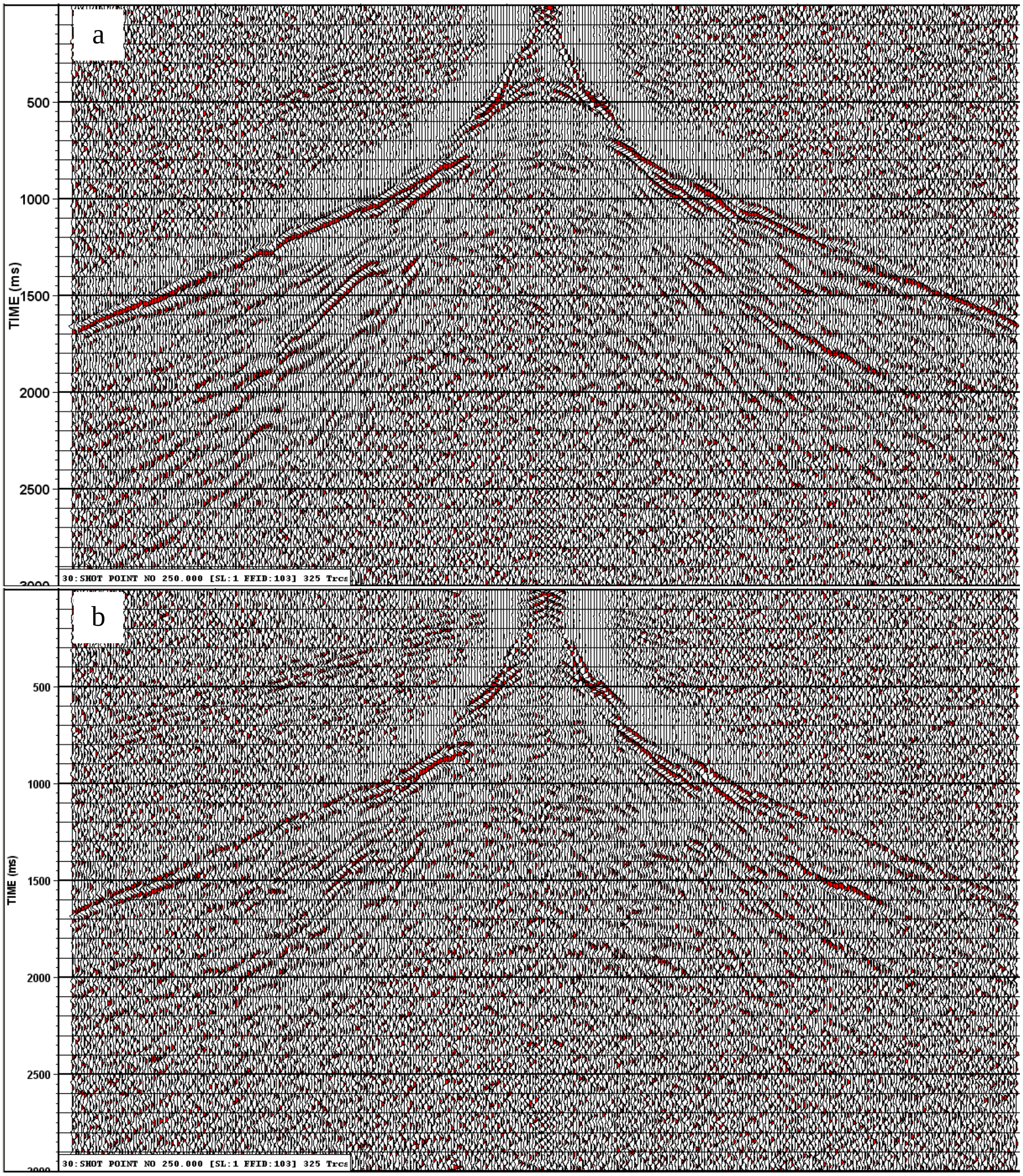

Figure 3-3. Example of a shot record from Line 104 (raw data). a) SH-H_1 data and b) SH-H_2 data. AGC with 500 ms window and band pass filter of 5-10-25-30 hz were applied.

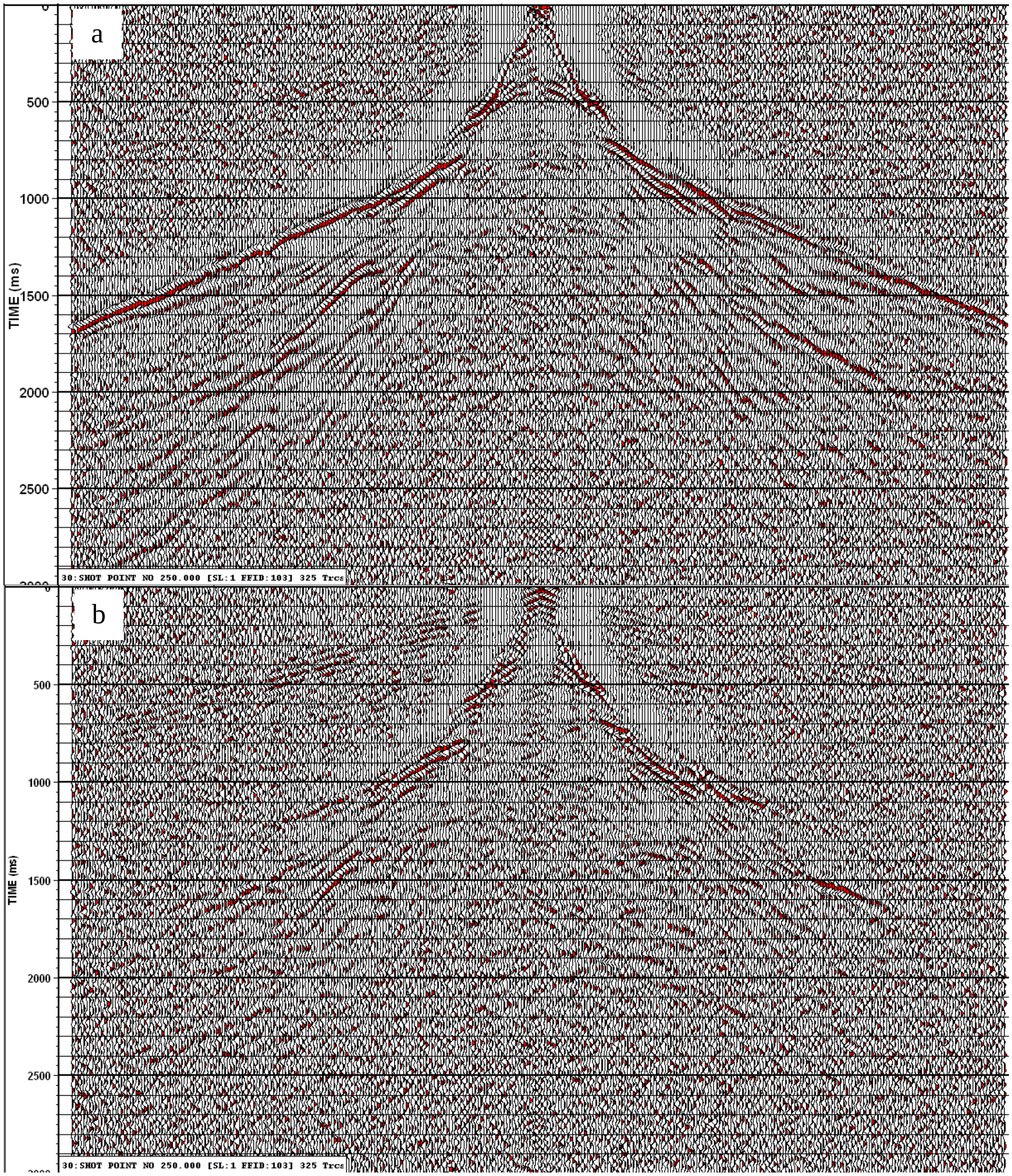

Figure 3-4. Example of the same shot record as in figure 3.3 (rotated data). a) SH-T data and b) SH-R data. AGC with 500 ms window and band pass filter of 5-10-25-30 hz were applied.

3.3 Velocity and depth analysis

The plus-minus time analysis method using both S-wave and P-wave datasets was applied to find velocity and depth structure of the shallow layers. After the rotation of the geophone components, the next step in the process was to pick first breaks in both datasets, shear-wave (SH) data and P-wave (P) data for three lines. Examples of these first break picks are shown in Figure 3-5. The quality of the data can also be appreciated; in general, the first breaks were easy to pick for the selected segments but there are other parts of this survey where the first breaks are difficult to follow. Automatic gain control with a window of 500 ms and an appropriate band pass filter were applied to each data set to enhance the first breaks (5-10-25-30 Hz for the shear data and 10-15-45-50 Hz for the P-wave data). Parameters of the three segments analysed are presented in Table 3-1.

Table 3-1. Description of data analysed from the refraction survey acquired in the area of study.

	Shot point range	**# of shots**	**Mode**
Line 101	260 – 302	43	P source only
Line 103	453 – 544	90	SH source only
Line 104	221 – 441	220	P & SH sources

The next step in the process was to export the first break times from all shots, to make time-distance curves, analyze the data and apply the plus-minus time analysis. Initially a manual approach was undertaken, using the following procedure:

Pairs of shots from the time-distance curves were chosen for the analysis along the line. In each case, the second shot was located at a distance greater than the crossover distance and inside the segment representing the refractor from which the velocity was being estimated, if this was possible. The reciprocal time (i.e. the time from shot 1 to the receiver at the position of shot 2) was read from the first break times coming from the refractor in consideration or in an extreme case, it was extrapolated when the offset was not enough or the refractor was too thin to yield only a few samples recorded from it. An example of this extrapolation is shown in Figure 3-6. The extrapolation was reasonable because the data showed consistency.

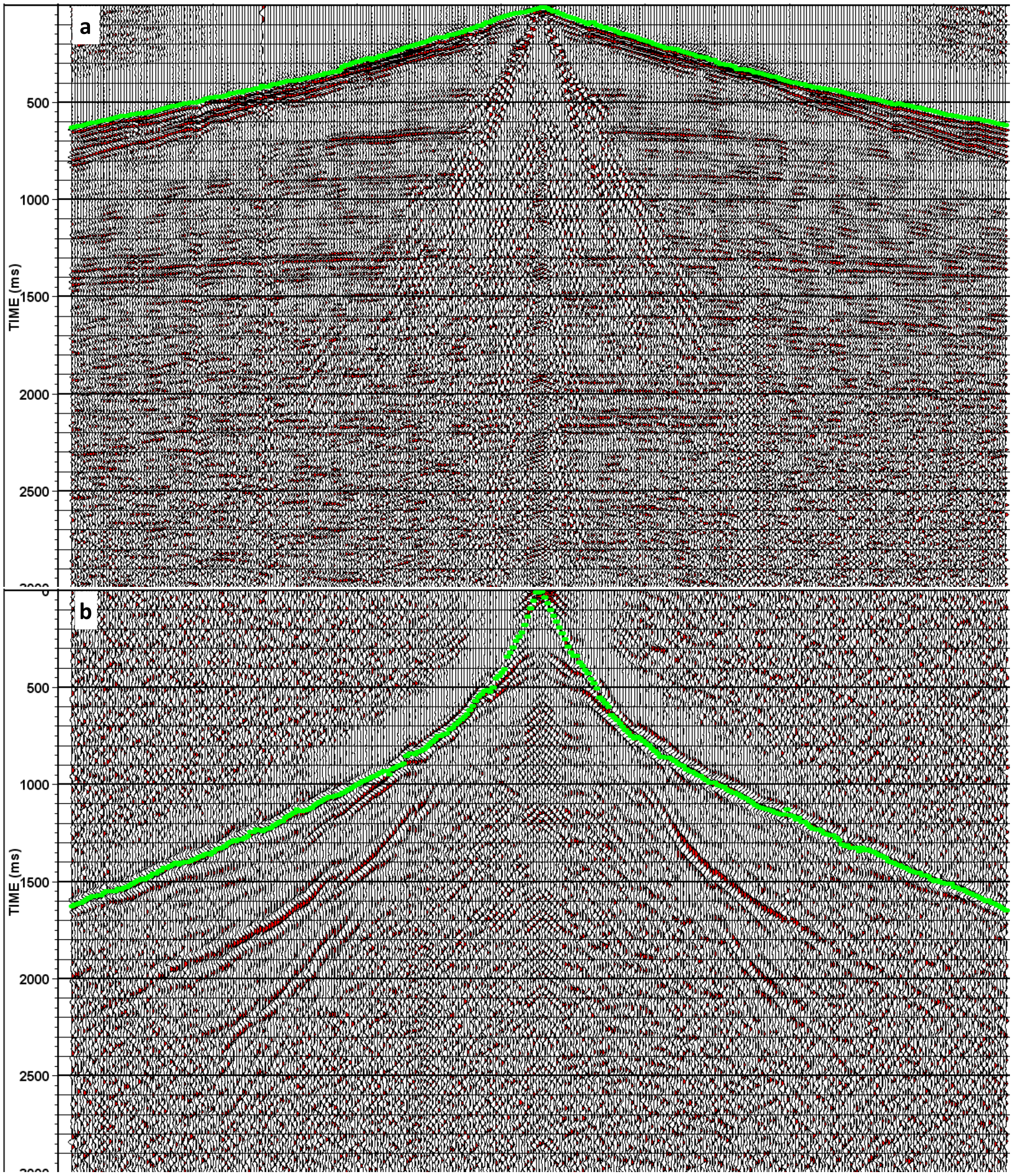

Figure 3-5. First break picks for (a) P-V data and (b) SH-T data for an example shot gather from Line 104. AGC with 500 ms window and band pass filter of 5-10-25-30 hz for SH-wave data and 10-15-45-50 hz for P-wave data were applied.

For each pair of shots, the plus-minus analysis window was established. This window (+/- window) is located between the crossover points and is indicated in Figure 3-6. The definitions of plus-times (equation 1.8) and minus-times (equation 1.11) were applied inside the analysis window at each receiver location.

After picking plus-minus windows, the velocity for the refractor in the plus-minus window was calculated. For the first layer, the velocity was calculated from the slope of the best fit line of the first break times coming from the first refractor (V_1 in Figure 3-6). The velocity for the other layers was calculated from the minus times analysis that requires a graph of minus times against distance. An example of this graph is shown in Figure 3-7 and the slope of the rectilinear part of this curve was used to calculate the velocity of the refractor. This rectilinear part also corresponds to the plus-minus analysis window.

Finally, the depth to the refractor was calculated from the plus times at each receiver within the plus-minus window. Equation 1.10 was used for the two-layer cases and equation 1.15 was used for the three-layer cases.

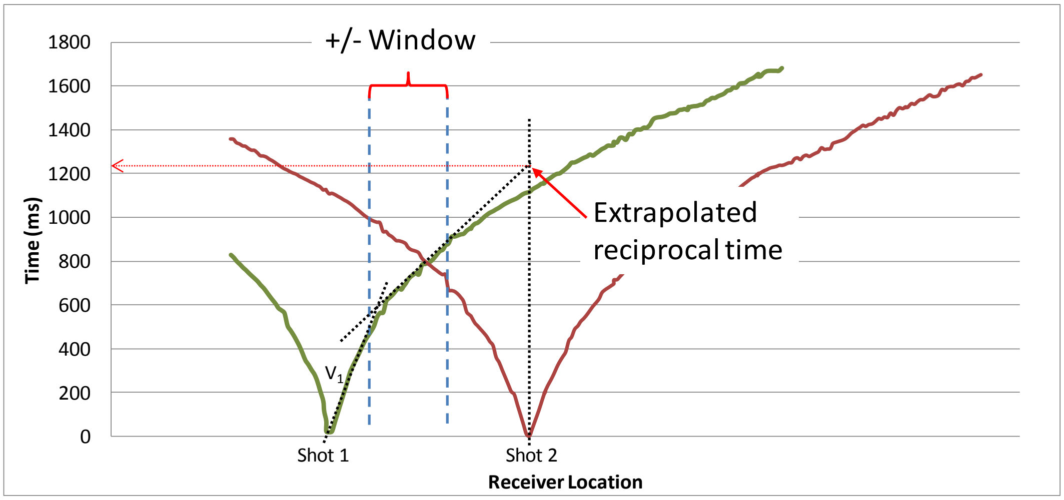

Figure 3-6. Example of a pair of shots to make the plus-minus analysis method (for the second layer) showing the +/- window and the reciprocal time required for the calculations.

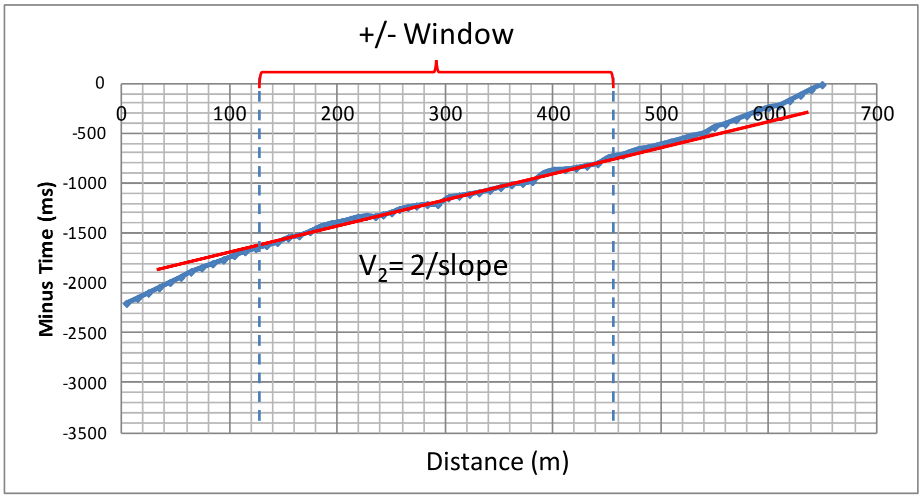

Figure 3-7. Example of T^- vs. distance graph to find V_2 from the minus times.

3.3.1 Analysis and results for Line 101, P-wave mode (43 shots)

Figure 3-8 shows an example of a shot record from Line 101 with the first-break pick times; the P-wave data has good quality for first arrivals as well as for the reflection events. The first break times from all shots were exported and used in an Excel spreadsheet to initially make graphs of times vs. location and after that, to apply the plus-minus time analysis method. This is a short line, so just a few plus-minus calculations were undertaken for the entire profile. Two layers were detected by analysing the first break time curves (Figure 3-9).

In this case, the reciprocal time, required for the plus-minus analysis, was extrapolated because pairs of shots for the analysis had to be chosen quite far apart so that an appropriate plus-minus window could be established. As mentioned before, the velocity for the first layer is the inverse of the slope of the best line that fits the direct arrivals to the receivers closer to the shot from the crossover point and, the velocity for the second layer is calculated from the minus times. The average velocity for the first layer varied from 1890 m/s to 1960 m/s and for the second layer ranged from 2700 m/s in the west to 2840 m/s in the east (Figure 3-10).

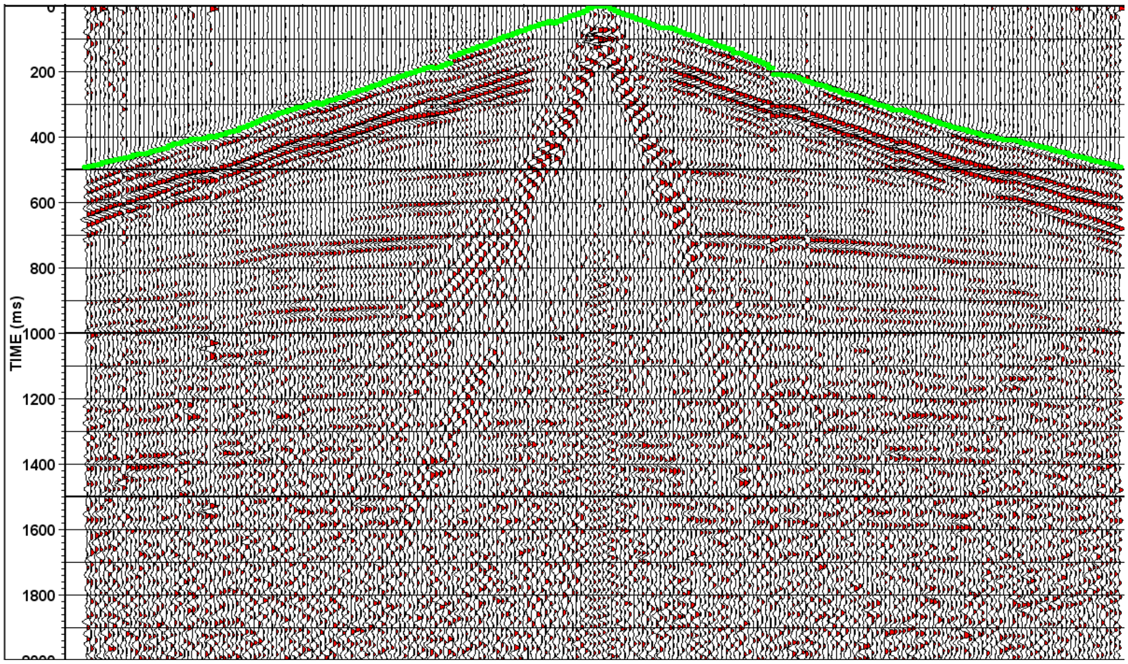

Figure 3-8. Example of shot record (vertical component) from Line 101 with first-break pick times identified. AGC with 500 ms window and band pass filter of 10-15-45-50 hz were applied.

The uncertainty in the calculation of velocities is linked to the uncertainty in the measure of minus-times (T_i^-) and of first breaks times. Assuming that each of these times is normally distributed about its true value with width parameter, σ, therefore the deviations are also normally distributed and a good estimate of the uncertainty can be obtained with the following expression (Taylor, 1982):

$$\sigma^2 = \frac{1}{N-2} \sum (Y_i - A - Bx_i)^2 \tag{3.4}$$

Where, Yi are the first break times or the minus-times to calculate V_1 or V_2, respectively. A and B are approximated by the constants obtained from the fit line (intercept and slope, respectively) and x_i is the distance. The denominator originally would be N, but in this case is N-2 to reflect the degrees of freedom. We have N measurements but before estimating σ, A and B had to be computed, this leaves N-2 degrees of freedom. The number of degrees of freedom is the number of independent measurements minus the number of parameters computed from these measurements.

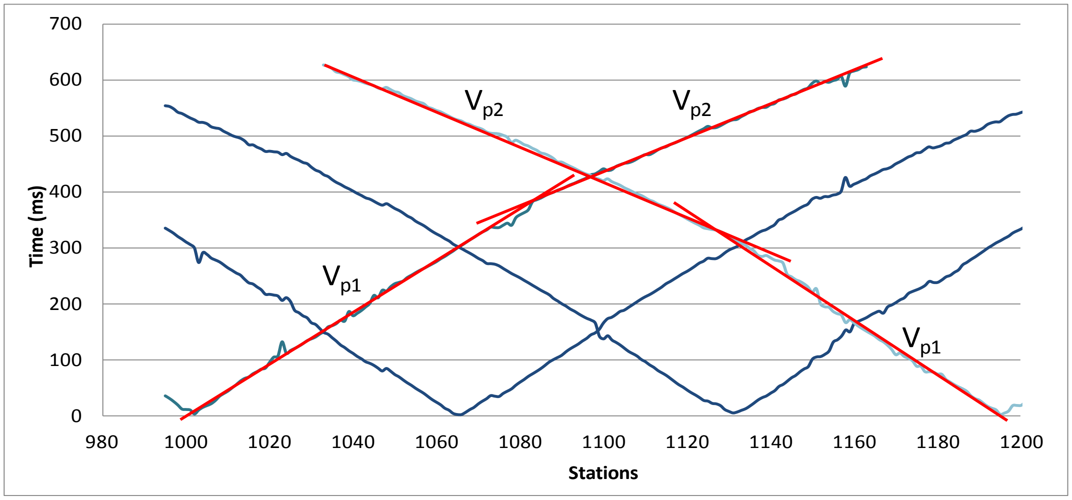

Figure 3-9. P-wave first-break times for four example shots along Line 101.

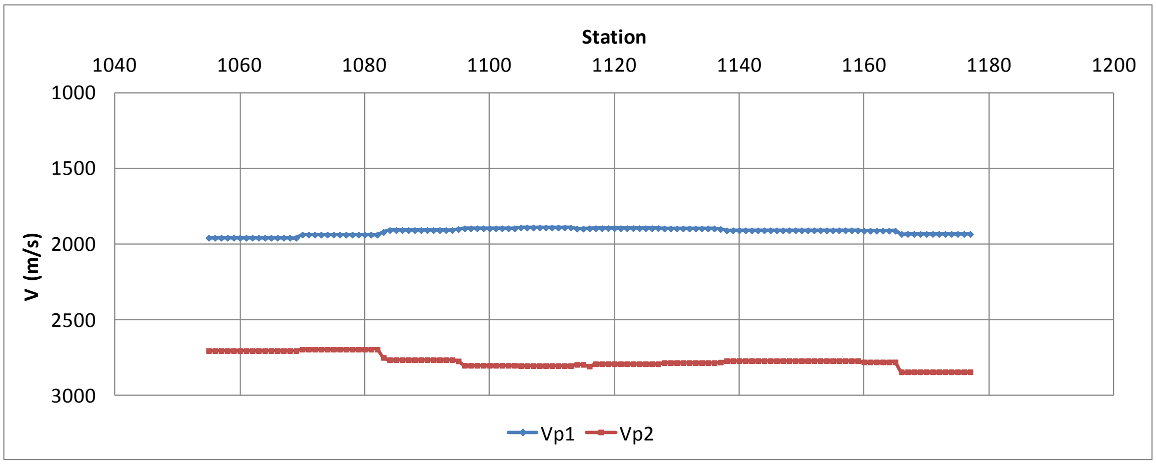

Figure 3-10. P-wave velocity profile for layer one (V_{p1}) and layer two (V_{p2}) for Line 101.

The regression coefficients for the fitted lines to calculate V_{p1} ranged from 0.985 to 0.999 and the uncertainty in the measurements of time for these two fitted lines are 2.65 ms and 9.73 ms; this corresponds to 1.62% and 4.2% of the mean value, respectively. For the calculation of V_{p2}, the regression coefficients for the fitted lines ranged from 0.9975 to 0.9998 and the uncertainty in the measurements of minus-times (T^-) for these two datasets are 0.75 ms and 3.63 ms; this corresponds to 0.12% and 0.55% of the mean value, respectively.

The velocities and the plus times were used to calculate the depth to the refractor (second layer) below each receiver. The result is shown in Figure 3-11. The average depth to this refractor was found to be around 170 m.

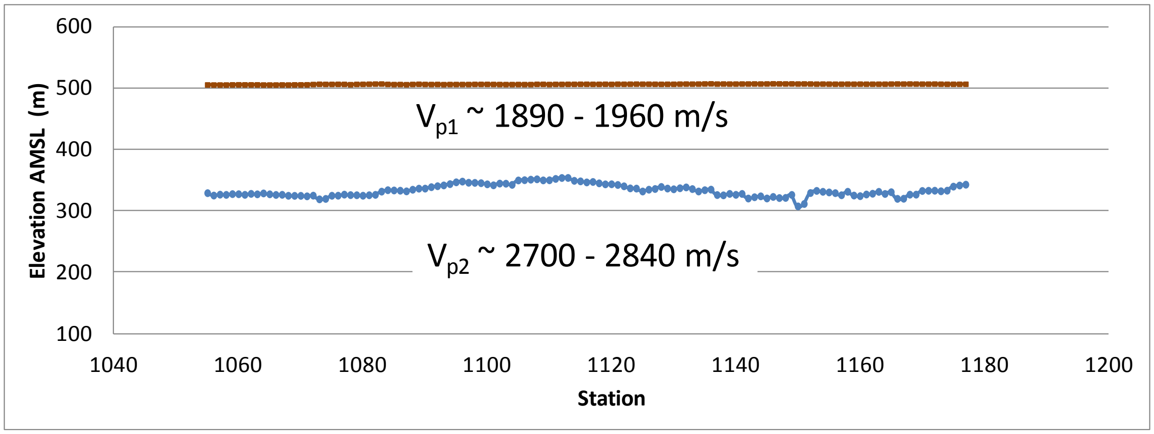

Figure 3-11. Depth profile obtained from P-wave data along Line 101.

Error propagation was evaluated for the calculation of depth to the refractor. Depth is a function of the plus-times (T^+) and the velocity of the first (V_1) and second (V_2) layers. Assuming that these parameters are random and independent, the uncertainty of depth (δh_1) calculation can be estimated with the following expression (Taylor, 1989):

$$\delta h_1 = \sqrt{\left(\frac{\partial h_1}{\partial T^+}\delta T^+\right)^2 + \left(\frac{\partial h_1}{\partial V_1}\delta V_1\right)^2 + \left(\frac{\partial h_1}{\partial V_2}\delta V_2\right)^2} \tag{3.5}$$

The values for the uncertainties of the parameters δT^+, δV_1 and δV_2 were assumed to be 5 ms, 100 m/s and 200 m/s, respectively. The result for depth uncertainty, δh_1, varied between 11 m and 16 m.

3.3.2 Analysis and results for Line 103, SH-wave mode (90 shots)

Figure 3-12 shows an example of a shot record (transverse component) from Line 103 with the first-break times; this is SH-wave data with fair quality for first arrival energy. Two sectors were more difficult to pick, at the receivers close to the shot and at the receivers near the crossover points. The quality in terms of reflection data is more irregular with only a few shots showing clear events. The example gather in Figure 3-12 shows good SH reflections between 500 ms and 2200 ms.

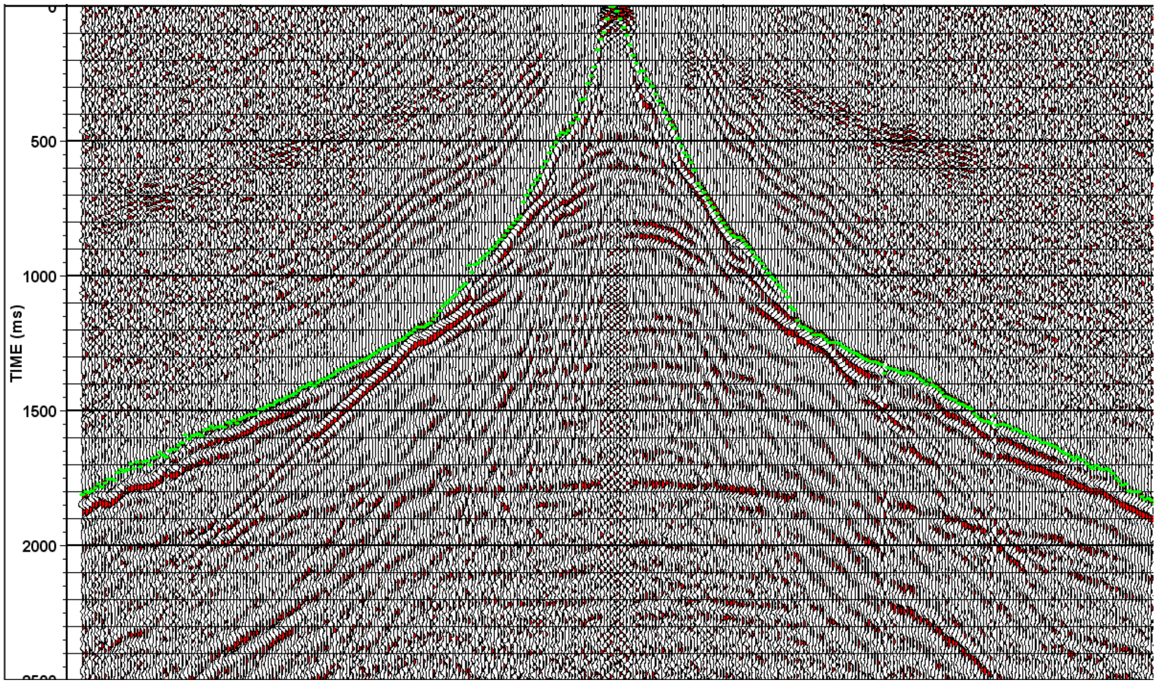

Figure 3-12. Example of shot record (transverse component) from Line 103 with first-break pick times identified. AGC with 500 ms window and band pass filter of 5-10-45-50 hz were applied.

The same methodology for the velocity-depth structure estimation was followed for the SH-data; picking first break times, exporting them to a spreadsheet and applying the plus-minus time analysis. Figure 3-13 shows first arrival times from three shots along the line and confirms the presence of three layers for this profile by considering a change of slope as a change of layer (a slope represents a particular velocity). The middle shot shows the presence of the three layers; the interpreted lines are offset to enable the actual picks to be visible. However during the analysis, it was found that the segment between stations 2250 and 2400 showed behaviour as if the shallowest layer was thinning, but east of station 2400, this layer again thickened. It was difficult to establish the plus-minus window here as the first breaks from the first refractor were fewer than along the remainder of the line. Figure 3-14 shows the velocity profile along this line and a decrease in the velocity of the second layer is noticeable between stations 2250 and 2400.

The regression coefficients for the fitted lines to calculate V_{s1} ranged from 0.9707 to 0.9989 and the uncertainty in the measurement of time for these two fitted lines are 4.92 ms and 28.9 ms; this corresponds to 1.4% and 8.3% of the mean value. For the calculation of V_{s2}, the regression coefficients for the fitted lines ranged from 0.9944 to 0.9998 and the uncertainty in the measurements of minus-times (T^-) for these two fitted lines are 3.07 ms and 19.76 ms; this corresponds to 0.22% and 1.48% of the mean value, respectively. For the calculation of V_{s3}, the regression coefficients for the fitted lines ranged from 0.9908 to 0.9996 and the uncertainty (in T_i^-) for these two fitted lines are 2.74 ms and 13.2 ms; this corresponds to 0.15% and 0.77% of the mean value, respectively.

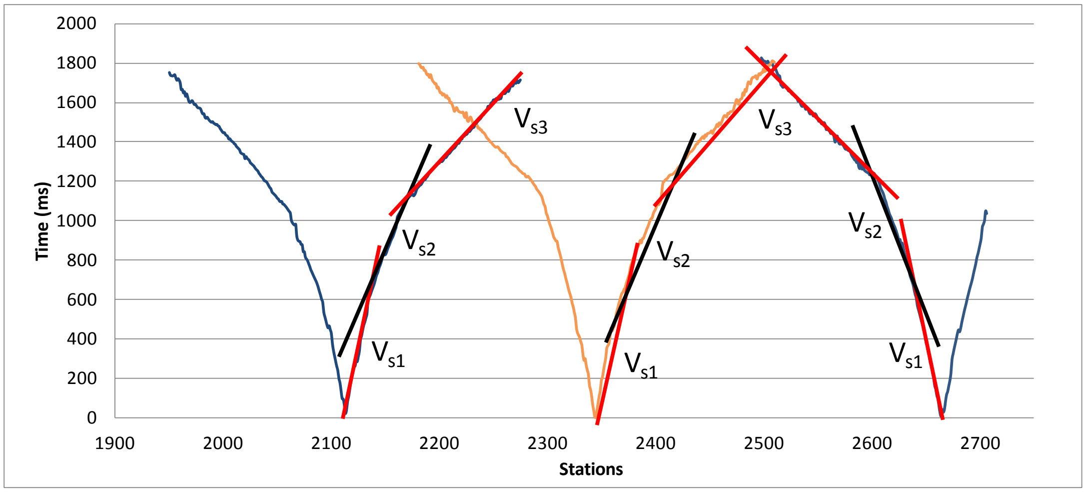

Figure 3-13. SH-wave first-break times for three example shots along Line 103.

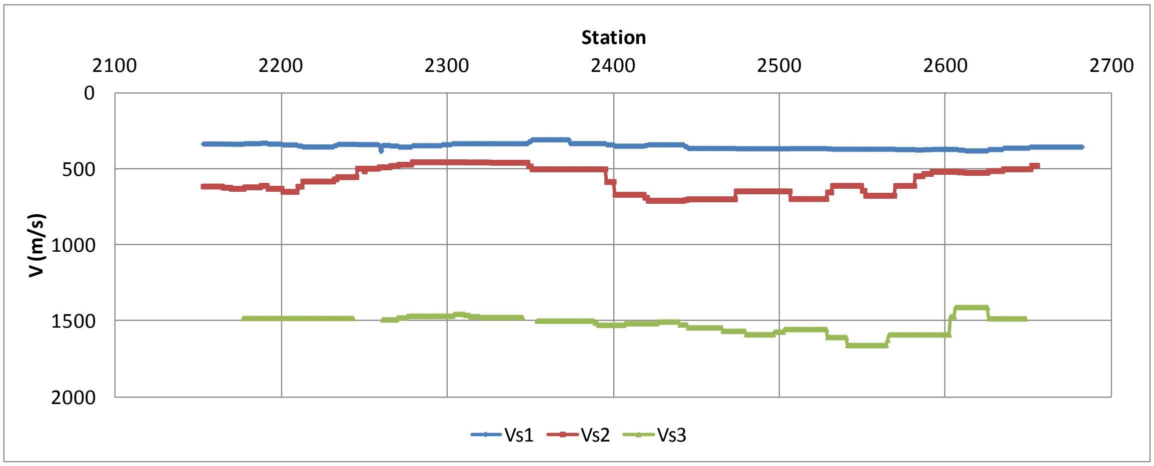

Figure 3-14. SH-wave velocity profile for layer one (V_{s1}), layer two (V_{s2}) and layer three (V_{s3}) along Line 103.

Figure 3-15 shows the depth profile along Line 103. The depth to the first refractor was found to be around 70 m and the depth to the second refractor ranged from 270 m to 320 m. Error propagation was evaluated for the calculation of the depth to the refractors. The uncertainty for the first refractor was calculated with equation 3.5. Two more terms had to be included to calculate the uncertainty of the depth to the second refractor (δh_2) to account for the error in the calculation of the depth to the first refractor, h_1, and the velocity of the third layer, V_{s3}. Equation 3.6 shows this modification. The parameters δT^+, δV_1, δV_2. δV_3, and δh_1 were assumed to be 5 ms, 100 m/s, 200 m/s, 200 m/s, and 10 m respectively. The uncertainty for the depth to the first refractor was found to vary from 6.6 m to 46 m and for the second refractor varied from 22 m to 57 m.

$$\delta h_2 = \sqrt{\left(\frac{\partial h_2}{\partial T^+}\delta T^+\right)^2 + \left(\frac{\partial h_2}{\partial V_1}\delta V_1\right)^2 + \left(\frac{\partial h_2}{\partial V_2}\delta V_2\right)^2 + \left(\frac{\partial h_2}{\partial V_3}\delta V_3\right)^2 + \left(\frac{\partial h_2}{\partial h_1}\delta h_1\right)^2} \qquad (3.6)$$

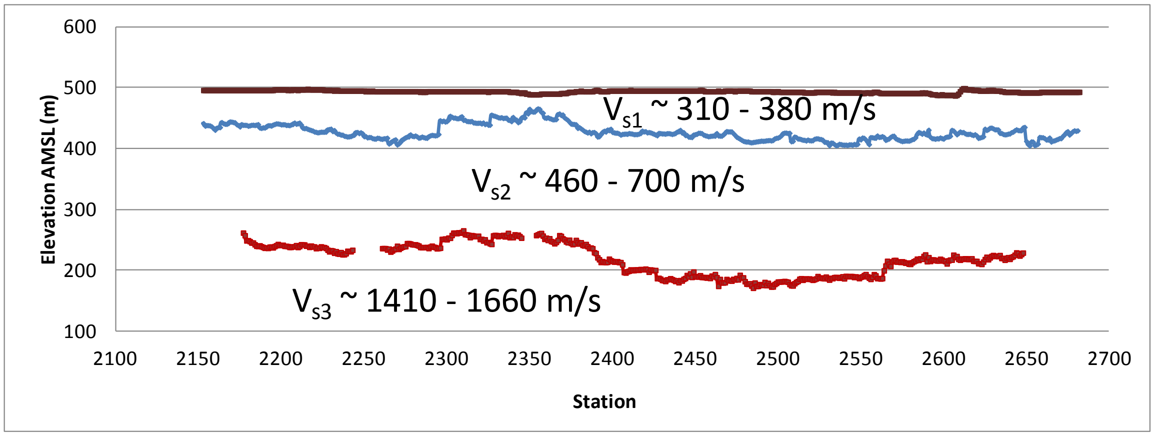

Figure 3-15. Depth profile obtained from SH-wave data along Line 103.

3.3.3 Analysis and results for Line 104, P & SH wave mode (220 shots)

Examples of shot records from this line were shown earlier in this chapter (Figure 3-7). From the analysis of the SH first-break times, three layers were detected to the west end of the line and two layers to the east end of the line (Figure 3-16). From the P-wave data only two layers were detected for the entire line (Figure 3-17). V_i (i= 1, 2, or 3) indicates the velocity for first, second and third layer, respectively. In these figures, the interpreted line segments for the middle shot are displaced from the actual so the real data can be appreciated.

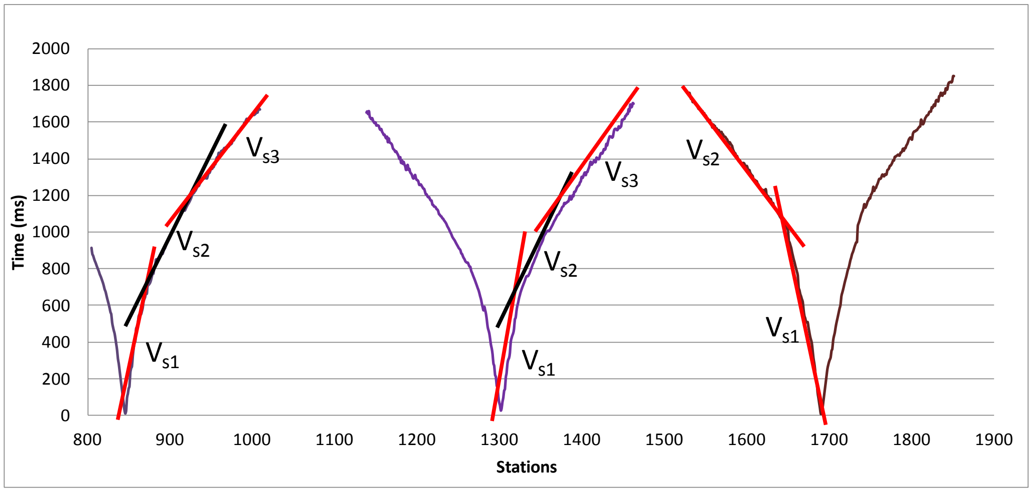

Figure 3-16. SH first-break times for three example shots from Line 104. Three layers were detected at the west end of the line (left); two layers were detected at the east end of the line (right).

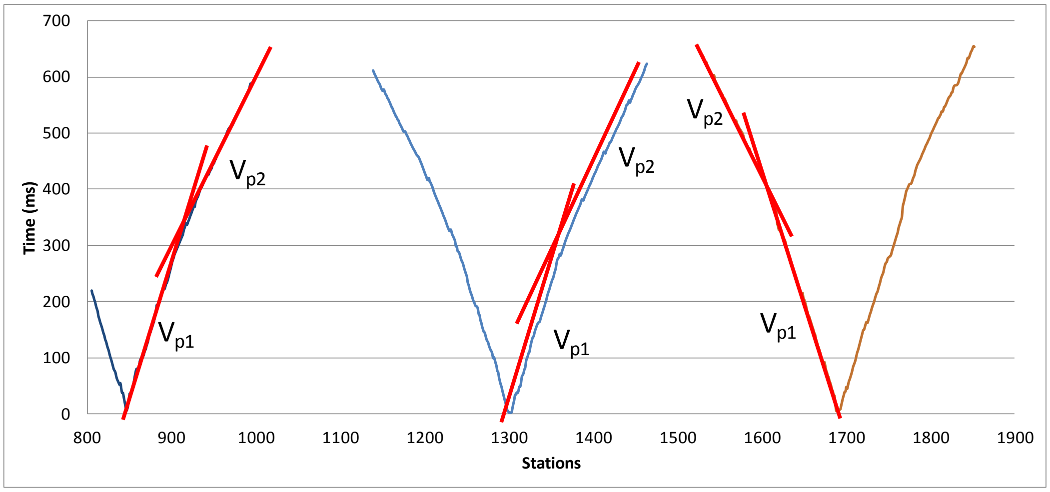

Figure 3-17. P-wave first-break times for the same shots as shown in Figure 3-16. Two layers were detected along the entire profile.

3.3.3.1 P-wave data analysis

For the P-wave data, the plus-minus time analysis was performed using the Excel spreadsheet as the lack of long offsets made difficult to determine systematic plus-minus windows to enable the method to be applied automatically. During the analysis I had to be very careful to choose the correct pairs of shots in order to perform the computations reliably. V_{p1} was calculated directly from the first breaks of the near offsets; V_{p2} was calculated through the minus-time method (Figure 3-18). The plus times were then used to calculate the depth of the weathering layer (Figure 3-19), where a channel can be seen toward the east end of the line.

The average velocity was found to be approximately 1920 m/s for the first layer and ranged from 2750 m/s to 2950 m/s for the second layer. The regression coefficient for the fitted lines to estimate V_{p1} ranged from 0.9935 to 0.9995 and the uncertainty in the measurements of the first-break times for these fitted lines are 2.48 ms and 7.14 ms; this corresponds to 1.2% and 5.0% of the mean value, respectively. The regression coefficient for the fitted lines used in the minus-time analysis to find V_{p2} ranged from 0.9956 to 0.9998 and the uncertainty in the measurement of these minus-times are 1.38 ms and 7.52 ms; this corresponds to 0.19% and 0.86% of the mean value, respectively.

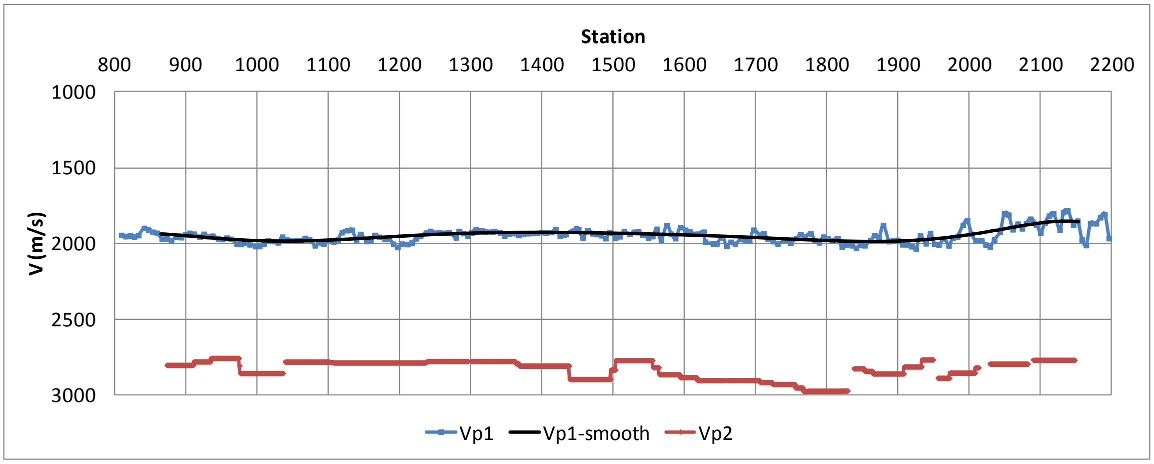

Figure 3-18. P-wave velocity profile for layer 1 (V_{p1}) and layer two (V_{p2}) along Line 104.

The velocities shown in Figure 3-18 were used to calculate the depth to the refractor for a two layer case (equation 1.10). The depth profile is shown in Figure 3-19, where a shallow channel can be seen between stations 1600 and 1950. This channel was expected from the electromagnetic survey acquired in the same area; in this case, the line crosses perpendicular to the channel (Figure 3-1). Again, error propagation was analysed for the calculation of depth to the refractor using equation 3.5. It was found an uncertainty range from 16 m to 21 m.

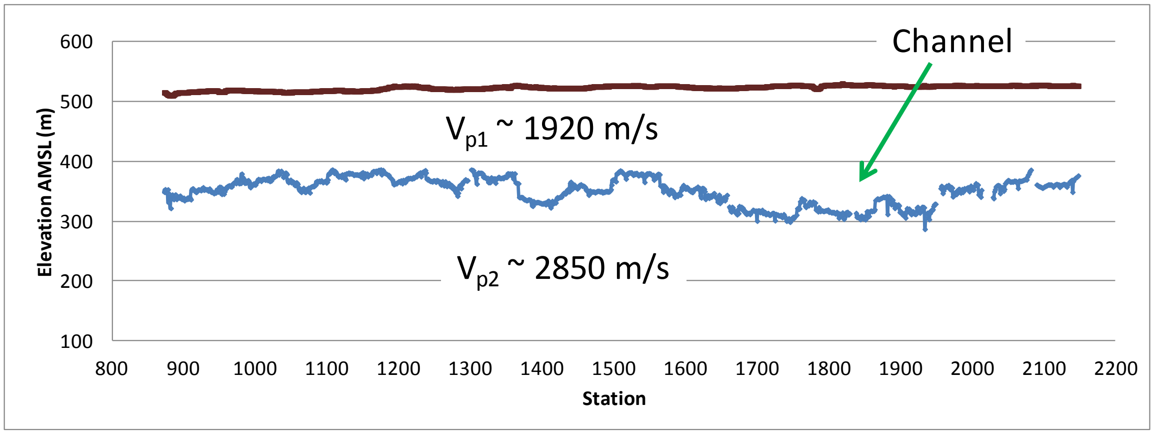

Figure 3-19. Depth profile obtained from P-wave data along Line 104.

3.3.3.2 SH-wave data analysis

The plus-minus time analysis was used to obtain the velocities and depths. For the SH-wave data, this process was carried out using the spreadsheet as well as through a program for automatic analysis. Plus and minus times were calculated using equations 1.8 and 1.11. V_{s1} was calculated directly from the first breaks of the first layer and V_{s2} and V_{s3} were obtained through minus time analysis (Figure 3-7). This method requires pair of shots to make the analysis and the definition of the analysis window between the crossover points (every 10th or 20th shot); these shots were chosen so that the entire profile had single-fold coverage and there is no redundancy of depth or velocity results at each receiver.

The regression coefficients of the fitted lines used for the calculation of V_{s1} ranged from 0.951 to 0.9978 and the uncertainty in the measurement of time are 6.43 ms and 27.72 ms; this corresponds to 2.5% and 6.7% of the mean value, respectively. The regression coefficients obtained for V_{s2} ranged from 0.9751 to 0.9986 and the uncertainty in the measurement of minus-times are 7.10 ms and 35.34 ms; this corresponds to 0.5% and 2.4% of the mean value, respectively. For the calculation of V_{s3}, the regression coefficients of the fitted lines ranged from 0.9923 to 0.999 and the uncertainty in the measurement of time are 11.4 ms and 12.8 ms; this corresponds to 0.7% and 0.8% of the mean value, respectively.

Depths were calculated using equations 1.10 or 1.15 for two or three layer cases, respectively. The velocities and depth profiles for this line are shown in Figure 3-20 and Figure 3-21, respectively. Error propagation was analysed for the calculation of depth to the refractors using equation 3.5 and 3.6. It was found an uncertainty range from 5 m to 22 m for the depth to the first refractor and 19 m to 70 m for the depth to the second refractor.

As previously mentioned, three layers were detected from the first break times near the west end of the line. Around shot 310 (stn 1367) the second layer decreased in thickness so the analysis window, which is determined between the crossover points, was too small and this prevented the second shot being located within the refractor data being analysed. Consequently the second refractor was not clearly identified in this region. To the east of station 1600 only two layers were interpreted (one refractor).

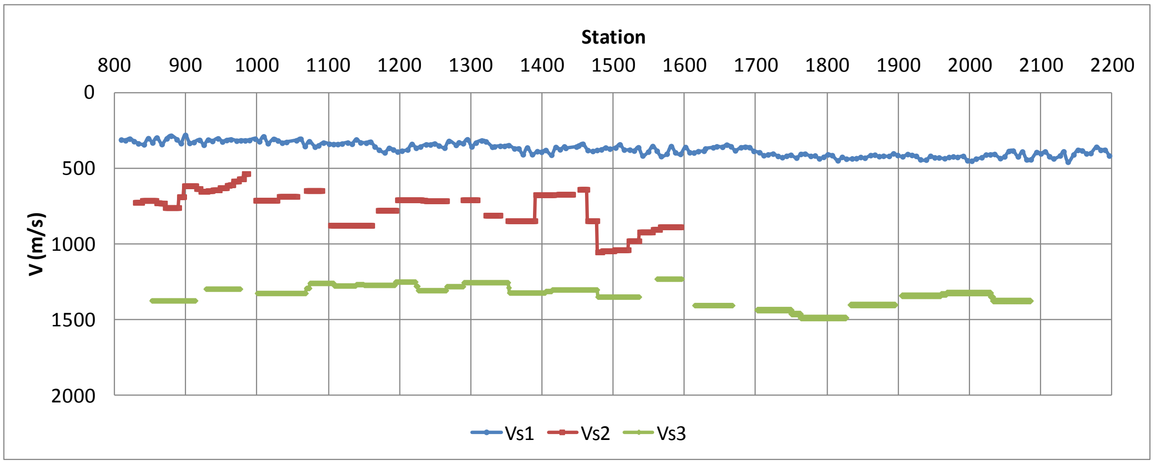

Figure 3-20. Velocity profile obtained by manually applying the plus-minus analysis method for SH-wave data from Line 104.

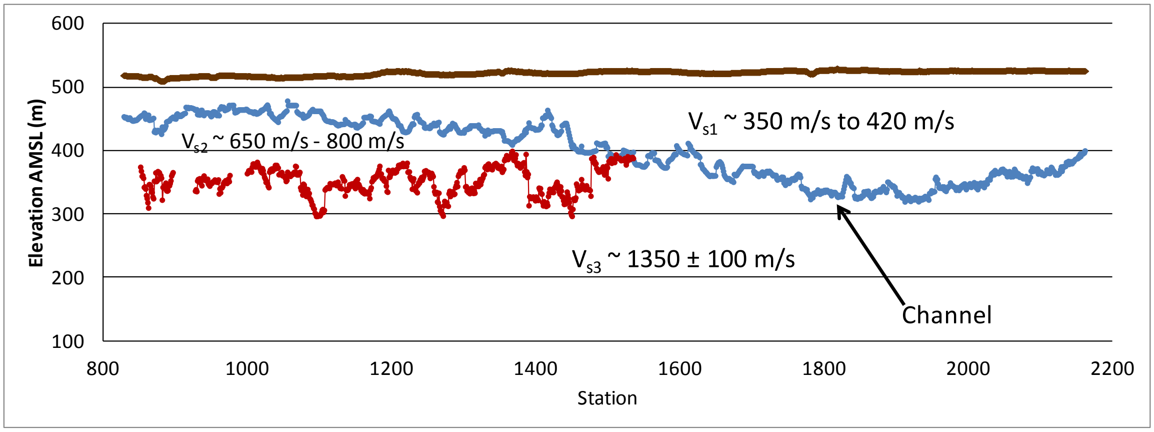

Figure 3-21. Depth profile obtained by manually applying the plus-minus analysis method for SH-wave data from Line 104.

The plus-minus time analysis was also undertaken using a program that requires the first break picks as an input and generates velocity and depth for the entire profile using all appropriate shots for each plus-minus window. Other input parameters for this program are the minimum window offset, minimum shot-to-shot offset (stations) and maximum shot-to-shot offset (stations). These values specify the analysis window for each pair of shots. Every shot is used with shots from the segment between the minimum shot-to-shot offset and maximum shot-to-shot offset. The minimum window offset identifies the lower limit of the window width for plus-time and minus-time calculations. The minimum shot-to-shot distance needs to be at least twice the minimum offset window (Figure 3-22).

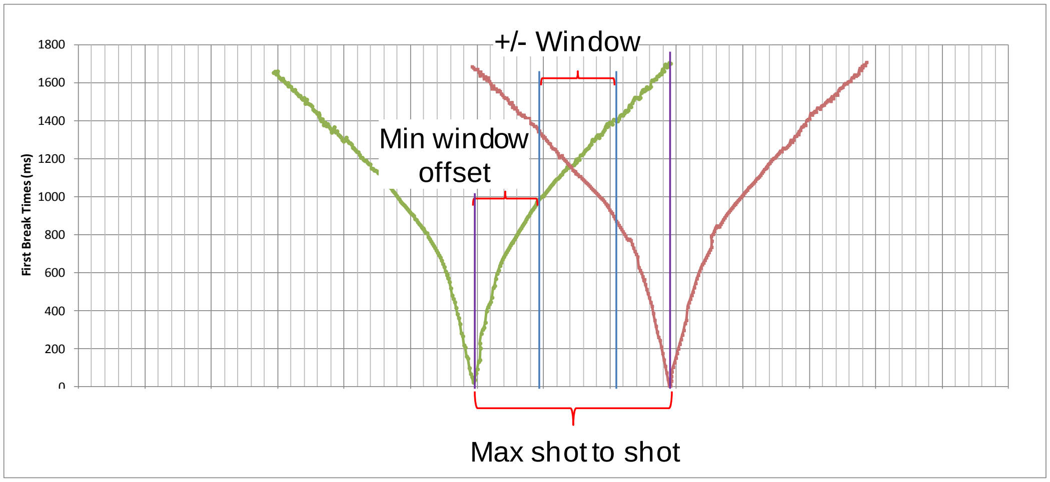

Figure 3-22. Input parameters for the plus-minus analysis code.

Velocities output with this program are shown in Figure 3-23. Figure 3-23a shows the raw results and, Figure 3-23b shows the velocity profile smoothed through a polynomial function of order 10. Figure 3-23c is a final composite of velocities for the profile. From Figure 3-23a and Figure 3-23b, it can be seen that V_{s1} and V_{s2} tend to the same value east of station 1500, suggesting that this layer is disappearing in the area marked as transition zone (Figure 3-23b). This was confirmed by the manual calculation where from shot 310 (stn 1367) to shot 355 (stn 1659) it was not possible to apply the plus-minus time analysis due to insufficient sampling of the second layer (the thickness was decreasing).

For the deeper refractor, the velocity was obtained using two different analysis windows. The light green curve (V_{s3}') was the result of a wider window to better sample the deeper layer, but this window was also sampling the second layer near the west end of the line causing the decrease in velocity in this region (see note in Figure 3-23b). This figure shows the results with the optimum window found after several attempts. The velocity in the first layer ranges from 350 m/s to 420 m/s, for the second layer it ranges from 500 m/s to 680 m/s and for the third layer there is a lateral variation from 1400 m/s in the west to 1100 m/s in the east.

Figure 3-24 shows the standard deviation for the velocities shown in Figure 3-23. Figure 3-24a shows the standard deviation for the velocity of the second layer which in average is 63 m/s. Figure 3-24b shows the standard deviation for velocity of the deepest refractor to the west end of the line which in average is 106 m/s and Figure 3-24c shows the standard deviation for velocity of the deepest refractor to the east end of the line which in average is 173 m/s.

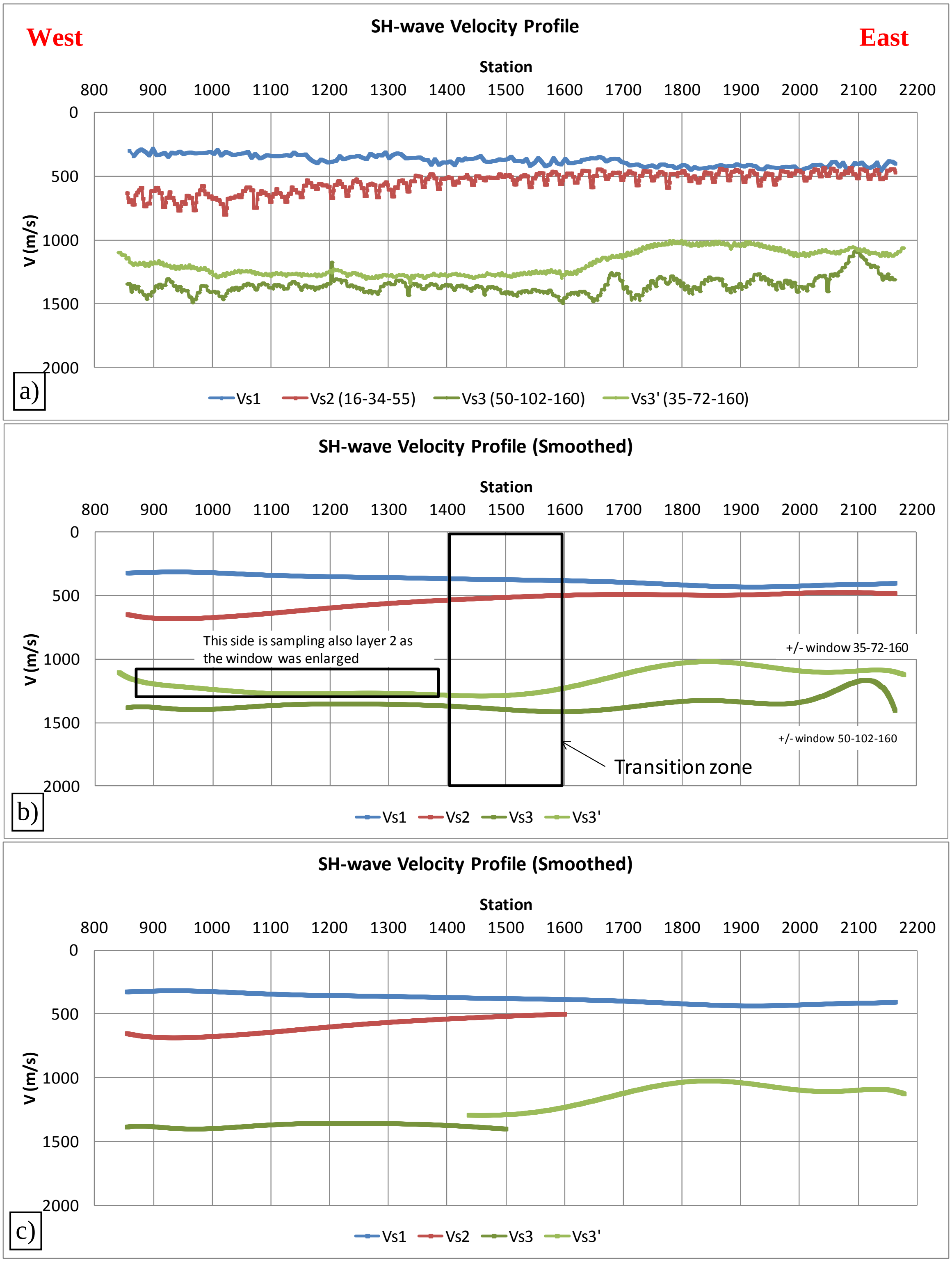

Figure 3-23. Velocities obtained with the plus-minus code for the SH-wave data from Line 104. a) raw velocities, b) smoothed velocities, c) composite velocities.

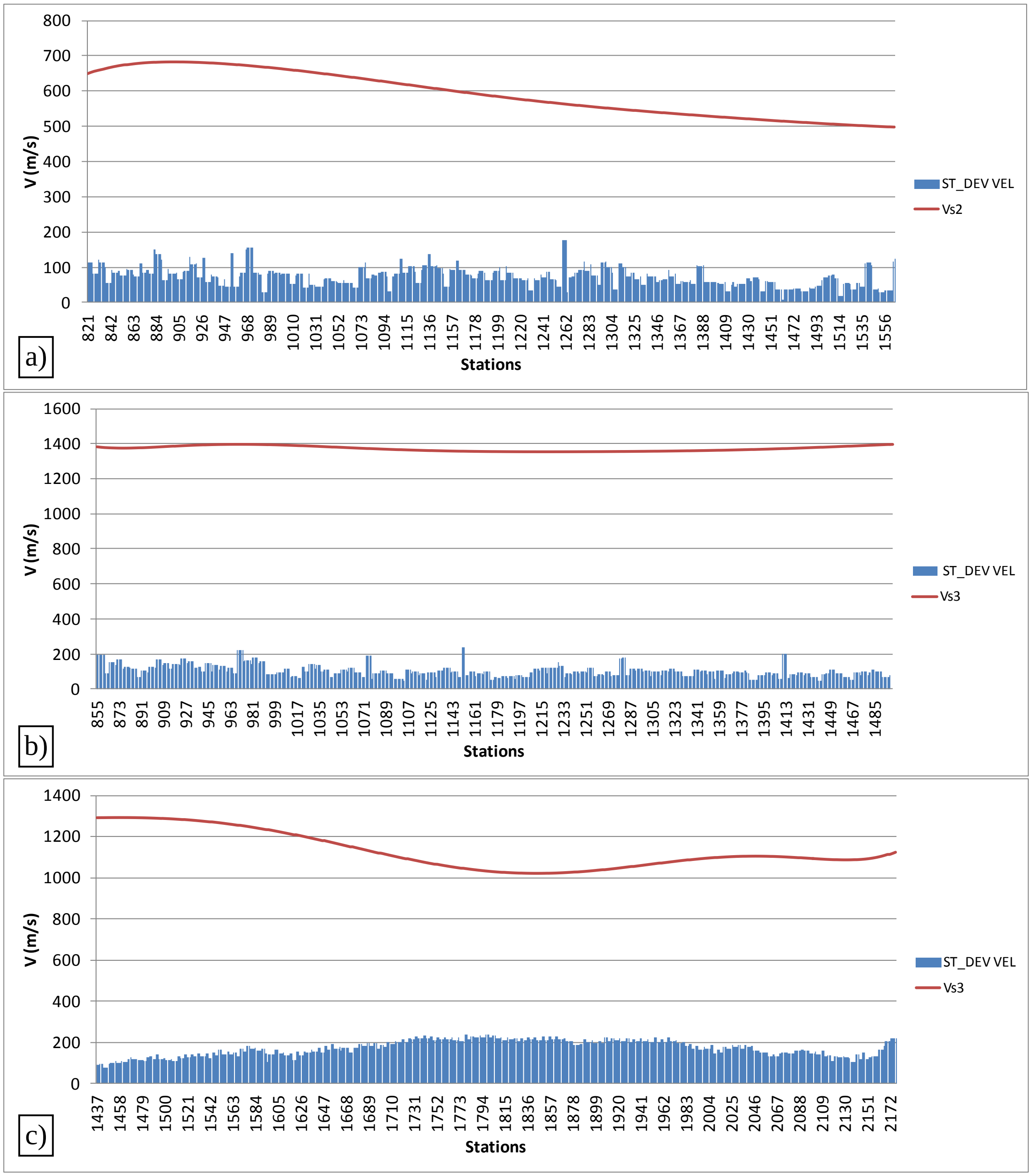

Figure 3-24 Velocity Standard deviation from software calculation. a) standard deviation for the velocity of the second layer, b) standard deviation for the velocity of the deepest refractor to the west end of the line and c) standard deviation for the velocity of the deepest refractor to the east end of the line.

The depth profile, obtained using the velocities of Figure 3-23c, is shown in Figure 3-25. It was difficult to define the refractor boundaries explicitly between station 1400 and 1600, since in this region it was assumed that layer 2 was thinning. This depth profile also confirms the presence of a channel in the area, as previously described from the electromagnetic survey (EM acquired by Nexen) and with the P-wave data. The lower velocity (V_{s3}') toward the east end of the profile is thought to be influenced by the presence of the channel. Error propagation was analysed for the calculation of depth to the refractors using equations 3.5 and 3.6. It was found an uncertainty range from 7 m to 24 m for the depth to the first refractor and 22 m to 62 m for the depth to the second refractor.

There is good agreement between the model generated manually and the model generated with the software. The benefit of the latter is that the results are generated faster; the benefit of doing the process manually is that changes in velocity or depth (changes in the near-surface) can be detected as the optimum pairs of shots are assessed along the line. The depth profile generated with the manual method presents high scatter due to low fold for the calculations at each receiver. The automatic method produces a smoother refractor due to higher number of calculations at each receiver; many pairs of shots are used in the process hence the final result is an average that produces a more regular depth profile.

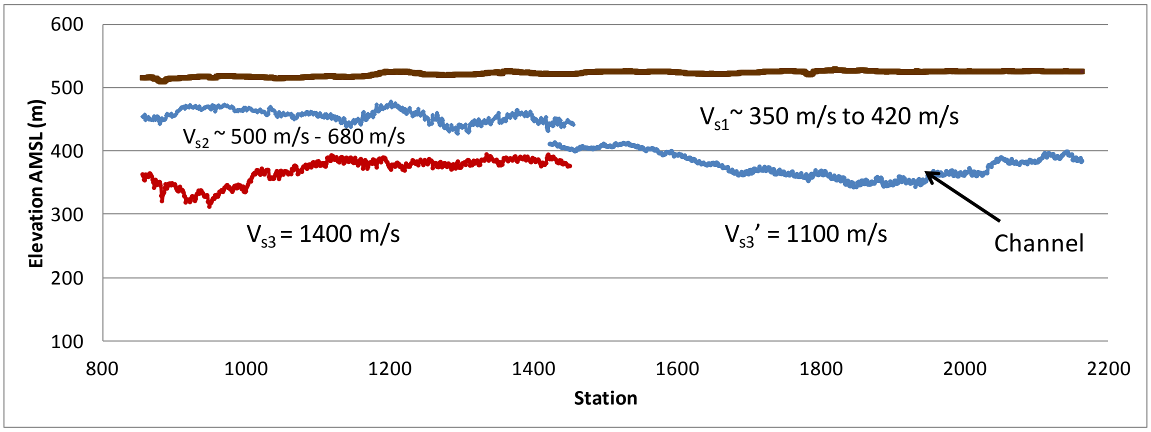

Figure 3-25. Depth profile obtained from SH-wave data along Line 104.

Line 101 runs parallel and adjacent to the main channel detected in the area through the electromagnetic survey (Figure 3-1). The channel has more influence towards both ends of the line, confirmed by the slightly deeper refractor in these ends of line (Figure 3-11). Line 103 runs almost parallel to the main channel in the area. The resistivity map shows higher values to the east end of the line and this is reflected in the depth profile (Figure 3-15) where the refractor gets deeper towards the east end of the line. The east end of Line 104 crosses a secondary channel shown in the resistivity map. The values of resistivity in this secondary channel are lower than the values at the main channel, suggesting shallower depth which is confirmed by comparing the depth profiles of Lines 103 and 104 (Figure 3-15 and Figure 3-21). The deepest part in Line 104 is around 220 m while the deepest part in Line 103 is around 320 m.

In terms of velocity, the SH-wave data of Line 104 shows that the second layer thins out, leaving only two layers to the east end of the line. Lines 101 and 103 do not present noticeable variations in velocity. The lines are located fairly apart and they yield similar velocities between them.

3.3.4 Generalized linear inversion (GLI) method

A comparison of the plus-minus results with the generalized linear inversion method (Hampson and Russell, 1984) was made (GLI by Sensor Geophysical). In this method, three-layer models were assumed for both P-wave data and SH-wave data (Figure 3-26 and Figure 3-27). For the P-wave data, a velocity of 1000 m/s was assumed for the first layer, and an average velocity of 1950 m/s for the second layer and an average velocity of 2900 m/s for the third layer were obtained. The depth for the first layer varies from 1 m to 10 m and for the second varies from 140 m to 210 m. For the SH-wave data, a velocity of 350 m/s was assumed for the first layer, a velocity from 500 to 900 m/s was determined for the second layer and an average of 1400 m/s was obtained for the third layer. The depth for the first layer was found to vary from 50 m to 90 m and for the second layer from 180 m to 210 m.

Comparing Figure 3-26 and Figure 3-27 with the results from the plus-minus analysis method, they have good agreement in terms of velocities (Table 3-2). However, the depth profile shows some differences. The depth of the basal refractor is similar in both methods but there are some differences in the general model. The P-wave data assumed 3 layers but the first layer is very thin and disappears to the east end on the line; this is close to the plus-minus method where only two layers were considered. For the SH model, three layers were interpreted for the GLI method; the deeper refractor is similar in both methods. The difference is that for the GLI method, the three layers are present for the entire profile whereas for the plus-minus method, there are three layers to the west and only two layers to the east. The GLI method forces three layers to be continuous along the profile whereas the plus-minus method gives the flexibility of changing analysis windows depending on data changes and allows more significant lateral changes in the velocity-depth model.

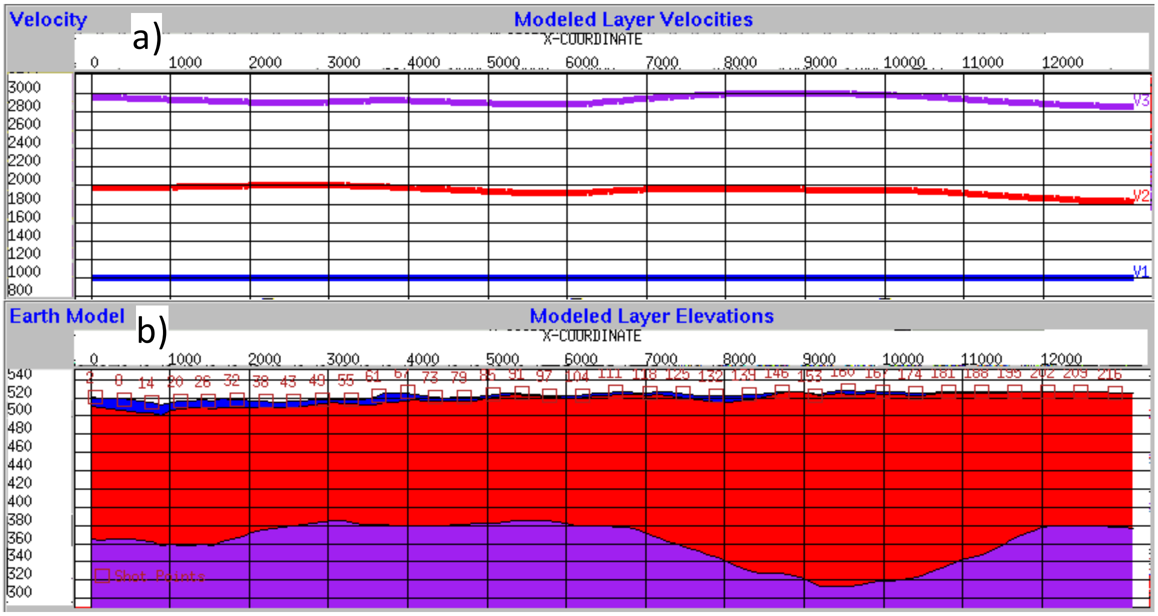

Figure 3-26. Results from the GLI method. a) P-wave velocity profile. b) P-wave depth profile.

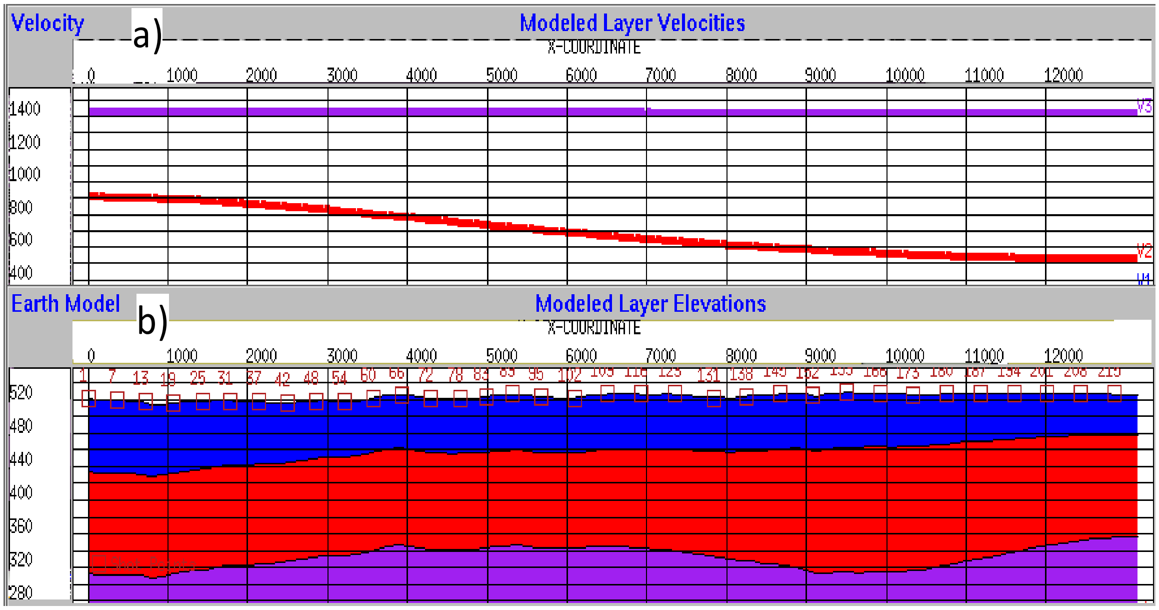

Figure 3-27. Results from the GLI method. a) SH-wave velocity profile, b) SH-wave depth profile.

Table 3-2. Comparison between GLI and plus-minus analysis results

	P-WAVE			
	Plus-minus analysis		GLI	
	Depth (m)	Velocity (m/s)	Depth (m)	Velocity (m/s)
Layer 1	140-220	1920 ± 65	1-10	1000
Layer 2		2850 ± 100	140-210	1950 ± 50
Layer 3	N/A	N/A		2900 ± 50

	SH-WAVE			
	Plus-minus analysis		GLI	
	Depth (m)	Velocity (m/s)	Depth (m)	Velocity (m/s)
Layer 1	40-200	375 ± 37	50-90	350
Layer 2	120-220	727 ± 85	180-210	500-900
Layer 3		1350 ± 100		1400

3.4 Statics corrections

As mentioned in section 1.3, static corrections are time shifts applied to the seismic data to correct for irregularities in the near-surface, low velocity material, different elevation of the stations, etc. The goal is to correct the reflection times as if they were recorded on a flat surface without the influence of the near-surface (Cox, 1999). The time corrections must be applied to data recorded at all surface locations to convert them to a set of times that would have been observed had the data been recorded on the datum surface with no weathering or low-velocity material present below this plane.

Time shifts assuming vertical rays were calculated for the P-wave and SH-wave near-surface models obtained in the previous analysis. Equations 1.17 and 1.18 were used for the two-layer case and three-layer case, respectively. The datum used for the three lines was 600 m and the velocity of the deepest refractor was used as the replacement velocity. Figure 3-28 through Figure 3-30 show the receiver datum static corrections for the three lines selected. The P-wave static corrections for Line 101 vary from 2 ms to 10 ms, and the average elevation in this line is 505 m; the shear wave static corrections for Line 103 vary from -180 ms to -250 ms and the average elevation in this line is 493 m. For Line 104, higher static corrections are calculated to the east due to a thicker first layer which has lower velocity. The datum static corrections vary from -150 ms to -250 ms for SH-wave data and about -15 ms to 15 ms for P-wave data. The elevation in this line ranges from 515 m to 526 m. The reflection time is reduced when the static correction is negative.

As a consequence of the low SH velocities, the magnitude of SH datum static corrections is typically much greater than for the corresponding P-wave values. Shear wave statics may be ten times or greater than the P-wave statics. This relationship is also reflected in the velocity ratio between compressional and shear data for the shallow layers. For this reason, S-wave statics are difficult to estimate with confidence (Tatham, 1991; Lawton, 1993).

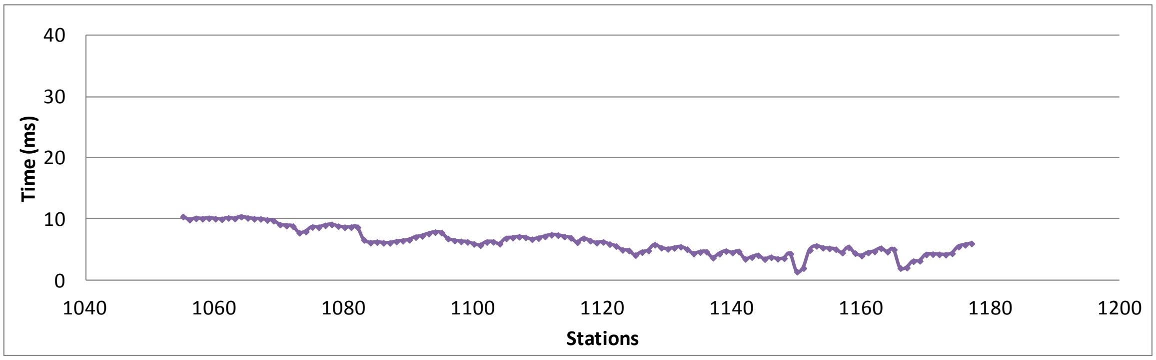

Figure 3-28. Datum receiver static corrections for P-wave data, Line 101.

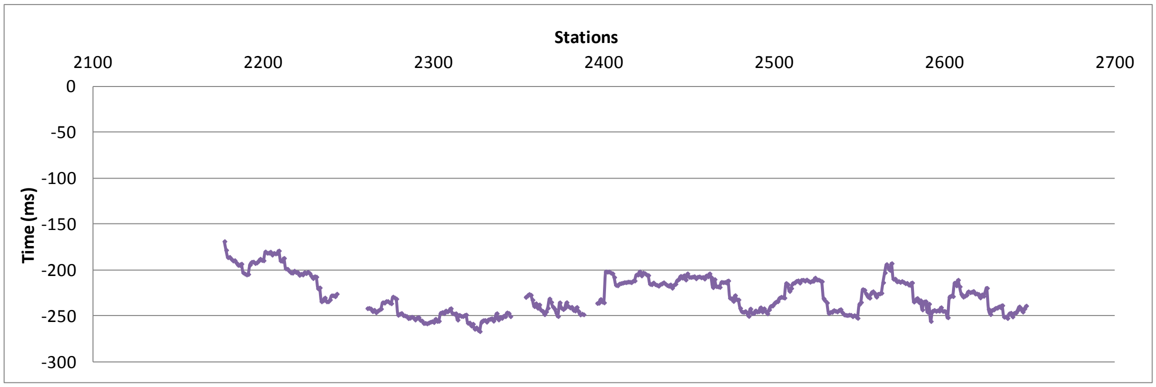

Figure 3-29. Datum receiver static corrections for SH-wave data, Line 103.

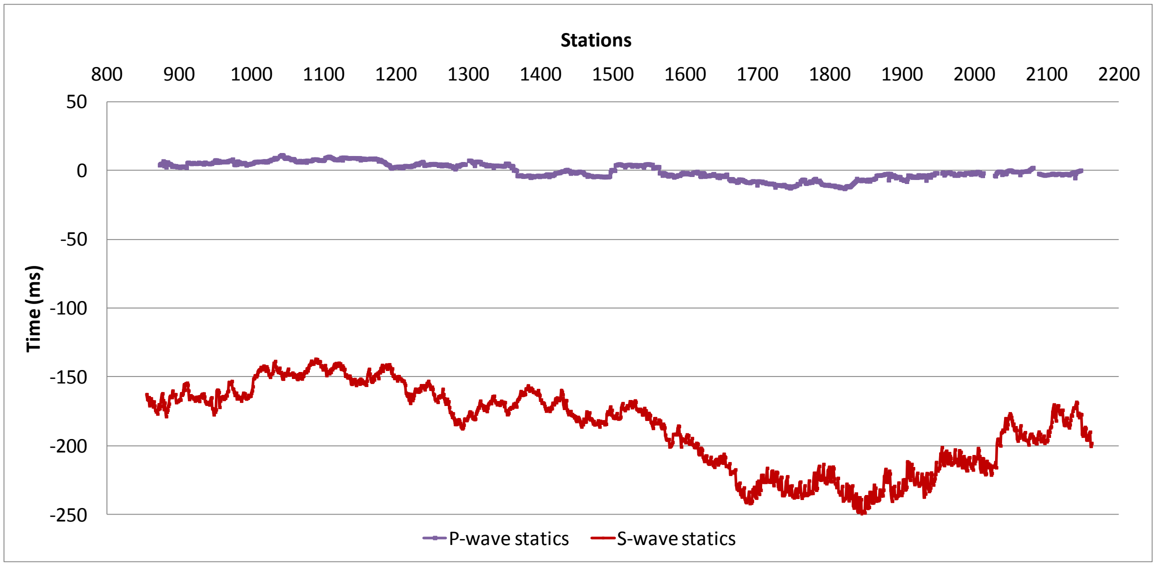

Figure 3-30. Datum receiver static corrections for P-wave data and SH-wave data, Line 104.

For Line 104, the shear static corrections have higher negative values around the channel due to the lower velocity and thicker layer in this area. The channel eroded the higher velocity layer present in the east end of the line and this is reflected in the higher values of statics where the channel is located. This lower velocity produces increased traveltime for reflections from deeper events in this region.

Notice that the statics for Line 103 are similar to those for the shear-wave data of Line 104 where the values of -200 ms to -250 ms are required in the channel area. The entire Line 103 is within the channel whereas Line 104 crosses the channel near the east end of the line where the values of statics coincide. The material in the channel is believed to be unconsolidated, so higher static corrections are reasonable. The P-wave statics are similar in both cases, Line 101 and Line 104; the influence of the channel is not as strong on P-wave data, which is why the P-wave static corrections do not vary as much as with the SH-wave data.

Lines 101 and 103 run parallel to the channel and this is the reason why the static corrections are more uniform compared to the corrections for Line 104 which is perpendicular to the secondary channel; here the influence of the channel is more evident.

Sensor Geophysical also provided their datum static correction results for Line 104 which can be seen in Figure 3-31. The trend of these curves is similar to the statics calculated in this study (compare to Figure 3-30), but the values are quite different for the S-wave statics. The shear wave statics from Sensor are 100 ms (average) smaller than the statics from this study. One difference on the calculation is the replacement velocity. Sensor used 1200 m/s for the S-waves and 2200 m/s for the P-waves. In this study, 1350 m/s for S-waves and 2850 m/s for P-waves were used. There was an 80 ms shift applied by Sensor to both P-wave and S-wave statics that was removed in Figure 3-31.

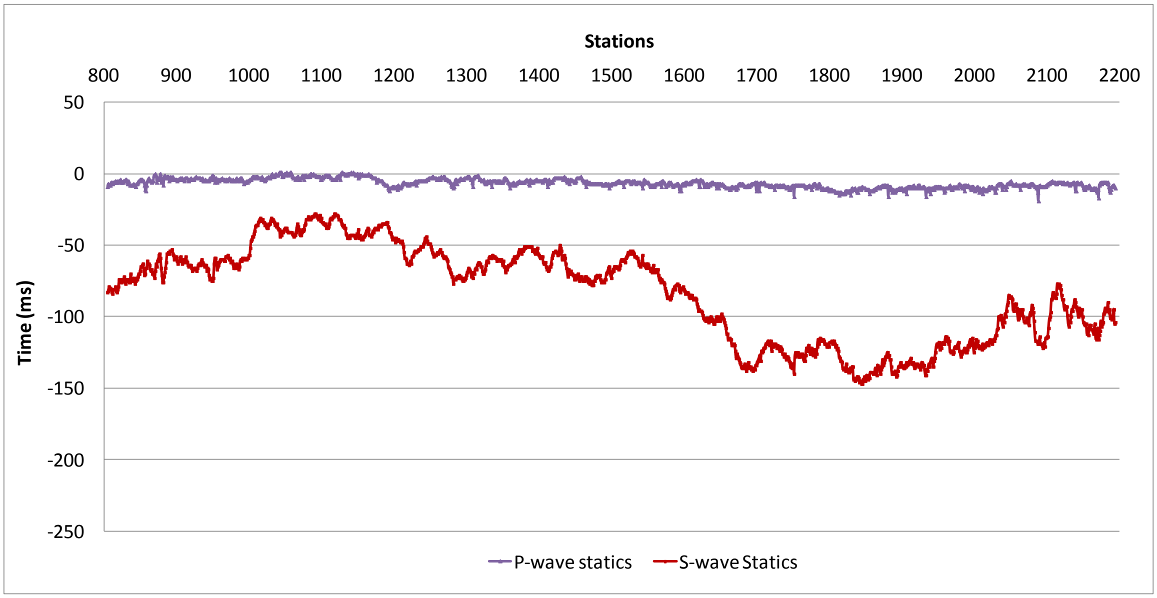

Figure 3-31. GLI result for datum receiver static corrections. Provided by Sensor Geophysical.

3.5 Summary of this chapter

This chapter showed the results of the refraction analysis method and the receiver static corrections. Accurate depth and velocities were obtained providing a detailed description of the near-surface structure using the plus-minus time analysis method. Three lines were analyzed from a refraction survey acquired in the study area. The first segment comprised 43 shots with only a P-wave source (Line 101), the second included 90 shots with only an S-wave source (Line 103) and the third 220 shots with both P- and S-wave sources (Line 104). From the model obtained, static corrections, which are needed for processing the reflection seismic data, were calculated. A comparison with the generalized linear inversion (GLI) was also presented in this chapter.

Chapter Four: V_P/V_S ANALYSIS

4.1 Introduction

The combination of S-wave and P-wave information helps in identifying changes in seismic amplitude due to lithology, pore fluid type and pore pressure (Avseth et al., 2005). Shear data assist in differentiating between changes in pressure or in saturation in 4D seismic data; these data has proved to produce better images of sediments with gas clouds where P-wave data failed. The property of shear splitting helps for anisotropy analysis and to describe reservoir fractures (Stewart et al., 2003).

The relationship of P-wave to S-wave velocity is very important to interpreting lithologic information from the formations of interest in the study area. One way to obtain this ratio is from compressional and shear sonic well logs. Another way is from interval time measurements of reflection events in P-wave and S-wave seismic sections. After interpreting the same horizons in both seismic sections, the velocity ratio can be estimated from an expression that relates Vp/Vs to interval times. Identifying identical reflection horizons will generate valid Vp/Vs. This chapter will describe both methods to find Vp/Vs values in order to compare the results and validate the interpretation.

The structure of this chapter will first show the well log available in the area of study, after that Vp/Vs for the near-surface, obtained from the log, will be compared to those values calculated from the refraction analysis result explained in chapter 3. Finally, Vp/Vs will be obtained through interval times from interpretation and again, these values will be compared to Vp/Vs values from the well log.

4.2 P-wave and S-wave information from well logs

Very important information is available from a well in the survey area, with a complete set of well log data taken over the entire length of the wellbore, i.e. from 40 m to 2054 m. The compressional sonic log and the shear sonic log were converted to compressional and shear velocities. Figure 4-1 shows a detailed view of logs, which from left to right the displayed curves are: S-wave velocity (green), P-wave velocity (magenta), density (red), Vp/Vs (blue) and Gamma Ray (brown).

Some important tops are shown in Figure 4-1 including the Bucking Horse (BH) Formation, Spirit River (SR) Formation, Banff Formation, Exshaw Formation, Tetcho Formation, Jean Marie (JM) Formation, Muskwa Formation and Otter Park Formation (OP). Marked increase in velocity can be observed at Exshaw and Tetcho Formations with Vp = 5550 m/s, Vs = 2700 m/s and Jean Marie Formation with Vp = 5250 m/s, Vs = 2550 m/s. From the log, the value of density for Exshaw and Tetcho is 2700 kg/m^{3}and for Jean Marie is 2550 kg/m^3; values are uniform for these formations unlike the Banff and Fort Simpson Formations which exhibit high frequency variations in density. The high values in velocity coincide with low values in Gamma Ray. These formations are mainly carboniferous shales and this is confirmed by the Vp/Vs of around 2.2 obtained from the log. The Muskwa Formation has a velocity of 3750 m/s and density of 2475 kg/m^3 in this log with high Gamma Ray reading; this formation is known to be highly radioactive - bituminous shale. Otter Park and Evie Formations have higher velocity than the overlying Fort Simpson with a bigger increase in Vs than in Vp, resulting in lower Vp/Vs values. The Gamma Ray is low in the Otter Park member that is composed by organic lean argillaceous carbonates. The general behaviour of the Vp/Vs curve is very uniform without extreme highs or lows except for the values in the near-surface (shallowest 170 m) where it reaches values up to 5.0. Vp/Vs of ~2.5 is obtained for the Buckinghorse and Spirit River formations and from this depth down to the top of Muskwa formation, an average Vp/Vs of 2.2 is observed; as mentioned earlier, the Otter Park and Evie Formations have a lower ratio of 1.7.

Examining the shallow section (0-400 m) that was the main interest in the previous chapter, we note that the velocities are comparable with those obtained from the plus-minus method (Figure 3.23). The S-wave velocity log shows a value of 500 m/s from 40 m to 170 m depth and an average of 1200 m/s from 170 m to 400 m depth. The P-wave velocity log shows ~2000 m/s from 40 m to 150 m depth, increasing to around 2500 m/s from 200 m to 400 m depth.

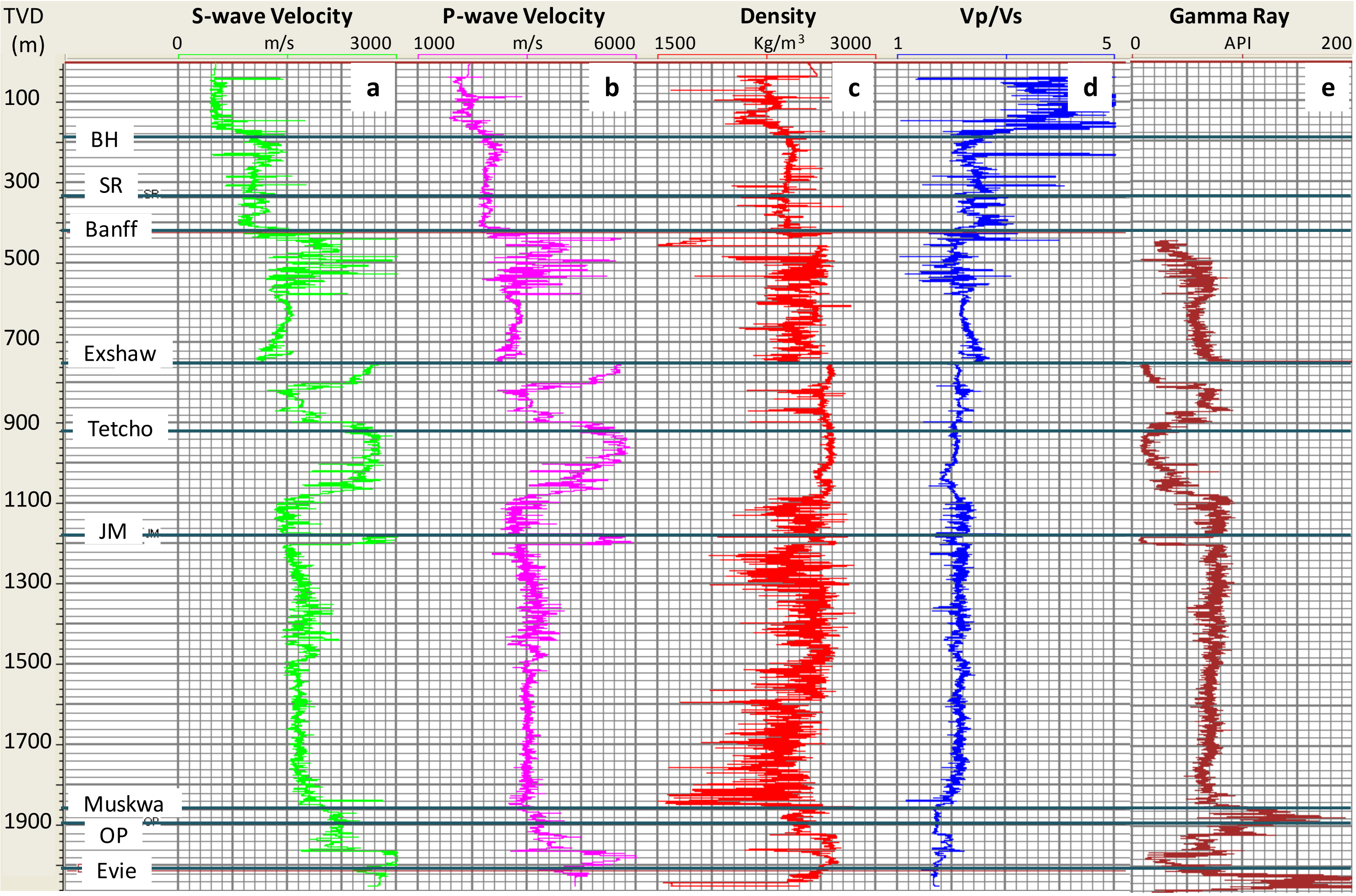

Figure 4-1. Well log from the area. a) S-wave velocity log. b) P-wave velocity log. c) Density log. d) Vp/Vs log and e) Gamma Ray log.

4.3 Well correlation to shot records

Well log information is usually used to generate synthetic seismograms which are one way to predict the seismic response of the earth. They are generated by convolving the reflectivity obtained from the well logs (velocity and density) with an assumed wavelet (e.g. Ricker wavelet) or a wavelet derived from the seismic data. Interpretation can be improved by comparing the markers from the well with major reflections from the seismic records.

Synthetic seismograms were generated with the software Syngram (Figure 4-2), and tied to shot gathers (Figure 4-3, Figure 4-4). These shot gathers are from the refraction survey acquired in the area of study, from which the refraction analysis was described in the previous chapter. The synthetic seismograms were generated with a Ricker wavelet of 40 Hz for the PP data and 20 Hz for the PS data; these values represent the difference in frequency content between the two modes. The maximum offset used was 1000 m which is fairly close to the maximum offset used in the refraction survey.

Figure 4-2 shows the Vp, Vs and density logs with tops to the left, PP synthetic gather (compressional) in the middle and PS synthetic gather to the right. Five reflectors can easily be recognized in both synthetics: Bucking horse, Banff, Exshaw, Jean Marie and the base of the Otter Park Formations. Spirit River and Muskwa Formations have less energy than the previously mentioned but still can be recognized. The time for the deepest reflection in the PP gather is around 1.2 seconds and in the PS gather is around 2.1 seconds.

Figure 4-3 shows a PP synthetic gather to the left and the actual shot gather from the seismic survey to the right. Figure 4-4 shows the PS synthetic gather to the left and the actual converted-wave shot gather from the seismic survey to the right. All shot gathers have maximum offset of 1000 m. These two figures show good agreement between the generated synthetic seismograms and the field seismic data; the main reflectors can be detected on the shot gathers and correlated with the synthetic gathers (arrows in the figures); For the PP synthetic, the shot record is located close to the well. For the converted-wave data, the time of the reflectors is slightly different between the synthetic and the actual shot because the latter is located quite far from the well (~5 km away). The converted-wave shots close to the well log did not have a good signal to noise ratio, and therefore the reflectors could not easily be identified. The agreement for the P-wave data is excellent, except for the shallow reflectors which are contaminated with ground roll. An F-K filter was applied to attenuate this noise but still the shallow reflectors are still not particularly clear. From the quality of the shot gathers, we anticipate good stacked sections, especially for the PP data.

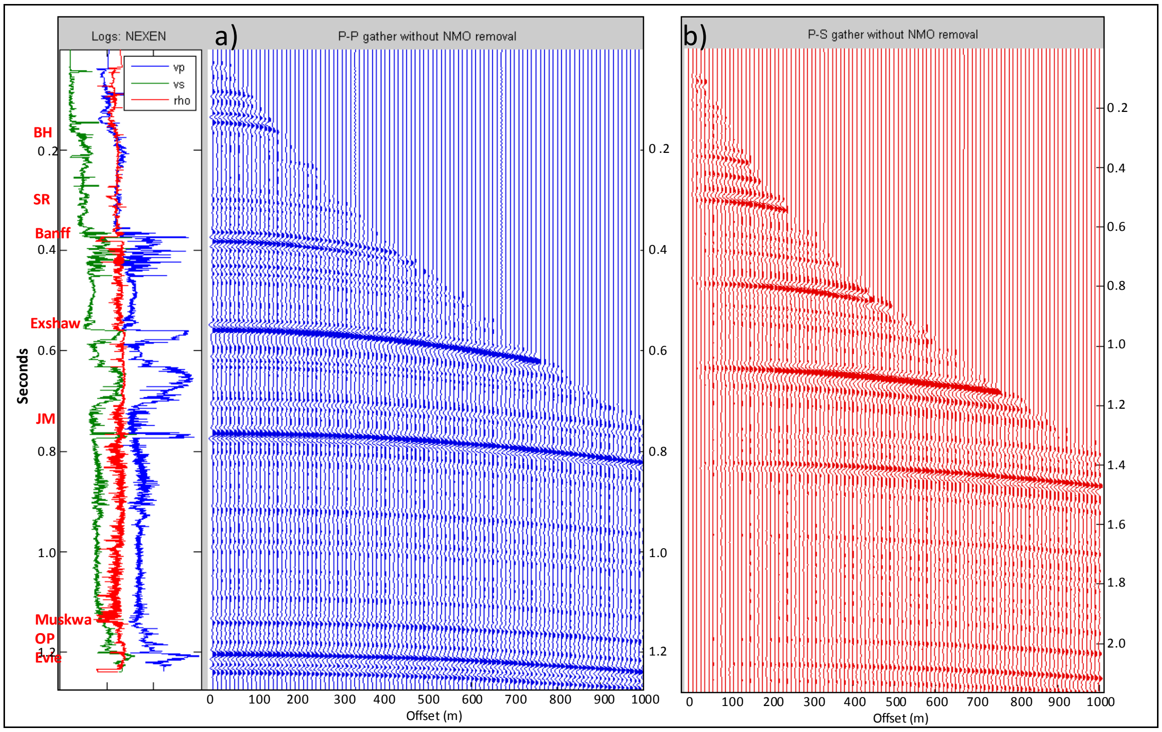

Figure 4-2. Synthetic seismogram in time. a) PP gather and b) PS gather where the main reflectors can be identified. Tops are shown on the left.

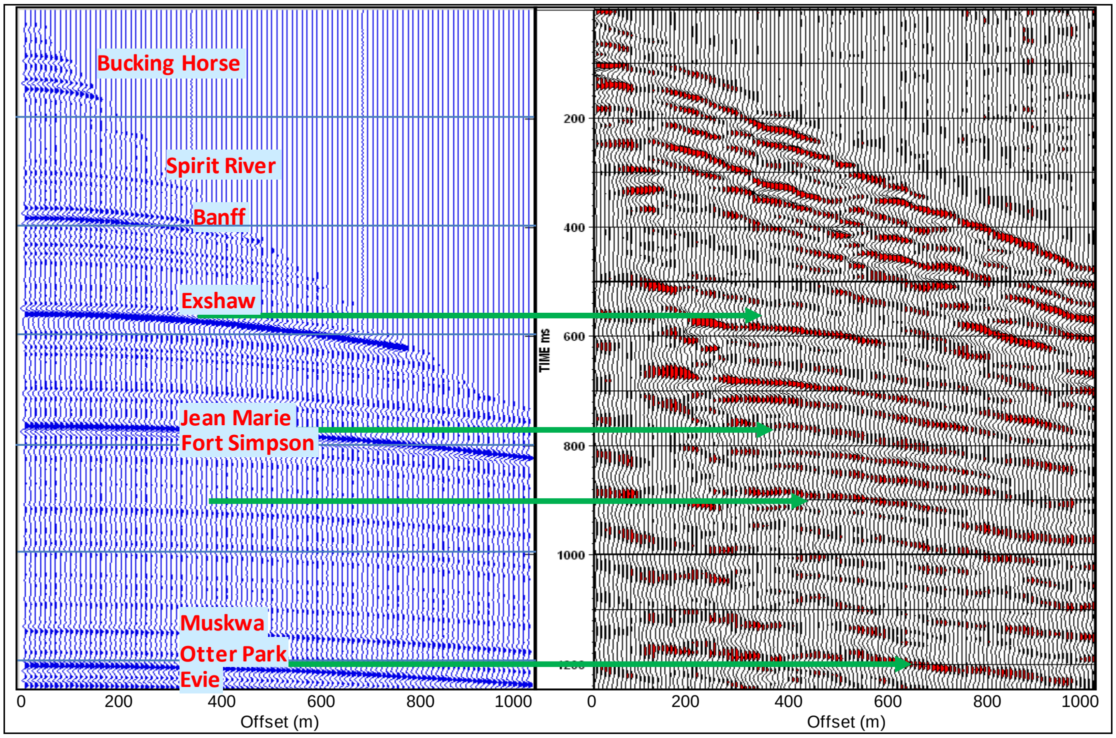

Figure 4-3. Synthetic P-wave (PP) gather in time (left), field P-wave shot gather (right).

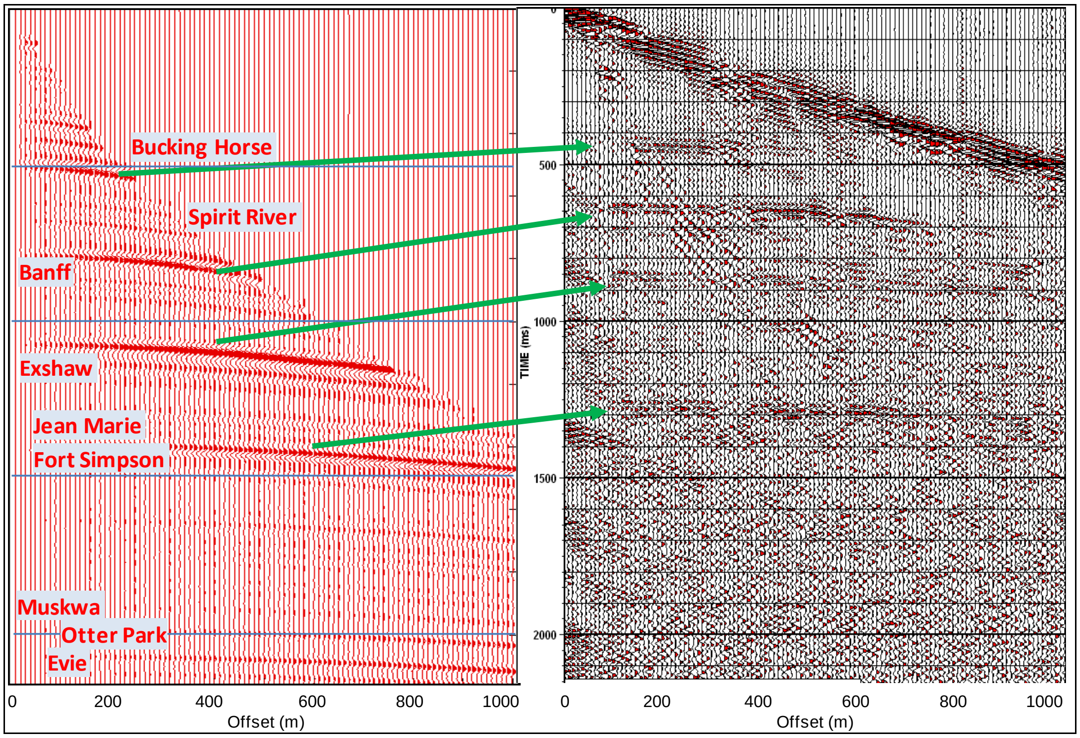

Figure 4-4. Converted-wave (PS) gather in time (left), field PS-wave shot gather (right).

4.4 Near-surface Vp/Vs analysis

Vp/Vs analysis was undertaken only for Line 104, which has good quality for both P- and S-wave data. Lines 101 and 103 have only one mode of data. From the velocities obtained through the refraction analysis, Vp/Vs was calculated for the near-surface layers and the results are shown in Figure 4-5 (left). Notice the high Vp/Vs values for the first layer, reaching values up to 6. This value is influenced by the low velocity material present in the channel area that affects the S-waves more than the P-waves. For shallow layers, values of 3 to 4 are expected. At greater depth Vp/Vs reflects the usual value expected for this relationship for consolidated sediments, which is between 2 and 3. The results are comparable to the values obtained from well log data described in section 4.2. Figure 4-5 shows the shallower 400 m of the well log (right). Ratios of 4 to 5 are found between 40 m and 180 m, and 2 to 3 between 180 m and 400 m.

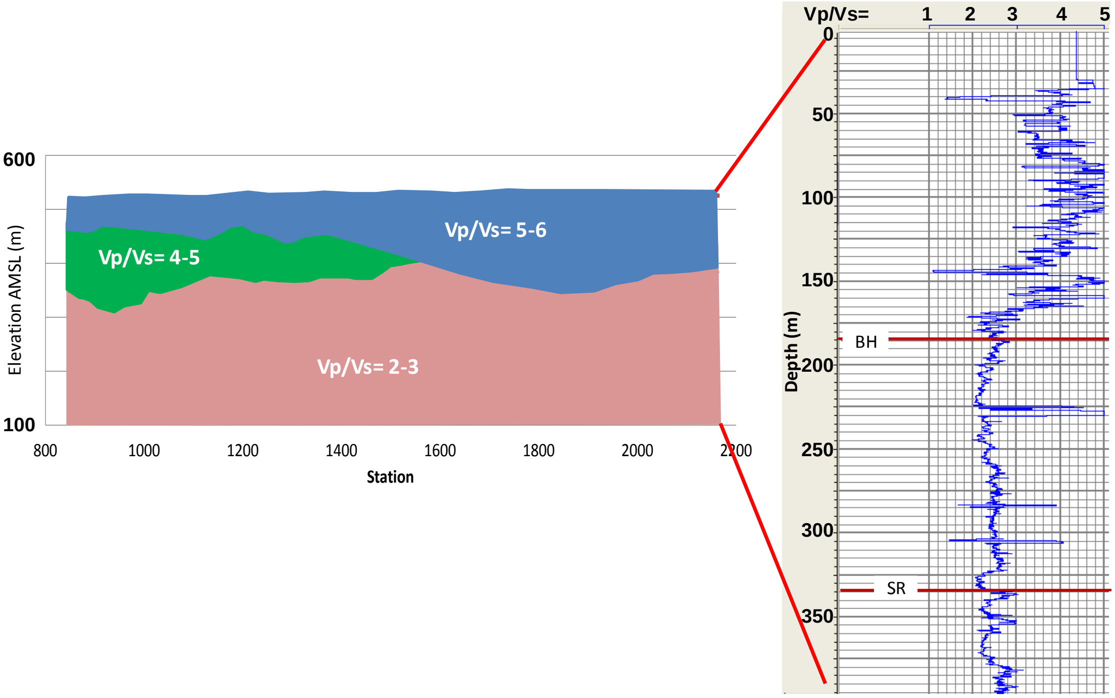

Figure 4-5. Vp/Vs along the profile obtained from the plus-minus analysis (left) compared Vp/Vs extracted from a nearby well.

4.5 Deep Vp/Vs analysis (PP – PS Registration)

One way to obtain Vp/Vs is from velocity analysis performed during processing of each section mode; the weakness of this method is the difficulty in precisely and accurately determining the subsurface velocities from surface seismic data (Tatham, 1991). For this reason, the ratio is usually determined from time measurements alone. Once the structural interpretation and reflection correlation of the data have been performed, Vp/Vs can be calculated using the interval time measurements of the fully processed stacked section. For shear data, Vp/Vs can be obtained from t_s/t_p, or the ratio of the correlated time intervals. This process is referred as registration.

For converted waves, P- and S-wave velocity ratio (Vp/Vs) can also be calculated from the P-wave (PP) time and converted wave (PS) time extracted from stack sections, if reflections from the same interface can be identified on PP and PS data sets. The following relationship is used to register the PP and PS data.

$$V_P/V_S = (2*\Delta T_{PS} - \Delta T_{PP}) / \Delta T_{PP} \qquad (4.1)$$

where ΔT_{PS} is the converted-wave time difference between two chosen events and ΔT_{PP} is the P-wave reflection time difference between the same two events. The time difference between matching events of the two data sets, read from shot records, was used to calculate Vp/Vs ratio with equation 4.1. The calculated values and the values from the well logs are shown in Table 4.1. The calculated values and those from the well log are similar. The use of this equation is recommended for layer thickness greater than a seismic wavelength (Emery and Stewart, 2006)

Table 4-1. Vp/Vs ratio from the well log

Tops		**Tp**	**Ts**	**ΔTpp**	**ΔTps**	**Vp/Vs**	**Vp/Vs from well**
Bucking Horse	BH	0.18	0.41	0.18	0.41	3.56	4.0
Spirit River	SR	0.32	0.65	0.140	0.240	2.43	2.5
Banff	Banff	0.38	0.75	0.060	0.100	2.33	2.0
Exshaw	Exshaw	0.55	1.05	0.170	0.300	2.53	2.3
Jean Marie/ Fort Simpson	JM/FS	0.78	1.40	0.230	0.350	2.04	2.0
Muskwa/Otter Park	M/OP	1.13	1.95	0.350	0.550	2.14	2.2
Evie	Evie	1.20	2.05	0.070	0.100	1.86	1.7

Sensor Geophysical carried out the processing of the seismic data from Line 104. Table 4-2 shows the processing sequence and Figure 4-6, Figure 4-7 and Figure 4-8 show the sections obtained from processing the PP data, the shear (SS) data and the PS data. The synthetic trace shown in red in these figures was used to generate the synthetic seismograms needed for correlation between the tops in the well and the correspondent event in the seismic data. This correlation was the starting point for interpretation of the different horizons. The channel that was indentified from both the electromagnetic survey and the refraction method can be seen between CDP ~1800 to CDP ~2100 and it is highlighted with a red ellipse in Figure 4-6 and Figure 4-8. The main formation picks in the area are also included in these figures. The PP data shows very good quality with continuous reflection events detected until 1.7 seconds. The SS and PS sections show appreciably good results with reflection events up to 2 seconds and 2.4 seconds, respectively. However for the SS data, only the Banff and Exshaw formations can be interpreted as deeper horizons are not detected in this section. The clinoforms characteristic of the Banff formation and the Debolt lapping out on top of the Banff formation can be distinguished in these sections.

Table 4-2. Processing sequence for the PP data, SS data and PS data by Sensor G.

	PP	SS	PS
Geometry assignment, trace edits and kills	x	x	x
H_1/H_2 Rotation: 20 degrees.		x	x
Amplitude recovery: Spherical divergence correction + 4 dB/Sec Gain	x	x	x
Singular Value decomposition (SVD) filter to remove ground roll,	x		x
FK filter to remove surface generated noise	x	x	
Surface-consistent deconvolution (Spiking): 100 ms operator length, 0.1 % Prewhitening	x	x	x
Vibroseis Decon compensation	x	x	x
Refraction static corrections, Datum 600 m, Vr = 2200 m/s (PP, PS), Vr = 1200 m/s (SS), 2 layers	x	x	x
Surface-consistent Statics	x	x	x

	PP	SS	PS
Surface-consistent Amplitude scaling	x	x	x
T – F Adaptive Noise Suppression, Offset consistent Gain Control	x	x	x
TV Spectral whitening	x	x	x
Normal moveout correction. Front end mute. Automatic gain control	x	x	x
CDP stack mean + 100 ms bulk shift (PP, PS). + 300 ms bulk shift (SS).	x	x	x
TV Spectral whitening	x		
FK filter to remove surface generated noise		x	x
Trace equalization. F-X Filtering. Diffusion filter	x	x	x
FD Time migration. Band pass filter	x	x	x
Trace equalization	x	x	
Time Variant scaling: mean, centre-to-centre, multiple gates			x

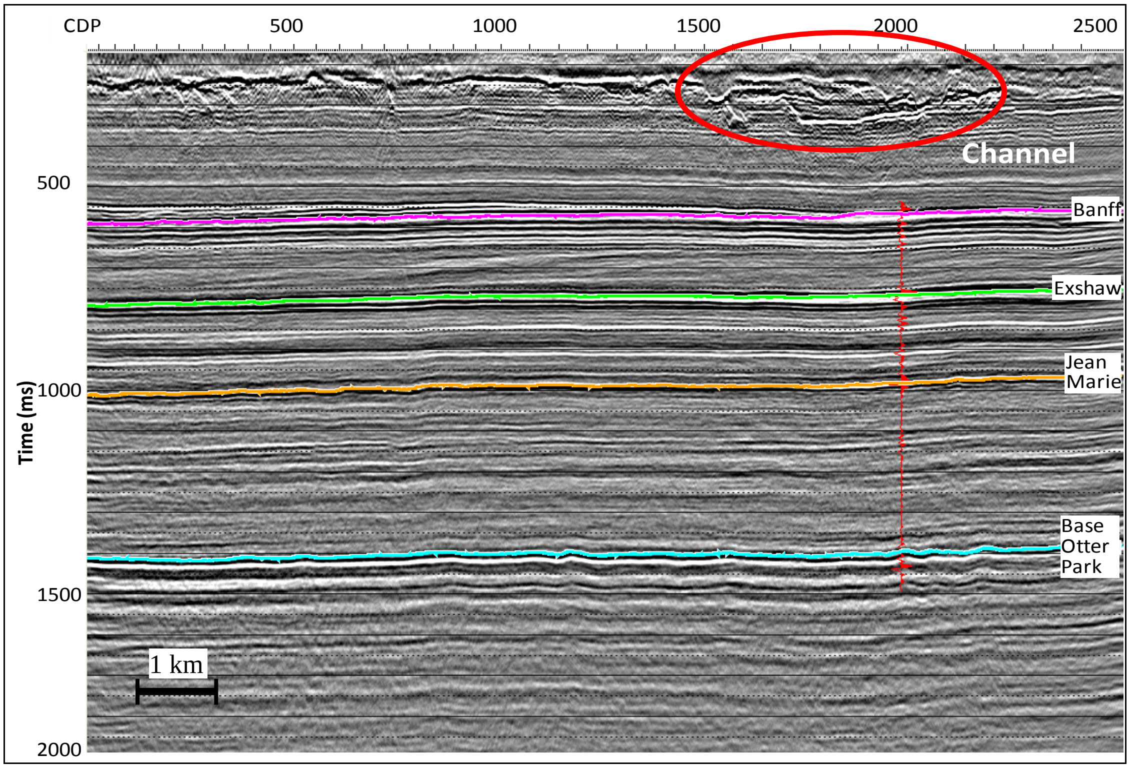

Figure 4-6. P-wave section after post-stack migration. Synthetic trace is shown in red. The total length of the line is 13 km.

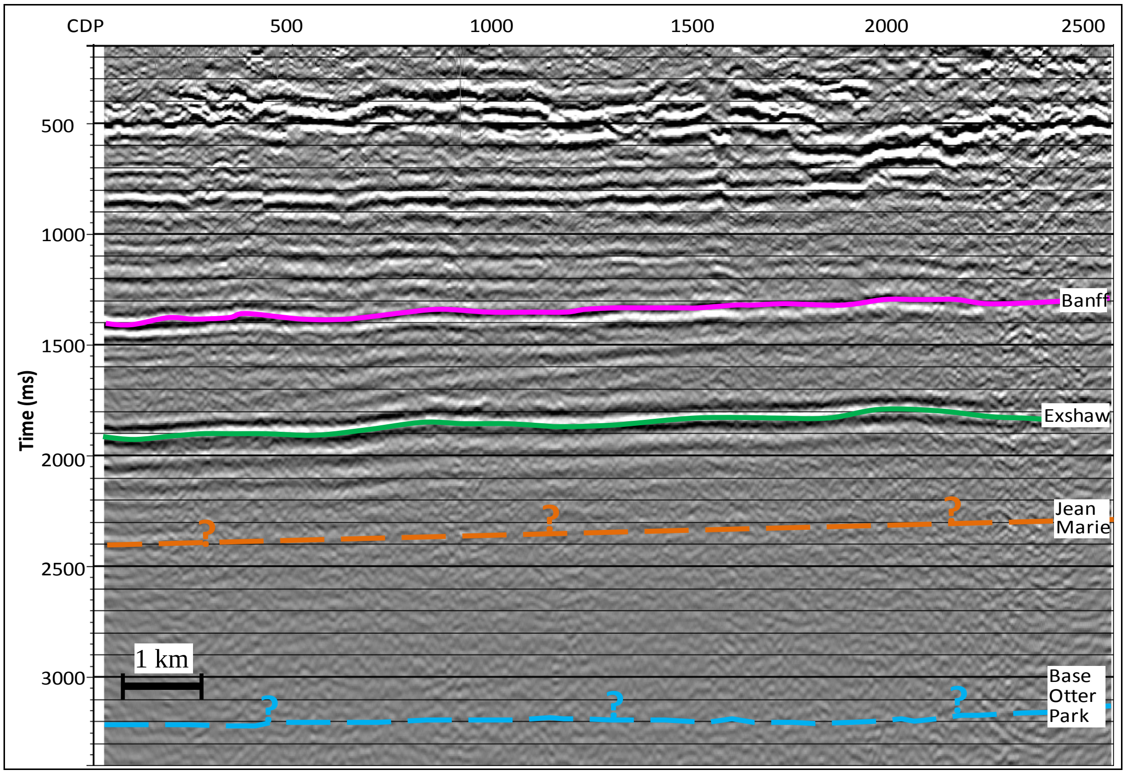

Figure 4-7. SS section after post-stack migration.

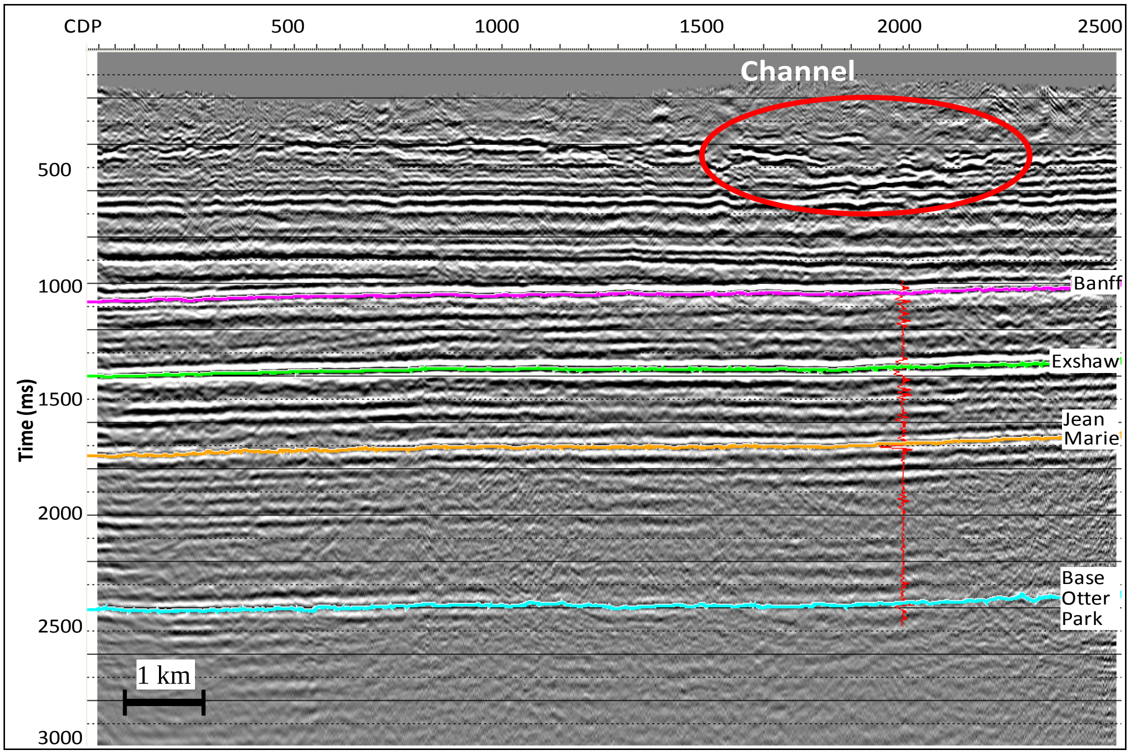

Figure 4-8. PS section after post-stack migration. Synthetic trace is shown in red.

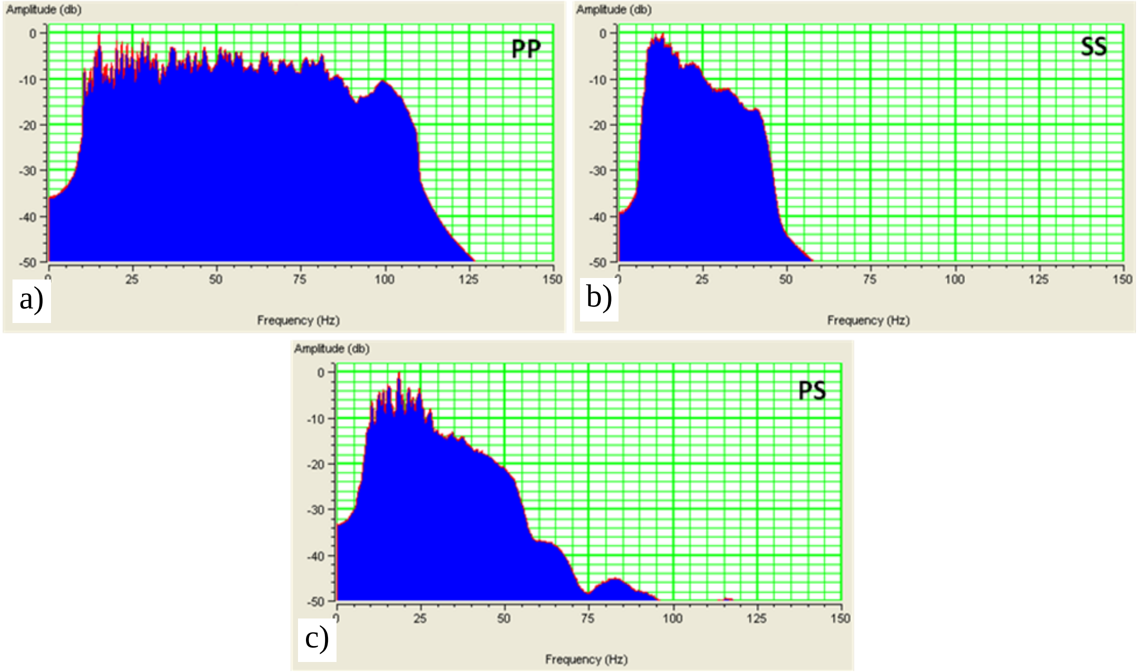

Figure 4-9. Amplitude spectra from a) the PP stacked section, b) the SS stacked section and c) the PS stacked section.

Figure 4-9 shows the amplitude spectra for each of the stacked sections. Here we can appreciate the difference in frequency content between the different wave modes. The PP-wave data has the broadest frequency bandwidth, from 5 Hz to 110 Hz; SS wave-data have frequency band from 5 Hz to ~45 Hz and the PS-wave have frequency band from 5 Hz to 55 Hz. Frequencies below10 Hz are highly attenuated in all sections. PP-wave data present a fairly flat spectrum while SS-wave data shows the highest frequency attenuation.

Registration was performed with Hampson-Russell ProMC software package. The main reflectors interpreted in the PP and PS sections were: Spirit River (SR), Banff Formation, Exshaw Formation, Jean Marie Formation (JM) and the base of the Otter Park (OP). Most of the major P-wave reflections in this section can be visually correlated with the PS reflections. Sections are easier to compare if they are at a similar scale corresponding to depth; hence the P-wave data were plotted at a scale of 1.5 times that of the PS data.

Considering that waves are traveling in unconsolidated media in the shallowest section, the ratio between the arrival time for PP waves and PS waves is high, but it decreases with depth. The structural similarity between both sections is the main tool for correlation. The Spirit River event is the first reflector interpreted but it was not used for the event matching due to lack of continuity in the PS section. The first strong and continuous PP reflection, the Banff Formation, at 560 ms was correlated with the PS reflection at 1010 ms. This event is very strong and continuous in the PP section, but precise identification of the event is needed to avoid interpreting the Debolt that lies over the Banff formation. The correct interpretation is confirmed with the value of Vp/Vs obtained for that interval after event registration; if this value is significantly different from that of the well log, it means that the horizon was interpreted incorrectly. The second interpreted reflector, the Exshaw Formation, is observed as the strong reflection at 755 ms on the PP section, which is correlated with a reflection at 1340 ms on the PS section. The Jean Marie Formation, observed at 963 ms on the PP section, was correlated at 1660 ms on the PS section. Finally, the base of the Otter Park Formation that can be appreciated as a strong event in the PP section at 1400 ms was correlated with an event at 2300 ms in the PS section. This last event was discontinuous along almost half of the line.

Event matching was applied to generate interval Vp/Vs shown in Figure 4-10. This Vp/Vs values were obtained with the information of interval times between horizons of interest and applying equation 4.1; the ratio is represented by the colors and values on the seismic section. Comparison with Vp/Vs from the well log overlain on the left of Figure 4-10 shows differences of ±0.1 between them. This ratio can be used to identify specific lithologies; in this case the formations are mainly dominated by shale (Banff Formation and deeper). The shallow layer does not represent entirely the real values because the Bucking Horse marker (BH) was not an easy reflector to follow along the line preventing robust event matching in this shallow section. If a well close to the line was available, the interpretation could be tuned and a better Vp/Vs function could be obtained. After doing event registration, it is possible to change domain from PS time to PP time for the PS-wave section. A comparison between the PP section and the PS section in PP time is shown in Figure 4-11. Good agreement can be observed between the two sections. This is a very promising data set where good registration is demonstrated. This method allow us to be sure about the PS interpretation because if incorrect Vp/Vs values are obtained after event matching, that suggests this interfaces do not correspond properly in depth between the PP and PS sections. Most likely the error would be in the PS interpretation. Reliable correlation will lead to geologically reasonable results.

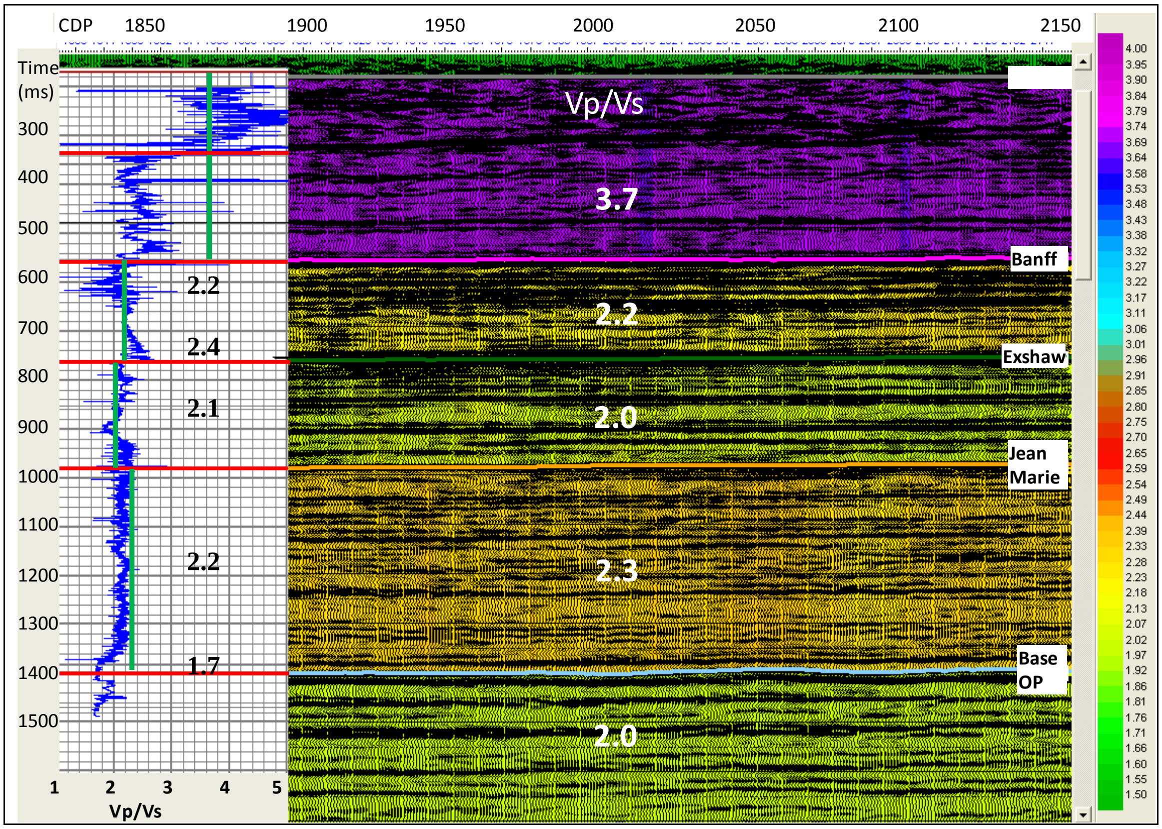

Figure 4-10. Vp/Vs after event registration. The well log data is shown to the left of the section.

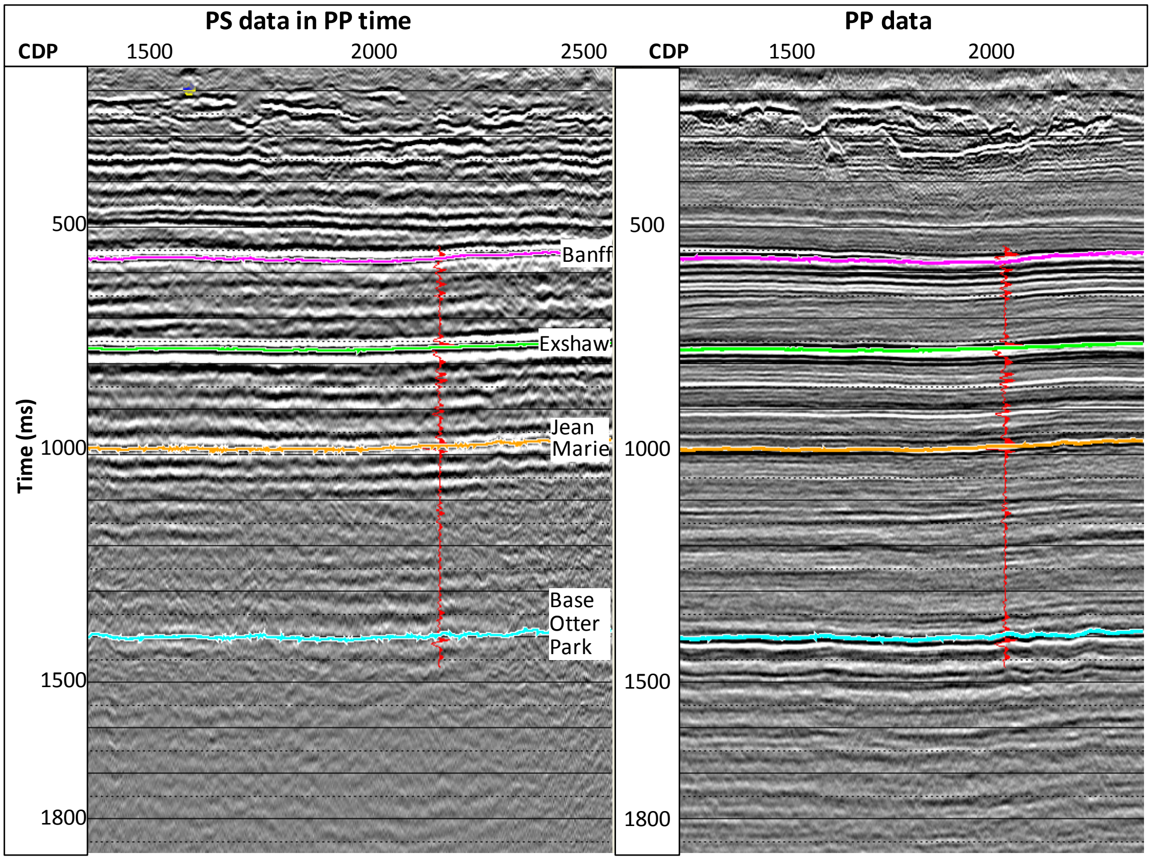

Figure 4-11. PS data displayed in PP time (left) versus PP data (right) after PP-PS registration.

The calculation of interval Vp/Vs was refined by adding well control to the process. This step produced high frequency vertical variations in Vp/Vs from the sonic logs, i.e. the stratigraphy at the well location. First, a wavelet was extracted from each seismic section to generate the synthetic seismograms. Figure 4-12 shows the statistically extracted wavelet from PP (left) and PS (right) sections; The PP wavelet was phase rotated by 60 degrees and the PS wavelet was rotated by -70 degrees to better fit the field data. The difference between the two wavelets is due to near surface effects, frequency-dependant absorption or artifacts generated by processing. The amplitude spectrum from each wavelet is shown in this figure which reflects the frequency of each seismic mode i.e. higher frequency content for PP than for PS data; this figure compares to the amplitude spectrum shown in Figure 4-9. These wavelets were convolved with the reflectivity log calculated from the density and corresponding velocity (Vp or Vs) from the logs to create a PP synthetic seismogram and a PS synthetic seismogram (Figure 4-13). After that, correlation between these synthetic seismograms and the actual seismic was performed by linking the tops from the well with the corresponding events in the seismic data, that is, seismic-well tie. This process was carried out for both, PP and PS data. Note in Figure 4-13 good correlation especially for Exshaw, Jean Marie and Otter Park Formations. Following, event matching with the same 4 horizons used before (Banff, Exshaw, JM and OP) was performed which produced a new Vp/Vs with a range in values between the horizons matched. This result is shown in Figure 4-14. Once the major event markers have been identified and the well logs tied to the seismic data, velocity models are created by interpolating the well-derived velocities along seismic horizons. This results in high resolution for the velocity variations along the matched horizons.

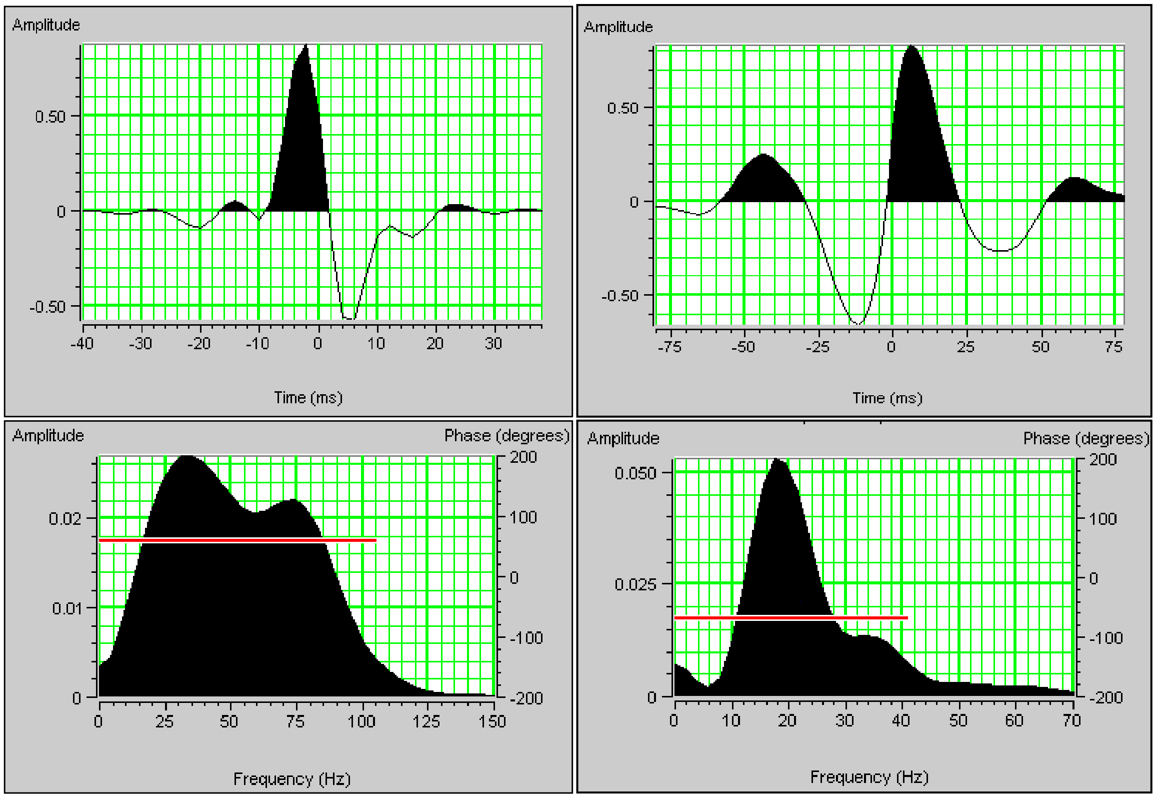

Figure 4-12. Statistically extracted wavelet from PP section (left) and PS section (right) for seismic well tie. The top figure shows the wavelet in time domain and the bottom the corresponding amplitude spectrum. Red line indicates the phase.

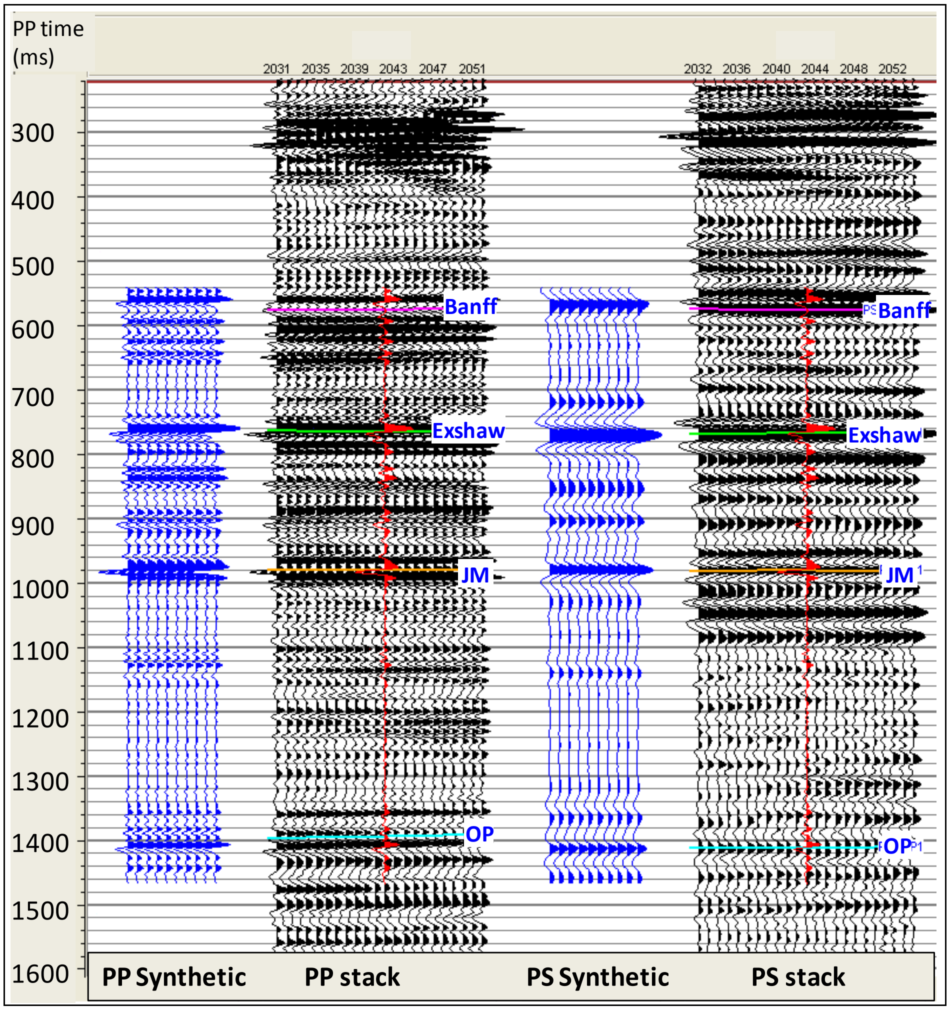

Figure 4-13. PP and PS synthetic seismograms (blue) with corresponding seismic traces (black) extracted from the actual data.

Successful joint PP – PS interpretation depends on identifying and registering the same reflectors in both sections. This task is especially challenging in the shallow sediments due to high ratio of P to S velocities which causes large differences in the corresponding traveltimes (Fomel et al., 2003). Wrong correlation of key reflectors will produce erroneous seismic-based attributes (Vp/Vs ratio, Poisson's ratio, shear modulus, and bulk modulus) and make accurate interpretation impossible (DeAngelo et al., 2003). Accurate registration of PP and PS time migrated images allows us to extract high resolution estimates of Vp/Vs, a very important physical attribute for subsurface characterization.

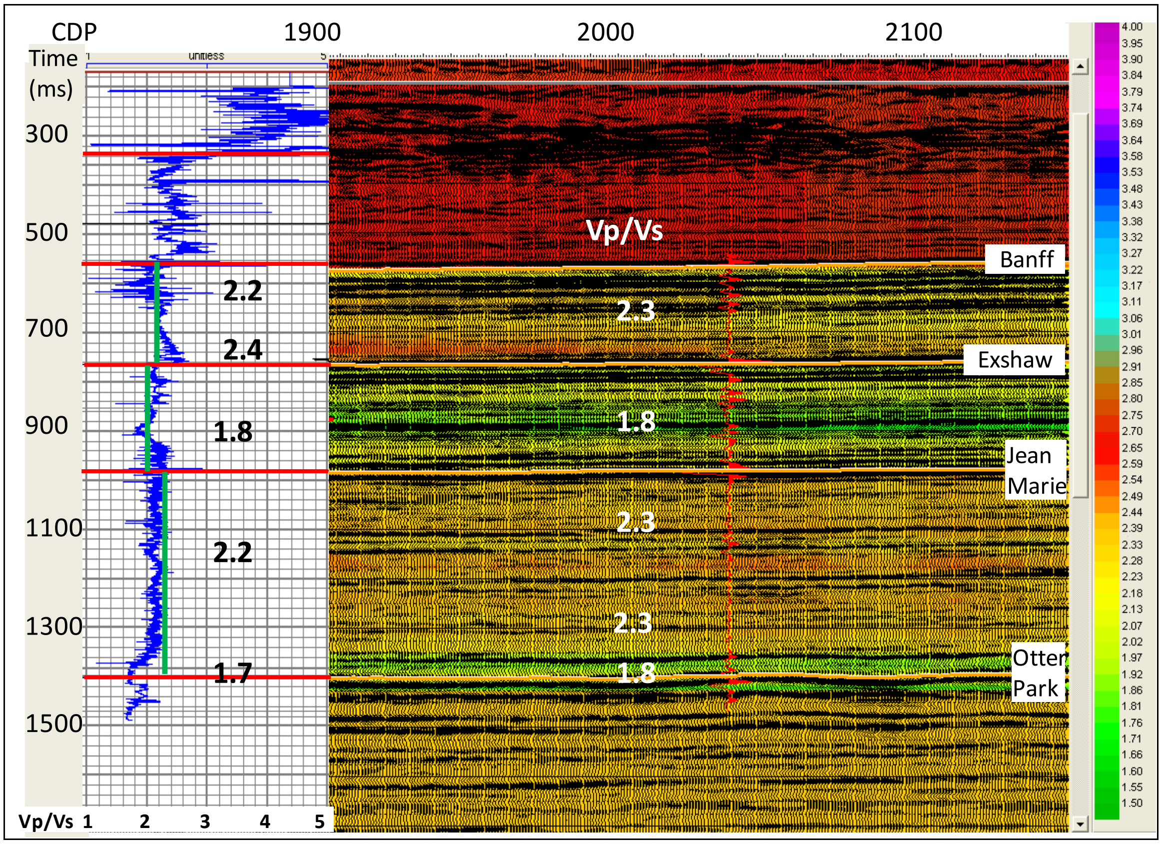

Figure 4-14. Vp/Vs result after adding well log control to the process of PP – PS registration. Vp/Vs from the well is shown on the left.

Vp/Vs anomalies will be generated when the correlation between the same reflectors in both sections fail. Unreliable values, too high or too low, will be presented in one interval and will affect the following interval with an opposite trend (opposite low or high). This situation deteriorates as the thickness of the layer decreases as they are more difficult to correlate.

4.6 Summary of this chapter

This chapter presented the results of Vp/Vs analysis for the near-surface as well as for deeper formations. A well log was available as a control point with the complete borehole depth being recorded (from 40 m to 2054 m depth). The velocities generated through the refraction analysis were used to calculate Vp/Vs in the near surface and were compared to those values obtained from the well log. For deeper formations, Vp/Vs was obtained through interval times from interpretation and, these values were also compared to Vp/Vs values from the well log. Differences between Vp/Vs calculated from the refraction analysis and those obtained from the well log are within a ±0.1.

Chapter Five: **PS SURVEY DESIGN**

5.1 Introduction

The objective of seismic acquisition is to obtain final images of the subsurface that allows seismic inversion. This objective imposes demanding requirements on the acquisition design to obtain the desired accuracy and quality from the seismic data (Veldhuizen et. al., 2008).

As mentioned in chapter one (section 1.5), for converted waves (PS) the reflection point is not centered between source and receiver points. The conversion point lies closer to the receiver points, depending on the Vp/Vs ratio and depth. Vp/Vs analysis discussed in chapters 3 and 4 were used as input into the design process. At higher ratios, the conversion points get closer to the receiver. Due to the asymmetry in the common converted point (CCP) domain, a design that produces uniform fold for P-P mode does not necessarily produce uniform fold for PS mode and to make the latter uniform can be a difficult task (Musser, 2003).

The case study described in this chapter is located in the same area where the refraction survey was acquired. This is an exploratory area and multicomponent data will be acquired; a significant effort has been invested with the previous analysis and with the survey design in order to provide optimum quality data and to maximise the desired results.

5.2 Acquisition footprint analysis of a 3D-3C seismic survey in NEBC

The main objective of this case study was to predict acquisition footprint, which refers to patterns seen on 3D seismic time slices that reflect the geometry used to acquire the survey or some features present on the surface such as rivers, lakes or any other obstruction; these patterns obscure the actual amplitude anomalies under consideration for stratigraphic interpretation, AVO analysis and reservoir attribute studies. Footprint geometry is a product of a variety of causes, for example: changes in S/N due to fold variations from bin to bin, azimuth and/or offset polarization, remaining multiple noise after stack as a result of offset and azimuth variation, and failure of DMO to produce constructive interference caused by lack of offsets in some bins (Cordsen, 2000). For this study OMNI software was used.

Four different geometries were tested: Orthogonal, slant, double brick, and triple brick. The last two were discarded due to environmental restrictions. This is a very sensitive area so the cutting of lines and their impact should be minimized. The input parameters for the 3D design, obtained from exploration objectives and from existing 2-D seismic data, are shown in Table 5-1.

Table 5-1. 3-D design input parameters.

Fold of good 2-D data: 96
Steepest dip: 10°
Mute for shallow markers needed for isochroning: 500 m (shallow target)
Target depth: ~2700 m
Target two way time: 2.9 s
V_{int} immediately above the target horizon: 2880 m/s – 3440 m/s
F_{dom} at the target horizon: ~50 hz
F_{max} at the target horizon: ~80 hz
Lateral target size: N/A
Area to be fully imaged: 300 km^2
Layout method: Orthogonal and Slant

Based on this information the initial survey design parameters were calculated (Cordsen, 2000). The results are shown in Table 5-2. There are some recommended rules to be accomplished when doing survey designs, as follows:

The minimum fold required should be half of the 2D fold (if the S/N is good) up to 2D fold (if high frequencies are expected). The bin size should be such that uses 3 to 4 traces across the target (for a thin target as a channel), avoids aliasing in the frequency (equations 1.22 and 1.25), provides 2 to 4 samples per wavelength of dominant frequency and meets the required lateral resolution. The minimum offset should be smaller than the shallowest reflector of interest. The maximum offset is set up as approximately the depth of the deepest target. The migration aperture must exceed the radius of the Fresnel zone, the diffraction width for an upward scattering angle [Z (tan 30°)] and the dip lateral movement after migration, which is Z (tan θ)

Table 5-2. 3-D design flowchart.

Parameter	Definitions and requirements
Desired fold= 48	(1/2 to 1) full 2D fold = 48 – 96
Bin Size (B)	a) For target size: Not available. Large target. b) For alias frequency: $B_1= V_{int} / (4f_{max}\sin \theta)$ If V_{int}= 2880, B_2= 51.8 m; If V_{int}= 3440, B_2= 61.9 m c) For lateral resolution: $B_1= V_{int}/(Nf_{dom})$ =28.8 to 14.4 m B_2= 34.4 to 17.2 m (N=2 to 4) Bin size= 30 m (this values was chosen as an appropriate value) RI= 60 m; SI= 60 m
Desired X_{min}*: 500 m	RLI= 240 m (from old surveys in the area) SLI= 360 m (from old surveys in the area) Xmin= $(RLI^2+SLI^2)^{1/2}$ = 432.67 m (less than the shallowest horizon)
Desired X_{max}*: 2700 m	Number of channels in patch= 2000 Number of receiver lines= 20 Channels per line= 100 Cross-line dimension= 4560 m In-line dimension= 6000 Aspect ratio= Cross-line dimension of the patch/ in-line dimension of the patch= 0.76 X_{max}= ½ [(In-line dimension of the patch)^2 + (Cross-line dimension of the patch)^2]$^{1/2}$ = 3768 m (Should be approx the same as the target depth)
Fold	In-line fold= # rec x RI / (2xSLI)= 100x60/(2x360) = 8.33 Cross-line fold= ½ # Rec. Lines= 13 Total fold= 108.33 (more than the desired but it will introduce fold striping as it is a decimal value)
Migration Apron (MA)	Radius of Fresnel Zone= ½ x V_{ave} x (target TWT /f_{dom})$^{1/2}$= ½ (2x2700/2.9) (2.9/50)$^{1/2}$ = 224.2 m Diffraction energy= 0.58*target depth= 0.58*2700= 1566 m Migration apron= target depth x tan (dip)= 2700*tan(10)= 476 m In-line fold taper= [(in-line fold/2) – 0.5] x SLI= 1320 m Cross-line fold taper= [(cross-line fold/2)-0.5] x RLI= 1440 m (FT+FZ) < total mig apron < (FT+MA) 1320 + 224.2 < MA < 1440 + 476 = 1544.2 < MA < 1916 MA= 1544 m to 1916 m

*** Xmin is the largest min offset in a survey and Xmax is the maximum recorded offset. It is usually the half-diagonal distance of the patch**

The calculations shown above confirm the validity of parameters chosen for the design shown in Table 5-3.

Table 5-3. Design parameters for the 3D/3C seismic survey acquisition.

Source line interval	360 m
Receiver line interval	240 m
Source Station interval	60 m
Receiver Station interval	60 m
Patch	20 x 100

Figure 5-1 shows the survey area with the source and receiver layout according to orthogonal (top) and slant geometries (bottom). Source lines are east-west direction and receiver lines are north-south for the orthogonal geometry, and for the slant geometry the receiver lines were changed to 45 degrees. The orientation for source lines was chosen because there are previous wide cut lines from prior seismic surveys acquired in the area that were appropriate for this new acquisition; additionally the subsurface structure is generally flat so there is no need to orient the lines in a specific way. The other parameters were also mainly chosen from previous surveys which demonstrated very good quality. Inside the lakes drawn in these figures, different source and receiver station intervals were tested as the survey is planned to be acquired in winter when the lakes are frozen. Receivers are located every 180 m and sources every 20 m (fewer receivers, more sources). Additionally, some source lines were moved to the existing cut lines to avoid new line cutting. This is economically and environmentally positive.

5.3 Results and discussion

In this section, results and discussion of the designs are presented. PP refers to compressional mode and PS refers to converted mode from P waves to S waves. Here, all the attributes were calculated using the same bin size for both modes to make a proper comparison (30 m x 30 m). If the optimum bin size for the converted waves had been taken, fold would be higher so the comparison would not be as meaningful.

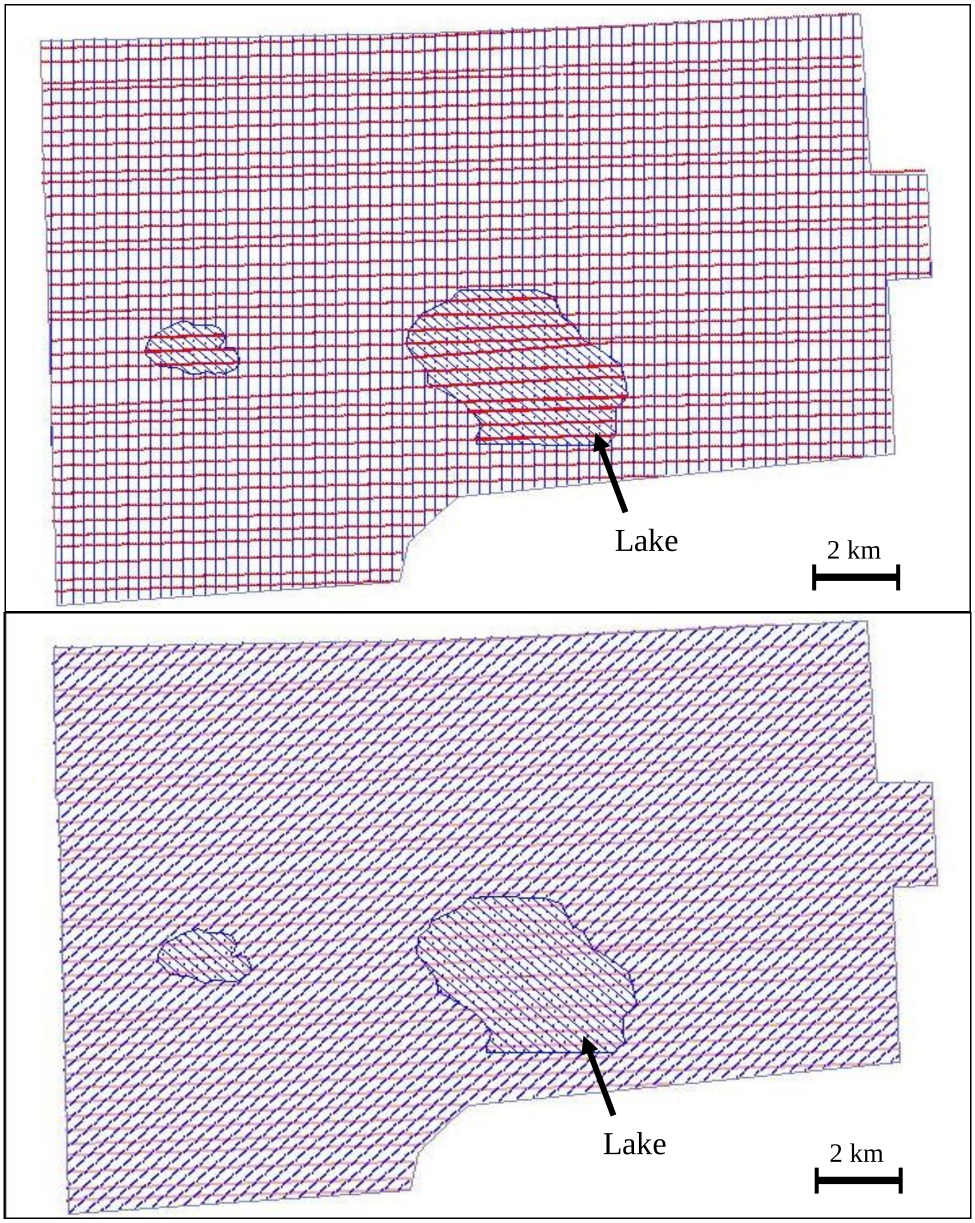

Figure 5-1. Surface layout, orthogonal (top) and slant (bottom). Blue lines are the receiver lines and red lines are the source lines.

Figure 5-2 shows the fold for PP survey, with orthogonal geometry (top) and slant geometry (bottom). Geometry footprint can be appreciated in these figures: we can infer the actual direction of the receiver lines in the slant layout, i.e. 45 degrees, especially around the lake; both geometries show the layout of sources (east-west) because some segments of these lines were moved to previously existing cut lines so the source line interval is uneven, producing stripes of low and high fold in the source line direction. The receiver line direction in the orthogonal geometry is not evident; this is the characteristic that is desirable for the entire layout. Also in these figures, ray paths are shown to highlight the influence of the slant layout of receivers over the offset distribution. The raypaths have longer offsets in the receiver direction.

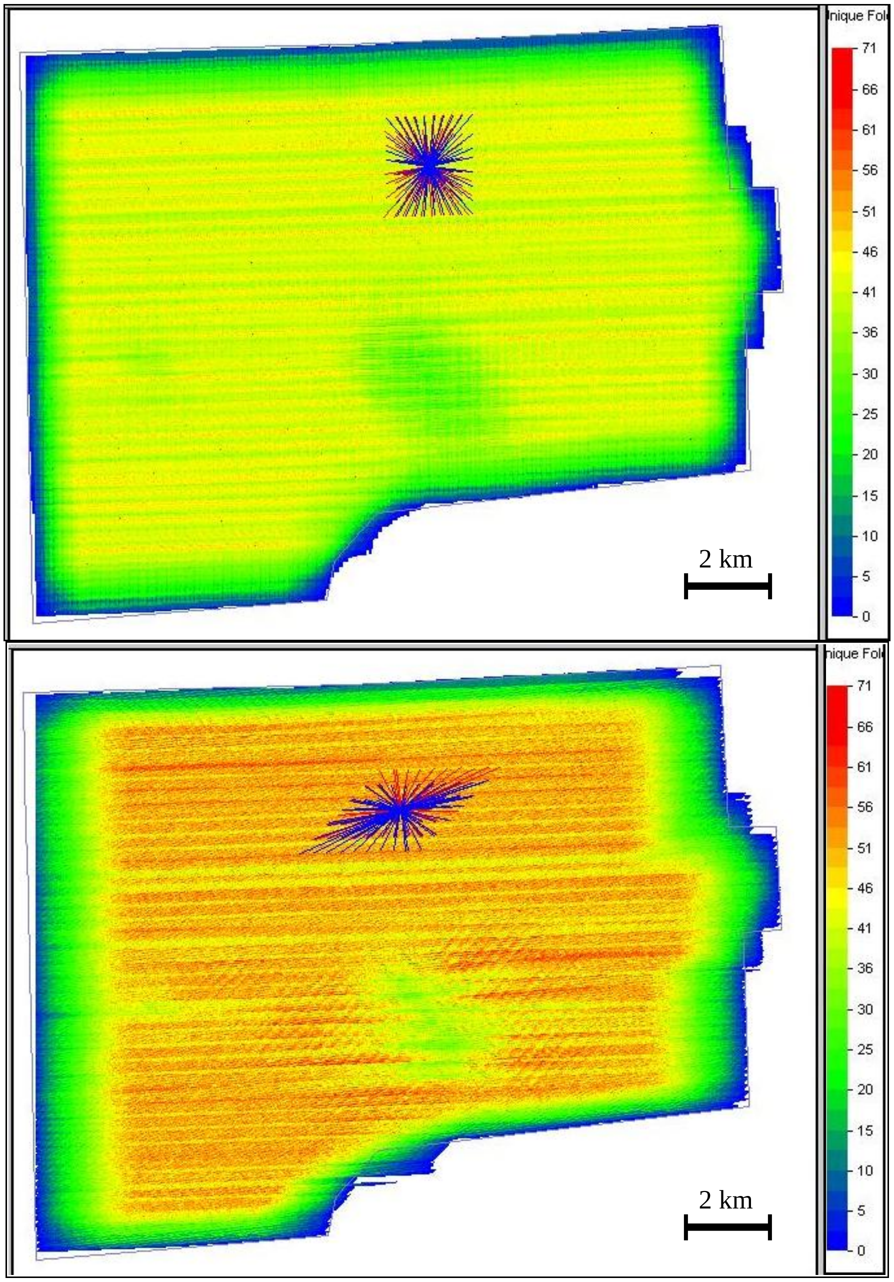

Figure 5-2. PP survey design fold. Orthogonal geometry (top) and slant geometry (bottom). Raypaths are shown in one bin for both geometries.

Figure 5-3 shows the fold for PS survey, with orthogonal geometry (top) and slant geometry (bottom). The footprint of the surface layout is stronger for orthogonal geometry.

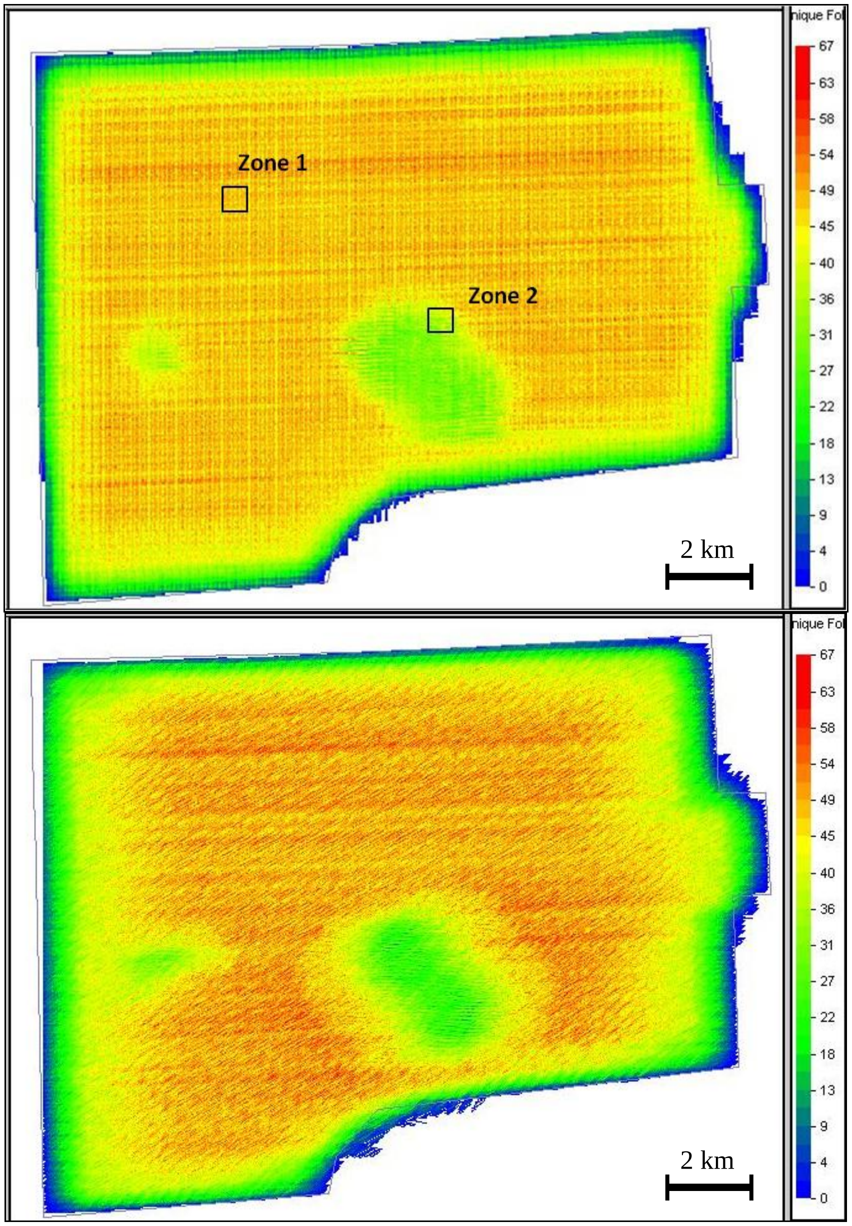

Figure 5-3. PS Survey design fold. Orthogonal geometry (top) and slant geometry (bottom). Black rectangles show areas of detailed analysis in later figures.

Regarding the lake footprint, there is a transition zone from the lowest values inside the lake to the highest values of fold outside the lake for the slant geometry. For the orthogonal geometry this change from lower to higher fold is more abrupt. The area of lower fold is smaller for the slant geometry design in the PP design as well as in the PS design.

Seismic attributes for two different areas marked in Figure 5-3 were looked at in detail: Zone 1 is an area with no influence of the lakes and zone 2 is an area just in the north east border of the big lake. This is shown in Figure 5-4 to Figure 5-11.

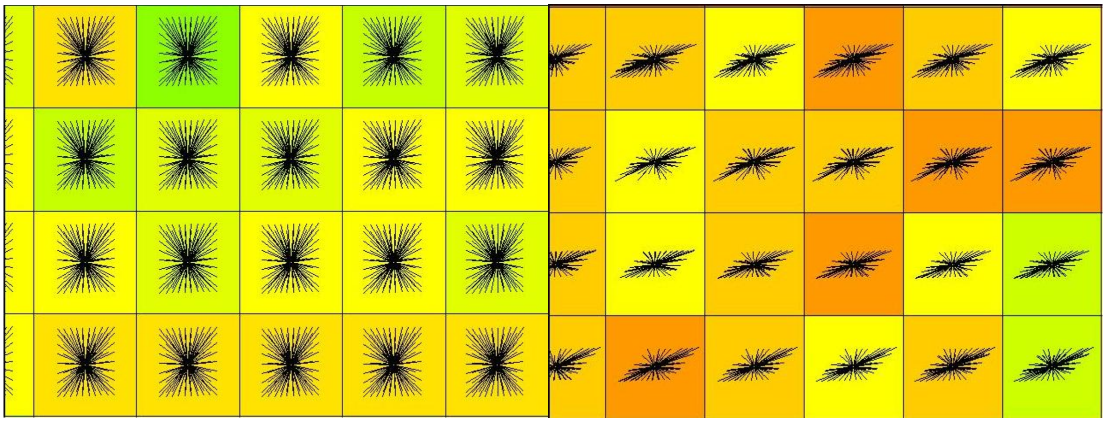

Figure 5-4. Zone 1: Azimuth – PP survey design. Orthogonal geometry (left); slant geometry (right).

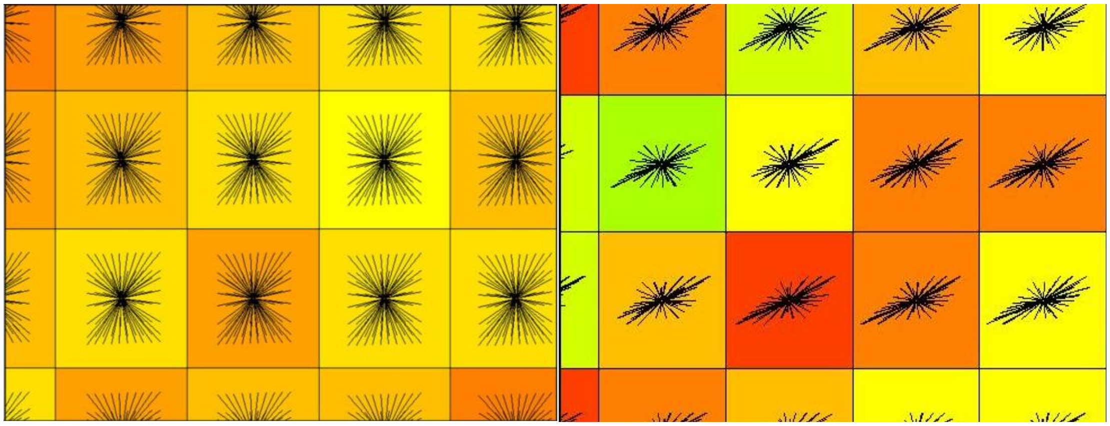

Figure 5-5. Zone 1: Azimuth – PS survey design. Orthogonal geometry (left); slant geometry (right).

Figures 5-4 to 5-7 show the azimuth distribution (spider plot). The squares in these figures represent CMP bins. Bin dimension for the PP design was 30 m x 30 m and it was set the same dimension for the PS design to have the same level of comparison. The direction of the sticks drawn in the bin center indicates the source-receiver azimuth; the length of these sticks represents the source-receiver relative offset. Finally, the color represents the fold with the same scale as in Figures 5-2 and 5-3. Poor azimuth distribution may produce statics coupling problems and failure to distinguish azimuth-dependent variations produced by dip and anisotropy (Cordsen, 2000). Good azimuth distribution improves velocity analysis and amplitude analysis with azimuth (AVOA), (Lansley, 2011).

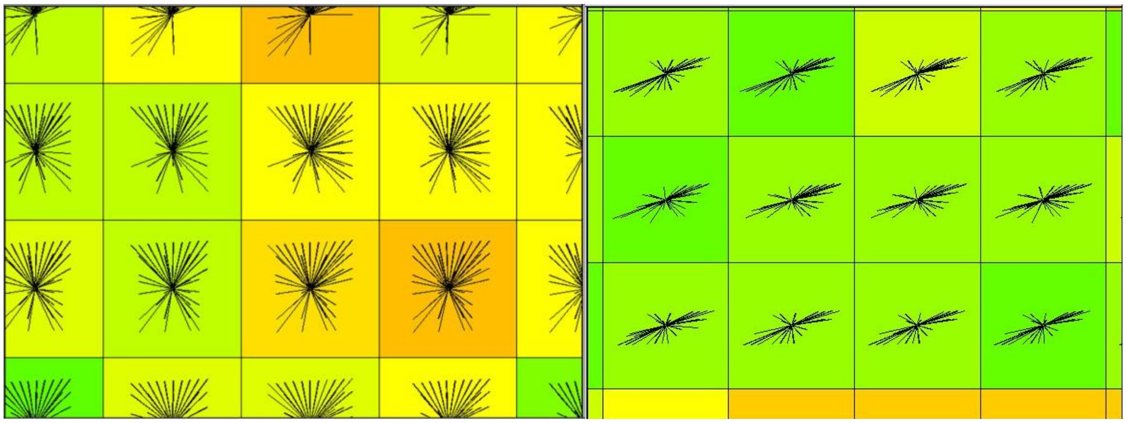

Figure 5-6. Zone 2: Azimuth – PP survey. Orthogonal geometry (left); slant geometry (right).

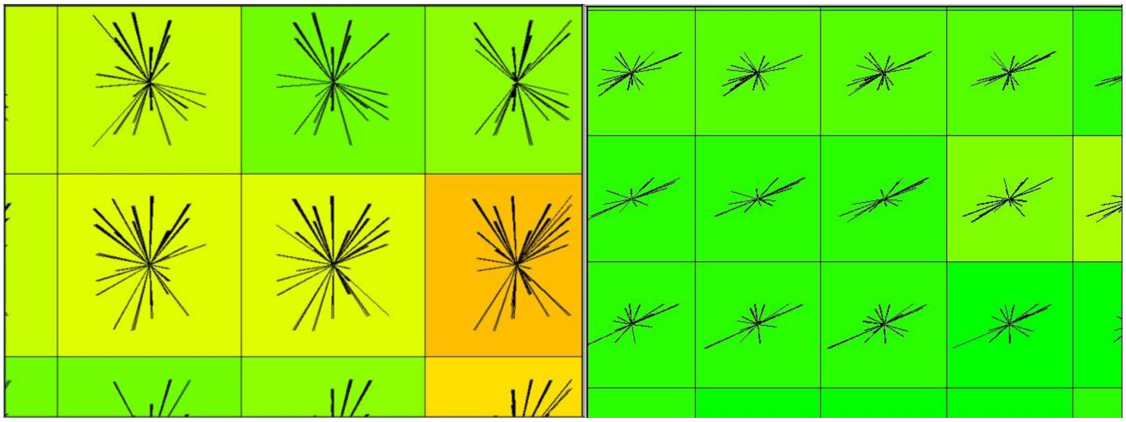

Figure 5-7. Zone 2: Azimuth – PS survey. Orthogonal geometry (left); slant geometry (right).

The azimuth distribution for the orthogonal geometry is uniform if a wide patch is used for recording. For slant geometry, the azimuth distribution is good but depends on the number of receiver lines per shot.

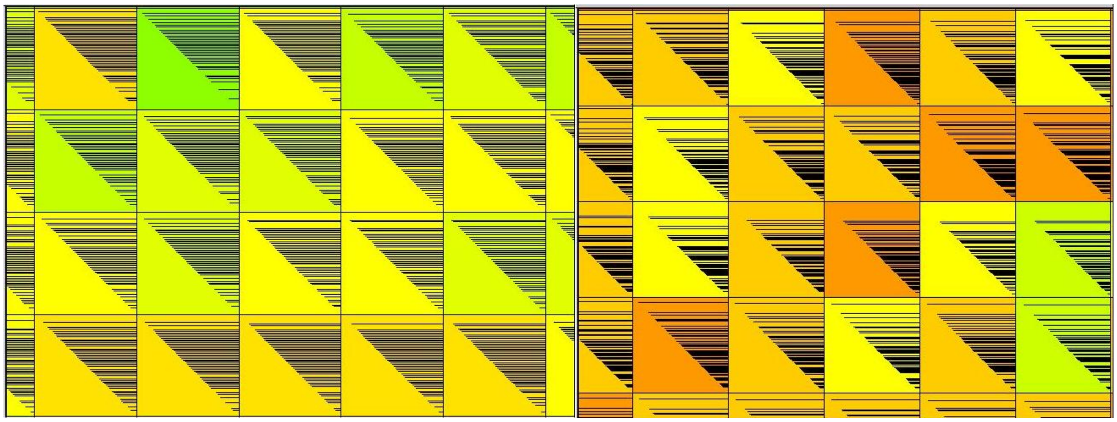

Figure 5-8. Zone 1: Offset distribution – PP survey. Orthogonal geometry (left); slant geometry (right).

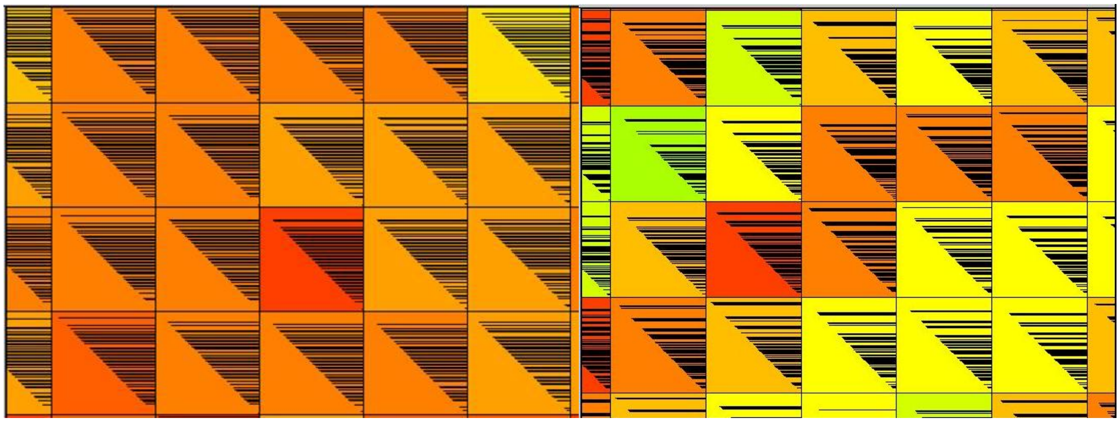

Figure 5-9. Zone 1: Offset distribution – PS survey. Orthogonal geometry (left); slant geometry (right).

Figures 5-8 to 5-11 show the offset distribution. Each square is a CMP bin (30 m x 30 m), and the number of lines equals the fold. The length of these lines indicates the source-receiver offset of the trace in that bin. The color represents the fold with the same scale as in Figures 5-2 and 5-3. In general for orthogonal geometry, the offset distribution is good but deteriorates in the center of the box (region inside two consecutive source lines and two consecutive receiver lines) where some near offsets are missing (Cordsen, 2000). For slant geometry (45 degrees), the offset distribution is usually well dispersed with few duplicates. Good offset distribution is important to assist in the process of velocity calculation for normal moveout corrections and to produce a good stack response. It also improves noise attenuation, and amplitude versus offset (AVO) analysis. Poor offset distributions can produce aliasing of dipping signal, and source noise (Lansley, 2011).

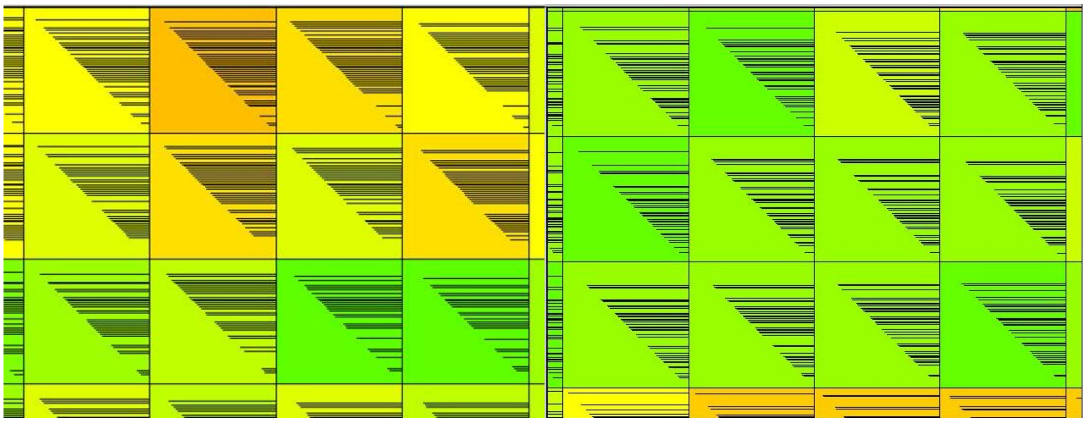

Figure 5-10. Zone 2: Offset distribution – PP survey. Orthogonal geometry (left); slant geometry (right).

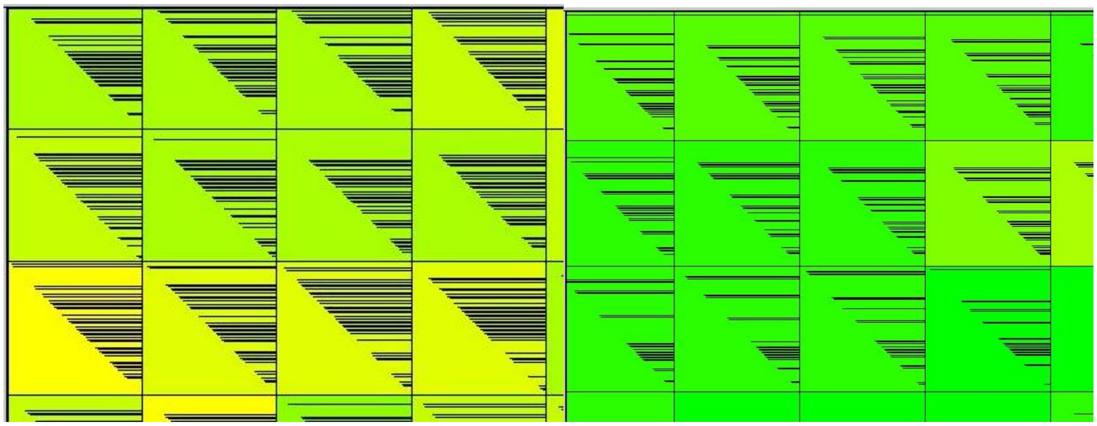

Figure 5-11. Zone 2: Offset distribution – PS survey. Orthogonal geometry (left); slant geometry (right).

From Figure 5-4 to Figure 5-11, it is concluded that orthogonal geometry produces a better azimuth and offset distribution for data inversion. Offsets and azimuths were lost due to the lake despite increasing the number of shots inside the lake because the receiver interval was also increased. The lost was more obvious for converted waves because there were fewer receivers inside the lake and as it is known, the conversion points are closer to the receivers.

In this case study the slant geometry was produced by laying out receiver lines at 45 degrees, as the source lines must be in an east-west direction to use previous cut lines as mentioned earlier. This geometry produced longer offsets in the direction of the receiver lines (ray paths in Figure 5-2). Orthogonal geometry produced a better offset distribution for all azimuths, and for this reason it was chosen for the planned seismic acquisition. Homogenous offsets and azimuth distribution is desirable to produce uniform stacking characteristics (Cooper, 2004a). The stronger footprint produced by the orthogonal geometry on the PS survey can be improved by optimizing design parameters per example by decreasing the receiver line interval. Cooper (2004b) affirms that patterns of low and high fold are more influenced by the usable offset than by the geometry type and offset is often ultimately limited in processing with the choice of mutes.

For all these experiments, the patch used was 20 lines with 100 receivers per line; for the final survey, this was changed to 26 lines so that an aspect ratio of 1.0 would be obtained. The reason for this change is to acquire more appropriate data for inversion as mentioned previously.

Larger offsets are required to differentiate between different surface-wave modes and to record longer wavelengths (lower frequencies). Lower frequencies provide information from deeper structures (Ivanov et al., 2008). In general, the acquisition geometry needs to be wide azimuth so that the subsurface is sampled from all directions hence the acquisition is closer to a true 3D survey (Canning et al., 1996). Sampling all offsets and all azimuths will provide full sampling of the 3D wavefield (Malcolm Lansley course notes); but in wide azimuth data, each azimuth is not sufficiently sampled producing irregularities (in azimuth and offsets) affecting pre-stack migration, pre-stack amplitude versus offset (AVO) or pre-stack amplitude versus azimuth (AVOA).

Footprint geometry should be avoided since the design stage, but in case it is still produced after acquisition, it should be removed or attenuated in processing, if possible. The interpreter should pay attention to the possibility of having these non-geological artifacts by overlying the acquisition geometry on different time slices (Cordsen, 2000).

5.4 Summary of this chapter

In this chapter, a discussion of survey design for compressional and converted waves was presented with emphasis on evaluating possible geometry footprint due to the survey design. Orthogonal and slant geometries were analysed for areas of the survey with two different characteristics: two large lakes are located inside this area, so a different layout was tested inside the lake, and the direction of source lines had to be east-west with some segments being moved to old cut lines to avoid new line cutting. After the analysis, orthogonal geometry was chosen for the seismic survey because produced better offset and azimuth distributions.

Chapter Six: **CONCLUSIONS AND FUTURE WORK**

In the first part of this thesis, detailed P-wave and S-wave near-surface characterization was carried out along three different seismic lines, to estimate static corrections required for processing the seismic reflection data that will be collected in an area in northeast British Columbia. The main conclusions from this part of the study are:

- Two of the lines (Line 101 and 104) had P-wave data and the near-surface models obtained showed two layers with similar P-wave velocities of ~ 1950 m/s for the first layer and ~ 2800 m/s for the second layer. A channel was detected to the east end of Line 104 which is perpendicular to this channel. The channel was previously interpreted from an electromagnetic (EM) survey acquired in the same area. Line 101 runs parallel and adjacent to the channel so the influence of the channel is not as evident as in Line 104.
- Some difficulties were encountered when applying the plus-minus method on the P-wave dataset due to insufficient offsets to reliably determine the reciprocal time. These values were extrapolated because pairs of shots for the analysis had to be chosen quite far apart so that appropriate plus-minus windows could be established.
- Two of the lines (Line 103 and 104) had SH-wave data. The final model obtained from the SH-wave datasets showed more detail in the near-surface structure than determined from P-wave data. Line 104 showed three layers in the west end of the line and two layers to the east end of the line. The presence of the channel is confirmed towards the east end of this line. Line 103 showed three layers along the entire profile. The velocities are also similar in both lines. The S-wave velocity of the first layer was found to be around 375 m/s, that for the second layer was ~ 727 m/s and the S-wave velocity for the third layer was ~ 1400 m/s.
- The analysis of the S-wave data on Line 104 was difficult from stations 1400 to 1600 because there were an insufficient number of refracted arrivals coming from

the second refractor as first breaks. Thus, the plus-minus window was too narrow and this prevented the reciprocal shot being located within the refractor data window being analysed. Consequently the second refractor was not clearly identified in this region.

- The difference in model results between the two wave modes is due to higher sensitivity of shear waves to changes in velocities.
- The static correction times for Line 103 were similar to those for the shear-wave data of Line 104 where the values of -200 ms to -250 ms are computed across the channel area. Line 103 lies entirely within the channel whereas Line 104 crosses the channel near the east end of the line where the values of statics were found to coincide. The geologic composition in the channel fill is believed to be unconsolidated sediments and glacial till, so higher static corrections are reasonable. The P-wave statics are of similar magnitude for both Line 101 and Line 104; the influence of the channel is not as significant on the P-wave data, which is why the P-wave static corrections do not vary as much as the S-wave static correction values.
- Lines 101 and 103 run parallel to the channel and for this reason the static correction times are more uniform compared to the static corrections for Line 104, which is perpendicular to the secondary channel; in Line 104 the influence of the channel is more evident.
- The GLI method and the plus-minus method gave different near-surface models for the S-wave data because the GLI method forces continuous layers along the profile, whereas the plus-minus method gives the flexibility of changing analysis windows depending on data changes, and allows more significant lateral changes in the velocity-depth model. Data variability reflects changes in the sub-surface, such as pinching out of a layer when the first breaks coming from that refractor diminish.

The second main contribution in this thesis is Vp/Vs analysis. This was undertaken for both the near-surface and deeper structure along Line 104. For the shallow section, results from the refraction analysis were used to calculate Vp/Vs and for the deeper structure, the main reflectors were interpreted in both PP and PS sections and these interpretation enabled event registration that generated interval Vp/Vs.

- Good agreement in Vp/Vs was found for the shallow section between the calculated values and those determined from a well log. For the deeper structure, this ratio was obtained from horizon registration of PP and PS migrated sections, and these interval Vp/Vs values matched closely those from the well log data.

Finally, the third part of this thesis was related to the design of the multicomponent survey that will be acquired in the area this winter. The conclusions from this section are:

- PS surveys can be designed to give as good attribute results as PP surveys and this will let us take advantage of the new application of the PS surveys such as structural imaging, lithologic estimation, anisotropy analysis, subsurface fluid description and reservoir monitoring.
- The refraction survey brought information needed to design the 3D/3C seismic survey. The data extracted was: 2D fold, steepest dip, mute for shallow markers, target two way time, interval velocity above the target, dominant frequency and maximum frequency at the target horizon.
- Values of Vp/Vs were integrated in the PS survey design to locate the common conversion points and to calculate the bin size as they both depend on this ratio. These are needed to estimate fold, offset and azimuth distributions. For the footprint analysis, the bin size for the PS design was forced to be equal to that of the PP design to make a proper comparison.
- An orthogonal acquisition geometry was chosen because it produced better distributions of seismic attributes than using a slant geometry design. Fold stripes in the east-west direction can be seen but they are not necessarily product of the

specific design but of the requirement of moving source lines to previously existing cut lines in order to minimize environmental concerns. This restriction produced stripes of low and high fold that cannot be avoided. The acquisition geometry footprint produced created by the orthogonal geometry can be improved by optimizing design parameters, especially the receiver line interval.

- Choosing a geometry that minimizes the possibilities of geometry footprint, improves the quality of stratigraphic mapping, attribute analysis and inversion results.

Recommendations for future research include collecting more refraction data using longer offsets in order to have a better definition of the analysis window required for the plus-minus time analysis method. It would also be interesting to apply other refraction methods as the Generalized Reciprocal Method (GRM) to compare with the results of the depth-velocity structure. In terms of the Vp/Vs analysis, it is recommended to perform PP to PS registration with logs from wells closer to the lines where the seismic data is available. This will improve the interval Vp/Vs obtained from this analysis, and provide a better lithologic understanding of the subsurface in the study area.

REFERENCES

Al Dulaijan, K., 2008. Near-surface Characterization Using Seismic Refraction and Surface-wave Methods: M.Sc. thesis, University of Calgary

Al-Shuhail, A. A. 2004. Estimation of sand dune thickness using a vertical velocity profile. Earth Sciences Department. King Fahd University of Petroleum & Minerals (KFUPM). The Arabian Journal for Science and Engineering, Volume 29, Number 2A.

Ashton, C.P., Bacon, B., Mann, A., Moldoveanu, N., Déplanté, C., Dickilreson, Sinclair, T. and Redekop, G. 1994. 3D Seismic Survey Design. Oilfield Review 6, 19-36

Avseth, P., Mukerji, T., and Mavko, G., 2005. Quantitative seismic interpretation. Cambridge

Blargy, J. P. 1992. Integrated seismic lithologic interpretation: the petrophysical basis. Ph.D. thesis, Stanford University Dept. of Geophysics, School of Earth Sciences, 1992 - Technology & Engineering - 383 pages

British Columbia Ministry of Energy and Mines. 2011. Ultimate Potential for Unconventional Natural Gas in Northeastern British Columbia's Horn River Basin.

Canning, A. and Gardner, G. 1996. Another look at the question of azimuth. The Leading Edge.

Carvalho, J., Torres, L., Castro, R. Dias, R. and Mendes-Victor, L. 2009. Seismic velocities and geotechnical data applied to the soil microzoning of western Algarve, Portugal, Journal of Applied Geophysics.

Castagna, J.P., Batzle, M.L., and Eastwood, R.L., 1985, Relationship between compressional-wave and shear-wave velocities in clastic silicate rocks: Geophysics, 50, p. 571-581

Cerda, F. 2001. Time-lapse (4-D), Vp/Vs Interpretation of Reservoir Depletion in Teal South Field, Gulf of Mexico: M. Sc. Thesis, University of Texas at Austin.

Cooper, N. 2004a. A world of reality—Designing land 3D programs for signal, noise, and prestack migration. Part I. The Leading Edge. P1007-1014

Cooper, N. 2004b. A world of reality—Designing land 3D programs for signal, noise, and prestack migration. Part II. The Leading Edge. P 1230-1235

Cordsen, A., Galbraith, M. And Peirce, J. 2000. Planning Land 3-D seismic Surveys. Geophysical developments No. 9. Society of Exploration Geophysicists.

Cordsen, A., and Lawton, D. C., 1996. Designing 3-component 3D seismic surveys. Society of Exploration Geophysicists

Cox, M., 1999, Static corrections for seismic reflection surveys: Society of Exploration Geophysicists

DeAngelo, M. V., Backus, M., Hardage, B. A., Murray, P., and Knapp, S. 2003. Depth registration of P-wave and C-wave seismic data for shallow marine sediment characterization, Gulf of Mexico. The Leading Edge. P. 96-105

Dobrin, M., and Savit, C. H., 1988, Introduction to geophysical prospecting. Mc-Graw Hill Book Co

Domenico. S.N., 1974, Effect of water saturation on seismic reflectivity of sand reservoirs encased in shale: Geophysics 39,759-769.

__1976, Effect of brine-gas mixture on velocity in an unconsolidated sand reservoir: Geophysics 41, 882-894.

__1984, Rock lithology and porosity determination from shear and compressional wave velocity: Geophysics 49, 1188-1195

Dufour, J., 1996, Refraction statics analysis of P-S Seismic data using the plus-minus time analysis method: M. Sc. Thesis, Univ. of Calgary

Eastwoos, R.L. and Castagna, J.P. 1987. Interpretation of Vp/Vs ratios from sonic logs. Geophysical development series, Volume 1 SEG P139-153

Eaton, D. W S., Slotboom, R. T., Stewart, R. R., and Lawton, D. C., 1990. Depth-Variant Converted-Wave Stacking. 60th Annual International. Meeting., Soc. Expl. Geophys., Expanded Abstracts, 1107-1110

Eaton, D.W.S. and Lawton, D.C., 1992, P-SV stacking charts and binning periodicity: Geophysics, **57**, 745-748.

Emery, D. J. and Stewart R. R. 2006. Using VP/VS to explore for sandstone reservoirs: well log and synthetic seismograms from the Jeanne d'Arc basin, offshore Newfoundland. CREWES Research Report — Volume 18

Ferri, F. Hickin, A. and Huntley, D. H. 2011. Besa River Formation, western Liard Basin, British Columbia (NTS 094N): geochemistry and regional correlations. BC Ministry of Energy and Mines. Geoscience report.

Fetter, C.W., 1994. Applied Hydrogeology. Third edition. Prentice-Hall Inc. Englewood Cliffs, NJ. P. 691

Fomel, S., Backus, M. M., DeAngelo, M. V., Murray, P. E. Hardage, B. A., 2003. Multicomponent seismic data registration for subsurface characterization in the shallow Gulf of Mexico. Offshore Technology Conference, Houston

Fromm, G., Krey, T. and Wiest, B., 1985, Static and dynamic corrections in Dohr, G., Ed., Seismic shear waves: Handbook of Geophysical Exploration, Vol. 15a, Geophysical Exploration Press, 191-225

Gardner, L. W., 1939, Seismograph prospecting: U.S. patent 2,153,920 (application 1936)

Gardner, L. W., 1939, An areal plan of mapping subsurface structure by refraction shooting: Geophysics, v. 4, p. 247-259

Garotta,R.J., and Marechal,P., 1987, "Shear wave polarization survey using converted waves," 57th Annual International Meeting, SEG, Expanded Abstracts, Session S11-6.

Garotta, R., and Granger, P.Y., 1988, Acquisition and processing of 3Cx3D data using converted waves: 58th Annual International Meeting, SEG, Expanded Abstracts, pp 995-997

Garotta, R., Granger, P.Y., and Dariu, H. 2002 Combined interpretation of PP and PS data provides direct access to elastic rock properties. The Leading Edge. 532-535

Glass, D.J. 1997. Lexicon of Canadian stratigraphy volume 4 Western Canada, including Eastern British Columbia, Alberta, Saskatchewan and southern Manitoba; Canadian Society of Petroleum Geology, Calgary, p. 1423

Guevara, S., Margrave, G. Agudelo, W. and Gomez, F. 2011. Near-surface S-wave velocity models from two uphole surveys. CREWES-University of Calgary / Ecopetrol-ICP.

Hagedoorn, J. G., 1959, The plus-minus method of interpreting seismic refraction sections: Geophysical prospecting, 7, 158-181.

Hampson, D., and Russell, B., 1984, First-break interpretation using generalized linear inversion: J. Can. Soc. Expl. Geophys., **20**, 40–54.

Han, D.H., NW. A. and Morgan, D., 1986, Effects of porosity and clay content on wave velocities in sandstones: Geophysics 51.2093-2107.

Hickin, A. and Kerr, B. 2005. Bedrock topography mapping and shallow gas in Northeastern BC. Summary of activities. BC Ministry of Energy and Mines, p 69-75

Hickin, A., Kerr, B., Turner, D.G. and Barchyn, T.E. 2008. Mapping quaternary paleovalleys and drift thickness using petrophysical logs, northeast British Columbia, Fontas map sheet, NTS 94I Canadian Journal of Earth Sciences, **45**.

Ivanov, J., Miller, R. D. and Tsoflias, G. 2008. Some practical aspects of MASW analysis and processing. 21st EEGS Symposium on the Application of Geophysics to Engineering and Environmental Problems. Environmental & Engineering Geophysical Society (EEGS)

Jain, S., 1987. Amplitud-vs-offset analysis: a review with reference to application in Western Canada. Journal of the Canadian society of exploration geophysicists. Vol. 23. No. 1, P 27-36

Kilty, K.T., Norris R.A., McLamoreS R., Hennon, P., and Euge, K., 1986. Seismic refraction at Horse Mesa Dam: An application of the generalized reciprocal method. Geophysics, Vol. 51, No. 2; P. 266-275

Krey, T. 1987. Attenuation of random noise by 2D and 3D CDP stacking and Kirchhoff migration. Geophysical prospecting

Kuster, G.T. and Toksdz. M.N., 1974, Velocity and attenuation of seismic waves in two-phase media: Part I & II: Geophysics 39,587-618.

Lane, M. and Lawton, D. C. 1993. 3-D converted wave asymptotic binning. CREWES research report volume 5

Lansley, M. 2004. CMP fold: a meaningless number?. The Leading Edge. 23. P 1038-1041

Lansley, M. 2011. 3D Seismic Data Acquisition: An Update on Modern Technologies and Usage Methodologies". Canadian Society of Exploration Geophysicist (CSEG), Doodle Train, Calgary

Lawton, D. C., 1989, Computation of refraction static corrections using first-break traveltime differences. Geophysics, vol. **54**, no. 10 (October 1989); p. 1289-1296,

Lawton, D.C., 1990, A 9-component refraction seismic experiment: Canadian journal of exploration geophysicist, 25, Nos. 1&2, 7-16

Lawton, D. C., 1993, Optimum bin size for converted-wave 3-D asymptotic mapping: CREWES Research Report, Volume 5, p. 28.1 - 28.14.

Lawton, D. C., Stewart, R.R., Cordsen, A., and Hrycak, S. 1995. Advances in 3C-3D design for converted waves. CREWES research report volume 7. P. 43.1 – 43.72

Lawton, D. C. and Hoffe, B. H. 2000. Some binning issues for 4C-3D OBC survey design. Consortium for Research in Elastic Wave Exploration Seismology (CREWES), University of Calgary.

Levson, V.M., Ferbey, T., Kerr, B.J., Johnsen, T., Smith, I.R., Blackwell, J. and Jonnes, S. 2004. Quaternary geology and aggregate mapping in northeast British Columbia: applications for oil and gas exploration and development. BC Ministry of Energy and Mines, Summary of Activities, p. 29-40.

Levson, V.M., Ferbey, T., Hickin, A., Bednarski, J., Smith, R., Demchuk, T., Trommelen, M., Kerr, B., and Church, A. 2005. Surficial Geology and Aggregate Studies in the Boreal Plains of Northeast British Columbia BC Ministry of Energy and Mines, Summary of Activities, p. 42-50

Levson, V., 2008. Geology of northeast British Columbia and northwest Alberta: diamonds, shallow gas, gravel, and glaciers. Canadian Journal of Earth Science. 45: 509-512

MacAulay, H. A., and Hunter, J. A. 1982. Detailed seismic refraction analysis of ice-bonded permafrost layering in the Canadian Beaufort Sea. Geological Survey of Canada, Ottawa, 4th Canadian Permafrost Conference

Martin, F., 2002, First breaks analysis for 3D shear seismic refraction statics, EAGE 64th Conference & Exhibition

McPhail, S., Walsh, W., Lee, C. and Monahan, P. A. 2008. Shale units of the Horn River Formation, Horn River Basin and Cordova Embayment, Northeastern British Columbia. British Columbia Ministry of Energy, Mines and Petroleum Resources / Monahan Petroleum Consulting/Penn West Energy Trust

Meier, M. A. 2009. Converted-wave survey design. SEG Houston 2009 International Exposition and Annual Meeting

Meier, M. A. and Lee, P. 2009. Converted-wave resolution. Geophysics, 74, No. 2. March - April 2. P. Q1–Q16.

Miller, S. L. and Stewart, R. R. 1990. Effects of lithology, porosity and shaliness on p - and s-wave velocities from sonic logs. Canadian Journal of Exploration Geophysics. Vol. 26, No 1 & 2. P. 94.103

Miller, S. L., 1992. Well log analysis of Vp and Vs in carbonates. Crewes Research report Volume 4.

Miller, S. L., 1996. Multicomponent Seismic data Interpretation: M.Sc. thesis, Univ. of Calgary

Monahan, P., 1999. Stratigraphy and potential hydrocarbon objectives of Mississippian to Lower Cretaceous strata in the eastern Liard Basin area. British Columbia Dept. of Energy, Mines, and Mineral Resources, consulting report.

Morrow, D.W., and G.D. Davies, 2001. The Liard Basin Manetoe Dolomite: a new look at a frontier deep gas play. Proceedings, CSPG Rock the Foundation Convention.

Morrow, D.W., B.C. MacLean and L.S. Lane, 2001. Liard Basin and Trout Plain: tectonic evolution and petroleum potential, NWT. Proceedings, CSPG Rock the Foundation Convention.

Morrow, D.W., M. Zhao, and L.D. Stasiuk, 2002. The gas-bearing Devonian Presqu'ile Dolomite of the Cordova Embayment region of British Columbia, Canada: dolomitization and the stratigraphic template. AAPG Bulletin, v. 86, #9, p. 1609-1638.

Musser, J.A., 2003. Seismic Survey Designs for Converted Waves GMG/AXIS Inc., Denver, CO. CSPG document

Neidell, N. 1994. Sampling 3-D seismic surveys: A conjecture favoring coarser but higher-fold sampling. The Leading Edge. P 764-768

Paine, J. G., and Collins, E. W., 2003, Applying airborne electromagnetic induction in groundwater salinization and resource studies, West Texas, in Proceedings, Symposium on the Application of Geophysics to Engineering and Environmental Problems: Environmental and Engineering Geophysical Society, p. 722-738 (CD-ROM)

Palmer, D., 1980, The Generalized reciprocal method of seismic refraction interpretation. Society of Exploration Geophysicist. Tulsa

Palmer, D., 1986, Hand book of Geophysical Exploration. Refraction Seismics: The lateral resolution of structure and seismic velocity, Geological Survey of New South Wales, Department of Mineral resources. Geophysical Press, London – Amsterdam. Volume 13

Palmer, D., 2005. Computing detailed refraction statics in a hard rock terrain with the GRM and the RCS. The University of New South Wales, and Leonie Jones, Geoscience Australia. SEG/Houston 2005 Annual Meeting

Parry, D.G. and Lawton, D.C., 1993, Near surface characterization using a 9-component refraction survey: Cochrane, Alberta, CREWES Research Report, 5

Petrel Robertson Consulting Ltd., 2003, Exploration Assessment of Deep Devonian Gas Plays, Northeastern British Columbia. British Columbia Ministry of Energy and Mines

Picket, G.R., 1963, Acoustic character logs and their applications information evaluation. Journal of Petroleum technology. 15, 659-667.

Richardson, S. E., and Lawton, D. C. Vp/Vs character of shallow strata, Red Deer, Alberta. CREWES Research Report — Volume 15 (2003)

Roche, S., Wagaman, M., and Watt H., 2005, Anadarko basin survey shows value of multicomponent acquisition: First Break, 23, 43-51.

Sheriff, R.E., 1991. Encyclopedic Dictionary of Applied Geophysics. Society of Exploration Geophysicists. Fourth Edition

Sheriff, R. E., and Geldart, L. P., 1995, Exploration Seismology, Second Edition, Cambridge University Press, Cambrige, U.K., 592 p.

Shi, H., Hou X., Yan F., and Li, Z. 2005. Application case: 3-D static correction in complex mountains of Tarim Basin SEG/Houston 2005 Annual Meeting. BGP, CNPC

Simmons, J. L., Backus, and M. M., 1999, Radial-Transverse (SV-SH) coordinates for 9-C 3-D seismic reflection data analysis. Expanded Abstracts

Sjögren, B. 1984. Shallow Refraction Seismics. London, New York: Chapman & Hall. 270 pp.

Stümpel, H., Kahler, S., Meissner, R. and Milkereit, B. The use of seismic shear waves and compressional waves for lithological problems of Shallow sediments. Geophysical Prospecting **32**,662-675, 1984

Stewart, R. R., Gaiser, J., Brown, R. J. and Lawton, D. C., 2002, Converted-wave seismic exploration: Methods: Geophysics, Society of Exploration Geophysicist, 67, 1348-1363.

Stewart, R. R., Gaiser, J., Brown, R. J. and Lawton, D. C., 2003, Converted-wave seismic exploration: Applications: Geophysics, Society of Exploration Geophysicist., 68, 40-57.

Tatham, R.H., and McCormack, M. D., 1991, Multicomponent seismology in petroleum exploration: Society of Exploration Geophysicists

Taylor, J. R. 1982. An introduction to error analysis. The study of uncertainties in physical measurements. Oxford University Press

Telford,W. M., Geldart L. P. and Sheriff, R. E., 1991. Applied Geophysics. 2nd edition. Cambridge University Press.

Van Veldhuizen, E. J., Blacquière, G., and Berkhout, A. J. Acquisition geometry analysis in complex 3D media. Geophysics, **73**, no. 5 September-October 2008. p. 43–58

Vermeer, G.J. 2002 3D seismic survey design. Society of Exploration Geophysicist

Yin, H. 1992. Acoustic velocity and attenuation of rocks: Isotropy, intrinsic anisotropy and stress induced anisotropy. Ph.D. thesis, Stanford University